LUND UNIVERSITY

D1.2 MaMi Channel Characteristics: Measurement Results

Bourdoux, Andre; Desset, Claude; van der Perre, Liesbet; Dahman, Ghassan; Edfors, Ove; Flordelis, Jose; Gao, Xiang; Gustafson, Carl; Tufvesson, Fredrik; Harrysson, Fredrik; Medbo, Jonas

2015

Link to publication

Citation for published version (APA):
Bourdoux, A., Desset, C., van der Perre, L., Dahman, G., Edfors, O., Flordelis, J., Gao, X., Gustafson, C., Tufvesson, F., Harrysson, F., & Medbo, J. (2015). *D1.2 MaMi Channel Characteristics: Measurement Results*. MAMMOET. http://cordis.europa.eu/docs/projects/cnect/6/619086/080/deliverables/001-D12Ares20152866415.pdf

Total number of authors:
11

General rights
Unless other specific re-use rights are stated the following general rights apply:
Copyright and moral rights for the publications made accessible in the public portal are retained by the authors and/or other copyright owners and it is a condition of accessing publications that users recognise and abide by the legal requirements associated with these rights.
• Users may download and print one copy of any publication from the public portal for the purpose of private study or research.
• You may not further distribute the material or use it for any profit-making activity or commercial gain
• You may freely distribute the URL identifying the publication in the public portal

Read more about Creative commons licenses: https://creativecommons.org/licenses/

Take down policy
If you believe that this document breaches copyright please contact us providing details, and we will remove access to the work immediately and investigate your claim.

LUND UNIVERSITY

PO Box 117
221 00 Lund
+46 46-222 00 00

Download date: 23. Aug. 2025

Ref. Ares(2015)2866415 - 08/07/2015

D1.2

MaMi Channel Characteristics: Measurement Results

Project number:	619086
Project acronym:	**MAMMOET**
Project title:	Massive MIMO for Efficient Transmission
Project Start Date:	1 January, 2014
Duration:	36 months
Programme:	FP7/2007-2013
Deliverable Type:	Report
Reference Number:	ICT-619086-D1.2
Workpackage:	WP 1
Due Date:	30 June, 2015
Actual Submission Date:	30 June, 2015
Responsible Organisation:	ULUND
Editor:	Ove Edfors and Fredrik Tufvesson
Dissemination Level:	PU
Revision:	1.0

Abstract: This deliverable presents channel measurement results for the scenarios Open exhibition and Crowded auditiorium. The measurement procedure and equipment are described. Massive MIMO (MaMi) channel characteristics and key parameters are extracted and used in an extended COST 2100 channel model for MaMi. The initial validation performed shows that the model is capable of reproducing the statistics in terms of temporal behavior of the user separability, singular value spread, capacity and sum-rate and directional characteristics. The model can be used for system and link level MaMi simulations.

Keywords: 5G, Massive MIMO, MaMi, measurement, channel model, channel characterization

This project has received funding from the European Union's Seventh Framework Programme for research, technological development and demonstration under grant agreement no. 619086.

Editor

Ove Edfors and Fredrik Tufvesson (ULUND)

Contributors (ordered according to beneficiary numbers)

Andre Bourdoux (imec)
Claude Desset (imec)
Liesbet van der Perre (imec)

Ghassan Dahman (ULUND)
Ove Edfors (ULUND)
Jose Flordelis (ULUND)
Xiang Gao (ULUND)
Carl Gustafson (ULUND)
Fredrik Tufvesson (ULUND)

Fredrik Harrysson (EAB)
Jonas Medbo (EAB)

Reviewer and supporting editor
Michael Höberl (TEC)
Marion Buchacher (TEC)

Executive Summary

We discuss requirements on massive MIMO channel models and compare to existing channel models, leading to a number of required modifications of the COST 2100 model. MAMMOET scenarios from deliverable D1.1 are discussed and two important ones are selected for further study, namely the "Open Exhibition" and "Crowded auditorium", of which the first is an outdoor one and the second is an indoor one. The performed measurements are described, in terms of equipment, setup and measurement configuration. Measurement sites are described in detail, using (aerial) photographs and drawings to establish environments and their physical dimensions.

Channel measurement data is analyzed in terms of singular-value spreads, sum-rate capacities, directional properties and time/frequency correlations. Multipath components are identified using the SAGE algorithm and clustering performed using the KpowerMeans clustering algorithm. Sanity checks are performed by visually correlating identified multipath components with physical objects in the propagation environment and channel model parameters are extracted.

The COST 2100 channel model extension includes the following changes, all made so that backward compatibility with COST 2100 can be maintained:

- Extension from two to three dimensions, to be able to capture as much as possible of the three dimensional propagation channels experienced as the envisioned large base station arrays are expected to be able to resolve multipath clusters both in azimuth and elevation.
- Visibility regions are introduced on the base-station array side, to capture large-scale fading effects along physically large arrays.
- Individual gain functions on multipath components are introduced to better model environments with crowds, where individual multipath components tend not to be visible in the entire cluster visibility region.

Model parameters from MAMMOET channel measurements and both the COST 2100 and the WINNER II channel models are used to get a complete set of model parameters. The channel model has been implemented in MATLAB (reported in D1.3) and validation is performed by comparing against measurements, using the same measures as described above (singular-value spreads, sum-rate capacities, directional properties and time/frequency correlations). Similarities and discrepancies are discussed and future use of the models in MAMMOET are expected to deliver feedback that will be used in a continuous update and improvement cycle of both the analysis and the models.

Contents

1 Introduction **1**

2 Massive MIMO channels **2**
2.1 Massive MIMO propagation characteristics . . . 2
2.2 Channel models . . . 3
2.2.1 Existing conventional MIMO models . . . 3
2.2.2 Necessary model extensions . . . 3

3 Measured MAMMOET scenarios **5**
3.1 MAMMOET scenario overview . . . 5
3.2 Scenario selection . . . 6

4 Channel measurement setups **7**
4.1 Measurement equipment . . . 7
4.2 Configuration for MAMMOET measurements . . . 8

5 Measurement campaigns **10**
5.1 Open Exhibition . . . 10
5.2 Crowded Auditorium . . . 11

6 Measurement data analysis **13**
6.1 Singular value spreads . . . 13
6.1.1 Effect of the number of BS antenna ports on the singular value spread . . . 13
6.1.2 Effect of the density of users on the singular value spread . . . 15
6.2 MRT and ZF capacity . . . 16
6.3 Directional analysis . . . 25
6.4 Temporal behavior . . . 28
6.5 Multipath component clustering . . . 34
6.5.1 Approach . . . 34
6.5.2 Results and discussion . . . 38
6.5.3 Cluster parameters . . . 52

7 Massive MIMO channel model **67**
7.1 Approach and scope . . . 67
7.1.1 Model consistency . . . 67
7.1.2 The COST 2100 channel model extension . . . 68
7.1.3 Model limitations . . . 71
7.2 Model parameters . . . 71
7.3 Validation against measurements . . . 72

7.3.1 Singular value spreads 72
7.3.2 MRC and ZF sum-rates 72
7.3.3 Temporal behavior 75

8 Summary **76**

List of Abbreviations **78**

Bibliography **80**

List of Figures

4.1 (a) The cylindrical array with 128 ports. (b) View from site MS 2. 8
4.2 (a) A user holding the MS user equipment antenna with an inclination of 45°. (b) Users moving randomly within the five-meter diameter circle. 9

5.1 Aerial photo of the measurement area. Base station locations are indicated by the label BS. The different positions of the mobile users are labeled by MS 1, MS 2, MS 8 and MS 10, and indicated by the circles. MS 1 and MS 2 have LOS condition. MS 8 and MS 10 have NLOS condition. 11
5.2 Crowded auditorium measurement. (a) Base station locations are indicated by the label BS. Users positions are indicated by Group 1 (back), and Group 2 (middle). (b) A measurement run with 9 active users surrounded with 11 non-active users (crowd). 12

6.1 CDFs of the singular value spread when using 128, 64, 32, 16 and 10 antenna ports at the BS (in logarithmic units). The BS communicates simultaneously with nine users in the presence of crowd. Plots correspond to outdoor (top) and indoor (bottom) environments. For comparison purposes, CDFs of the singular value spread of i.i.d. Rayleigh channels with the same number of antenna elements are also given. (The legend is shared between both figures.) 14
6.2 Median of the normalized parallel channel gain (left) and singular value spread (right), in logarithmic units, when using 128 antenna ports at the BS in an outdoor, microcell deployment (site MS 2). Various numbers of scheduled users and user densities are considered. For comparison purposes, median values of the singular value spread and normalized parallel channel gain of i.i.d. Rayleigh channels with the same number of users also given. 17
6.3 Median of the normalized parallel channel gain (left) and singular value spread (right), in logarithmic units, when using 128 antenna ports at the BS in an outdoor, microcell deployment (site MS 1). 18
6.4 Median of the normalized parallel channel gain (left) and singular value spread (right), in logarithmic units, when using 128 antenna ports at the BS in an indoor auditorium deployment (BS 1, users at the back). 19

6.5 Median of the normalized parallel channel gain (left) and singular value spread (right), in logarithmic units, when using 128 antenna ports at the BS in an indoor auditorium deployment (BS 1, users at the center).

NOTE. Several limitations apply to this figure. First, the measurement data corresponding to the user density of 1.0 users/m^2 were obtained after a restart of the measurement equipment and, therefore, this measurement might suffer from a loss of accuracy. Second, the measurement data for the density of 0.0 users/m^2 were acquired on a different measurement occasion. In this case, the positions of UE antennas and BS are only approximate. 20

6.6 Median of the normalized parallel channel gain (left) and singular value spread (right), in logarithmic units, when using 128 antenna ports at the BS in an indoor auditorium deployment (BS 3, users at the back). 21

6.7 Median of the normalized parallel channel gain (left) and singular value spread (right), in logarithmic units, when using 128 antenna ports at the BS in an indoor auditorium deployment (BS 3, users at the center). 22

6.8 Sum-rate capacity and sum-rates with zero forcing (ZF) and maximum ratio transmission (MRT) for several user densities and two deployments: indoor auditorium (left) and outdoor suburban microcell (right). For comparison purposes, the sum-rate capacity of an i.i.d. Rayleigh channel with the same number of users and antennas is also given. 24

6.9 Two-dimensional PDFs of the propagation channel from user 1 to BS in an outdoor suburban microcell deployment (site MS 2, with user surrounded by a crowd). The PDFs are based on the estimated gains, directions and delays of 30 000 plane waves. The dynamic range if -110 dB to -60 dB. The amount of transferred energy that can be modeled as deterministic plane waves is also shown (bottom, right). 26

6.10 Two-dimensional PDFs of the propagation channel from user 1 to BS in an indoor auditorium deployment (BS 1, users at the back surrounded by a crowd). The PDFs are based on the estimated gains, directions and delays of 30 000 plane waves. The dynamic range is -80 dB to -30 dB. The amount of transferred energy that can be modeled as deterministic plane waves is also shown (bottom, right). 27

6.11 LOS component and the 30 strongest multipath components for users 1 and 2, at snapshot 100. This figure corresponds to an outdoor suburban microcell deployment (site MS 1). There is LOS to the BS and a crowd is present. 28

6.12 LOS component and the 30 strongest multipath components for users 1 and 2, at snapshot 100. This figure corresponds to an outdoor suburban microcell deployment (site MS 2). There is LOS to the BS and a crowd is present. 29

6.13 LOS component and the 50 strongest multipath components for users 1 and 2, at snapshot 100. This figure corresponds to an outdoor suburban microcell deployment (site MS 8). There is NLOS to the BS and a crowd is present. . . . 29

6.14 LOS component and the 50 strongest multipath components for users 1 and 2, at snapshot 100. This figure corresponds to an outdoor suburban microcell deployment (site MS 10). There is NLOS to the BS and a crowd is present. . . . 30

6.15 LOS component and the 30 strongest multipath components for users 1 and 2, at snapshot 10. This figure corresponds to an indoor auditorium deployment (BS 1, users at the center). There is LOS and no crowd is present. 30

6.16 LOS component and the 30 strongest multipath components for users 1 and 2, at snapshot 10. This figure corresponds to an indoor auditorium deployment (BS 1, users at the back). There is LOS and no crowd is present. 31
6.17 LOS component and the 30 strongest multipath components for users 1 and 2, at snapshot 10. This figure corresponds to an indoor auditorium deployment (BS 3, users at the center). There is LOS and no crowd is present. 31
6.18 LOS component and the 30 strongest multipath components for users 1 and 2, at snapshot 10. This figure corresponds to an indoor auditorium deployment (BS 3, users at the back). There is LOS and no crowd is present. 32
6.19 Cumulative distribution function (CDF) of the 3-dB coherence time (left) and 3-dB coherence bandwidth (right) of the measured 9×128 SISO channels. The CDF is shown for two different deployments, namely, indoor auditorium (BS 1, users at the back) and outdoor suburban microcell (site MS 2), and for two different user densities. Recall that the snapshot sampling rate is ca. 60 ms (Tab. 4.1); hence, the coarse temporal resolution of the time coherence CDF (left). 33
6.20 For an indoor auditorium deployment (BS 1, users at the back in the presence of a crowd) the plots show: time series of the real part of the correlation coefficients $c_{1,2}$ and $c_{1,3}$ (top); frequency dependency of the real part of the correlation coefficients $c_{1,2}$ and $c_{1,3}$ (bottom left); and, probability density function (PDF) of the real part of the correlation coefficients over all user pairs, snapshots and subcarriers. 35
6.21 For an outdoor suburban microcell deployment (site MS 2, in the presence of a crowd) the plots show: time series of the real part of the correlation coefficients $c_{1,2}$ and $c_{1,3}$ (top); frequency dependency of the real part of the correlation coefficients $c_{1,2}$ and $c_{1,3}$ (bottom left); and, probability density function (PDF) of the real part of the correlation coefficients over all user pairs, snapshots and subcarriers. 36
6.22 For an indoor auditorium environment (BS 1, users at the back in the presence of a crowd) the plots show: time series of the small-scale gain of the narrowband channel for users 1 and 2 (top); frequency dependency of the small-scale gain of the narrowband channel of users 1 and 2 (bottom left); and, probability density function (PDF) of the small-scale gain of the narrowband channels over all users, snapshots and subcarriers. 37
6.23 MPC strengths from all 9 users in all 300 snapshots, Site 1, with crowd. Color coding represents the channel gain of the MPCs in dB. The distance of each MPC point to the base station is the delay of the corresponding MPC. The circles indicate the positions of cluster centroids. Here we see that the clusters with different delays and azimuth angles are captured. 39
6.24 Clusters based on MPCs from all 9 users in all 300 snapshots, Site 1, with crowd. There are 15 clusters. Color coding represents different clusters. 39
6.25 MPC strengths from all 9 users in all 300 snapshots, Site 1, with crowd. Color coding represents the channel gain of the MPCs in dB. The strongest energy contribution comes from around 100 degrees azimuth angle, which is the direction of LOS. There are also strong signals due to scattering at the buildings around. 40
6.26 MPC delays from all 9 users in all 300 snapshots, Site 1, with crowd. Color coding represents the delay of the MPCs in meter. We can see that clusters with large delays are captured. 40

6.27 Clusters based on MPCs from all 9 users in all 300 snapshots, Site 1, with crowd. There are 15 clusters. Color coding represents different clusters. 41
6.28 MPC strengths from all 9 users in all 300 snapshots, Site 10 (at entrance of study center), with crowd. Color coding represents the channel gain of the MPCs in dB. Here we can see clusters are separated in delay and azimuth angle. 41
6.29 Clusters based on MPCs from all 9 users in all 300 snapshots, Site 10 (at entrance of study center), with crowd. There are 15 clusters. Color coding represents different clusters. 42
6.30 MPC strengths from all 9 users in all 300 snapshots, Site 10 (at entrance of study center), with crowd. Color coding represents the channel gain of the MPCs in dB. Here we see how the incoming energy is distributed in azimuth and elevation. 42
6.31 MPC delays from all 9 users in all 300 snapshots, Site 10 (at entrance of study center), with crowd. Color coding represents the delay of the MPCs in meter. Clusters with large delays are captured. 43
6.32 Clusters based on MPCs from all 9 users in all 300 snapshots, Site 10 (at entrance of study center), with crowd. There are 15 clusters. Color coding represents different clusters. 43
6.33 MPC strengths from user 1 in all 300 snapshots. Color coding represents the channel gain of the MPCs in dB. BS position 1, user group 1 (center seats), user arrangement 1, without crowd. 44
6.34 MPC delays from user 1 in all 300 snapshots. Color coding represents the delay of the MPCs in meter. BS position 1, user group 1 (center seats), user arrangement 1, without crowd. 45
6.35 Clusters and MPCs from user 1 in all 300 snapshots. Color coding represents different clusters. BS position 1, user group 1 (center seats), user arrangement 1, without crowd. There are 15 clusters. 45
6.36 Single-bounce scatterers from user 1 in all 300 snapshots. Color coding represents the channel power contribution of the scatterers in dB. There are 16 clusters, among which at least 12 are single-bounced clusters. BS position 1, user group 1 (center seats), user arrangement 1, without crowd. Here we clearly see strong incoming energy from the center seats and reflections on the walls. 46
6.37 Scatterers based on single-bounce assumption, from user 1 in all 300 snapshots. Color coding represents different clusters. There are 16 clusters, among which at least 12 are single-bounced clusters. BS position 1, user group 1 (center seats), user arrangement 1, without crowd. 47
6.38 MPC strengths from user 1 in all 300 snapshots. Color coding represents the channel power contribution of the MPCs in dB. BS position 1, user group 2 (back seats), user arrangement 1, without crowd. 48
6.39 MPC delays from user 1 in all 300 snapshots. Color coding represents the delay of the MPCs in meter. BS position 1, user group 2 (back seats), user arrangement 1, without crowd. 48
6.40 Clusters and MPCs from user 1 in all 300 snapshots. Color coding represents different clusters. BS position 1, user group 2 (back seats), user arrangement 1, without crowd. There are 15 clusters. 49

6.41 Single-bounce scatterers from user 1 in all 300 snapshots. Color coding represents the channel power contribution of the scatterers in dB. There are 15 clusters, among which 11 are single-bounced clusters. BS position 1, user group 2 (back seats), user arrangement 1, without crowd. We can see that strong incoming energy from the back seats and the back-left corner of the room, as well as the front wall and the right wall. 50
6.42 Scatterers based on single-bounce assumption, from user 1 in all 300 snapshots. Color coding represents different clusters. There are 15 clusters, among which 11 are single-bounced clusters. BS position 1, user group 2 (back seats), user arrangement 1, without crowd. 51
6.43 MPC strengths from user 1 in all 300 snapshots. Color coding represents the channel power contribution of the MPCs in dB. BS position 3, user group 1 (center seats), user arrangement 1, without crowd. 52
6.44 MPC delays from user 1 in all 300 snapshots. Color coding represents the delay of the MPCs in meter. BS position 3, user group 1 (center seats), user arrangement 1, without crowd. 53
6.45 Clusters and MPCs from user 1 in all 300 snapshots. Color coding represents different clusters. There are 15 clusters. BS position 3, user group 1 (center seats), user arrangement 1, without crowd. 53
6.46 Single-bounce scatterers from user 1 in all 300 snapshots. Color coding represents the channel power contribution of the scatterers in dB. There are 16 clusters, among which 12 are single-bounced clusters. BS position 3, user group 1 (center seats), user arrangement 1, without crowd. Strong energy comes from the center seats and the wall corner where the base station is located. 54
6.47 Scatterers based on single-bounce assumption, from user 1 in all 300 snapshots. Color coding represents different clusters. There are 16 clusters, among which 12 are single-bounced clusters. BS position 3, user group 1 (center seats), user arrangement 1, without crowd. 55
6.48 MPC strengths from user 1 in all 300 snapshots. Color coding represents the channel power contribution of the MPCs in dB. BS position 3, user group 2 (back seats), user arrangement 1, without crowd. 56
6.49 MPC delays from user 1 in all 300 snapshots. Color coding represents the delay of the MPCs in meter. BS position 3, user group 2 (back seats), user arrangement 1, without crowd. 56
6.50 Clusters and MPCs from user 1 in all 300 snapshots. Color coding represents different clusters. BS position 3, user group 2 (back seats), user arrangement 1, without crowd. There are 16 clusters. 57
6.51 Single-bounce scatterers from user 1 in all 300 snapshots. Color coding represents the channel power contribution of the scatterers in dB. There are 16 clusters, among which 11 are single-bounced clusters. BS position 3, user group 2 (back seats), user arrangement 1, without crowd. Strong energy comes the back seats as well as the wall corner where the base station is located. 58
6.52 Scatterers based on single-bounce assumption, from user 1 in all 300 snapshots. Color coding represents different clusters. There are 16 clusters, among which 11 are single-bounced clusters. BS position 3, user group 2 (back seats), user arrangement 1, without crowd. 59
6.53 CDF of the number of MPCs from all users in one cluster, LOS scenarios. 60
6.54 CDF of the number of MPCs from all users in one cluster, NLOS scenarios. . . . 60

6.55 CDF of the cluster delay spreads, LOS scenarios. 61
6.56 CDF of the cluster delay spreads, NLOS scenarios. 61
6.57 CDF of the cluster angular spreads in azimuth, LOS scenarios. 62
6.58 CDF of the cluster angular spreads in azimuth, NLOS scenarios. 62
6.59 CDF of the cluster angular spreads in elevation, LOS scenarios. 63
6.60 CDF of the cluster angular spreads in elevation, NLOS scenarios. 63
6.61 Cluster power decay, LOS scenarios. 64
6.62 Cluster power decay, NLOS scenarios. 64
6.63 CDF of the cluster shadowing fading, LOS scenarios. 65
6.64 CDF of the cluster shadowing fading, NLOS scenarios. 65
6.65 CDF of the LOS power factors (K-factors), LOS scenarios. Estimated from RSSI measurements with a single-antenna at the user side, no user effect. 66

7.1 An illustration of the extension of cluster visibility regions to the base station side [9]. 69
7.2 Singular value spreads of the simulated channels and measured channels. 74
7.3 Downlink sum-rates by ZF and MRC in the simulated channels and measured channels, when the average interference-free SNR at the users is 10 dB. 74
7.4 Auto-correlation in distance of the simulated channels and measured channels. . 75

List of Tables

3.1 "Open exhibition" main characteristics. 5
3.2 "Crowded auditorium" main characteristics. 6

4.1 RUSK LUND configuration parameters for massive MIMO measurement campaigns. 9

6.1 Supported user densities for outdoor measurements at sites MS 1 and MS 2. . . 15
6.2 Supported user densities for indoor measurements. 16
6.3 Expected coherence time at 3-dB, in [ms]. 32
6.4 Expected coherence bandwidth at 3-dB, in [MHz]. 32
6.5 Cluster information for all outdoor measurements. 52
6.6 Ratio of the number of single-bounce clusters and the number of all types of clusters, from indoor measurements. 58

7.1 Parameters of the outdoor measurements for the COST 2100 channel model. . . 73

Chapter 1

Introduction

In this deliverable we present the initial outcomes of the measurement campaigns and massive MIMO channel modeling efforts performed in WP1. Results are at this stage very recent and will be refined after feedback from the use of developed channel models in other work packages, primarily WP3 and WP4. We start by describing Massive MIMO channels in general and existing channel models in particular. This also includes a discussion about the necessary changes of existing MIMO channel models to incorporate the particular properties appearing when the number of antenna elements and array apertures grow. This is followed by a MAMMOET scenario discussion, where two scenarios are selected for further study. The two scenarios selected are an outdoor crowd and an indoor auditorium. Channel measurement equipment and specific configuration for the MAMMOET measurements are discussed.

The obtained channel measurements are analyzed from different points of view, with the two-fold aim of providing understanding of the massive MIMO channels in the two measured scenarios and forming a basis for comparison against channels generated by the developed channel model. The measures selected are singular-value spreads, sum-rate capacity, directional properties, and temporal behavior. These measures are then followed by multi-path component estimation and clustering, later to be used as input to the channel model.

The deliverable is concluded by a detailed description of the chosen channel modeling approach and limitations. Model parameters are selected, based on the channel measurement analysis, and the developed channel model is verified by comparing against properties of the measured channels.

Chapter 2

Massive MIMO channels

2.1 Massive MIMO propagation characteristics

When modeling the behavior of the radio channel for massive MIMO systems there are some specific phenomena that have to be taken into account as compared to conventional MIMO systems. The radio channel is of course the same, independent of system and antenna configuration used, but some propagation effects become more pronounced or more important when using physically large arrays, when using many antenna elements at the base station, and when having many closely located users. These effects are important and we need to capture detailed behavior that can explain, e.g., user separability, temporal behavior, as well as the possibilities for significant increases in energy efficiency and spectral efficiency. Among the important specific propagation effects for massive MIMO can be mentioned noticeable spherical wavefronts, variations of statistics over physically large arrays, and the limited lifetime of individual multipath components (MPCs) when a user is moving. The spherical wavefronts are important to model when physically large arrays are used at the BS because then not only directions to users and scatterers are important, but also the distances to scatterers and users. The inherent beamforming capability of massive MIMO systems makes it possible to focus the signal energy to a specific point in the environment rather than just in a certain direction. If two users are in the same direction but at different distances from the BS, the spherical wavefronts can make it possible to separate those users, also in line-of-sight (LOS). This is typically not the case for conventional MIMO using smaller antenna arrays. The variations in statistics of the received signal from a specific user over the array also contributes to the ability of user separation. The variations include, e.g., received signal power, angular power spectra, as well as power delay profile between different antenna elements [16], also in cases where they have identical antenna patterns aimed in the same direction. Variations of the angular power spectra can be characterized by the so-called spatial fingerprints [7]. The limited lifetime of individual MPCs is another important effect to consider when analyzing user separability of closely located users. In conventional MIMO models, as discussed in next section, all the scatterers in a cluser are visible from all positions in the visibility region of the cluster. In practice this is, however, not the case. Each of the MPCs typically has a limited area inside the visibility region where they can be seen. Clusters provide a very effective way of modeling antenna correlation for a single user, but our observations show that conventional MIMO models tend to overestimate correlation between users in massive MIMO systems.

2.2 Channel models

2.2.1 Existing conventional MIMO models

We consider the group of channel models called Geometric Stochastic Channel Models, (GSCMs) as those provide a natural way to capture and describe correlation effects between users and between antenna elements in a straightforward way through the concept of clusters and visibility regions. Within the group of GSCMs there are two basic approaches having the same origin (the COST 259 model): the COST 2100 approach and the WINNER approach. In the COST 2100 [12] approach the scatterers have fixed physical positions in the simulated environment, whereas in the WINNER [11] approach the channel simulation is based on angles to the scatterers. From a massive MIMO perspective the latter has the drawback that the angles vary as long as we are not in the far field of the array; hence we have to include this in the model. Due to this reason and since we aim for a consistent model showing realistic correlations between users in a massive MIMO context we use the COST 2100 modeling approach where the clusters and scatterers are described by their physical locations rather than their directions in the simulation area. The extensions we propose are in general not specific to massive MIMO only but can be useful to realistically represent physical propagation mechanisms when taking wireless communication beyond the conventional cellular scenario with one or several base stations. The concepts introduced should, e.g., be useful also for peer-to-peer channels or when developing models for radio based positioning. However, in the reminder we focus on the massive MIMO scenario with one base station equipped with many antennas and several users having mobile stations with one or a few antennas.

One should also mention that there are theoretical geometrical model proposals in the literature, see e.g. [21]. As we aim for a model connected to a physical environment those models are out of scope of our investigation, though these theoretical models can provide useful insights into, e.g., correlation characteristics. Ray-tracing based investigations and models can also provide useful insights for system design and performance assessment, but those models are also out of scope of our investigation here.

2.2.2 Necessary model extensions

The model we aim for has a cluster centric approach, where the visibility regions belong to the clusters and both visibility regions and clusters are randomly placed in the simulation area according to specific distributions. We introduce visibility regions (VRs) at both sides of the link, both for the BS and for the MS. As the visibility regions belong to the clusters and not to the base station we get a more symmetric approach which has many advantages in scenarios with multiple base stations, with or without massive MIMO, and also for peer-to-peer communication such as vehicle-to-vehicle or device-to-device communication. For the model it is important to be backwards compatible with the conventional COST 2100 model, which in this case this can be achieved by setting the size of the base station visibility regions to infinity, so that all BS antennas see all the clusters that are active from the mobile side, i.e. clusters where the users are inside the corresponding MS visibility regions.

From a massive MIMO perspective it is important to capture the effect that not all multipath components are visible in the whole VR. Therefore we introduce the concept of gain functions of the MPCs within the cluster. The gain function is a smooth function allowing power variations of single MPCs within the cluster. As a first approach we use gain functions that have a Gaussian shape. The width of the gain function (determined by the standard deviation of the Gaussian function) controls the variability of the MPC gain within the visibility function. Each

MPC has its own gain function and the specific gain function of an MPC has a peak location (in 2D or 3D as discussed below) within the VR. For a specific user location the Euclidean distance to the peak of the gain function is calculated and the gain of the MPC is given as a function of this distance. The gain function has also the advantage that it can be used to create sub-clusters out of clusters if this is desired. This is achieved by having correlated locations of the peaks of the gain functions with closely located scatterers in the cluster. Backwards compatibility with the conventional COST 2100 model is achieved by setting the variance of the gain function to infinity so that there are no variations at all for the gain of a single MPC inside the VR.

A third extension that we think is necessary is to also have a 3D extension of the conventional COST 2100 model. As large antenna arrays are envisioned for the base station it is quite likely that those arrays have some kind of 2D structure and hence have good resolvability and beamforming capability both in elevation and azimuth. The whole modeling framework should be extended to 3D so that locations of users, clusters, visibility regions, base station(s) are described in 3D. Backward compatibility is achieved by projection of the 3D parameters on the ground floor.

Chapter 3

Measured MAMMOET scenarios

3.1 MAMMOET scenario overview

The measurements and analysis focus on two of the important MAMMOET scenarios identified in [D1.1], namely Scenario 1: open exhibition and Scenario 4: Crowded auditorium.

According to [D1.1.] Scenario 1: open exhibition consists of outdoor-deployed (macro) BSs serving outdoor-located UEs. UEs with high density are randomly distributed and moving at pedestrian speeds. UEs locations are in principle completely random, although some correlation may exist for both the UEs positions and the traffic patterns at specific times and/or locations.

Table 3.1: "Open exhibition" main characteristics.

Parameter	**Value**
Propagation environment	Outdoor
Cell geometry / size	Irregular, delimited geometry / medium to large
UE distribution	Random, but clustered, with high density
UE speed	Up to 7 km/h
LOS/NLOS	Both
Shadow fading	Present
Channel model	COST2100
METIS relation	TC9 "Open air festival"
Examples	Outdoor conference center, crowded square

One of the most important aspects to analyze and model is the user separability of closely spaced users, possibly with many other (passive) people being around acting as scatterers or shadowing objects and thus interacting with the nearby MS antenna. In this scenario it is of uttermost importance to include the effect of the user hand, the user body and the user antenna. From a measurement perspective we downscale the scenario to capture the essential characteristics by a group of users being closely located, with or without other people being around, simultaneously communicating with a macro BS in LOS or NLOS. In our measurements we have 9 users all being within a circle of 5 m diameter moving randomly holding the MS in browse mode in front of the body with one hand.

Scenario 4: Crowded auditorium provides the indoor counterpart of the outdoor Scenario 1, in which both the UEs and BSs are, respectively, located and deployed indoors. The UEs are randomly distributed with high density, possibly with correlated UEs positions and traffic patterns. The UEs are almost static in most cases and NLOS propagation conditions are

expected. A subcase may be considered in which the UEs are static, placed at deterministic locations (e.g., seats in a concert hall) and channels contain LOS components.

Table 3.2: "Crowded auditorium" main characteristics.

Parameter	**Value**
Propagation environment	Indoor
Cell geometry and size	Determined by scenario boundaries
UE distribution	Random, but clustered, with high density
UE speed	Mostly static, up to 3 km/h
LOS/NLOS	Both
Shadow fading	Not present
Channel model	COST2100
Examples	Indoor conference center, office, concert hall, indoor arena
METIS relation	TC1: "Virtual reality office", TC3 "Shopping mall", TC4: "Stadium"

Again, we capture the essential characteristics of this scenario by downscaling it to a case with a group of closely located simultaneous indoor users in a lecture theater communicating with a BS mostly in LOS but with some obstructions. The users are seated regularly with and without other passive users around them acting as scattering and shadowing objects. As opposed to the outdoor case we expect larger angular spreads due to more interaction with the indoor walls and hence less dominant LOS component. The users hold the MS in browse mode with one hand in front of the body, all users face the same directions, but with varying directions of the MS in front of the body.

3.2 Scenario selection

The reason for focusing on the "Open Exhibition" and "Crowded Auditorium" scenarios is first of all their importance, but also the possibility to conduct high quality measurements in reasonably controlled areas. The outdoor-to-indoor scenarios are also among the more interesting scenarios, but they also provide some severe challenges in terms of finding representative building structures and in terms of getting enough signal power at the receivers given the available measurement equipment. For the future it would be highly interesting to also characterize those environments, but with the limited measurement resources we focused on two key scenarios, that are seen as crucial for future 5G deployment, where we also had good control of received power levels to make meaningful analysis. We see those measurements and models as a starting point for massive MIMO models below 6 GHz, more measurement and characterization efforts are needed to fully understand and model the behavior of the radio channel and once a more comprehensive view of the massive MIMO channel behavior is available the models and channel characteristics presented here can and should probably be refined.

Chapter 4

Channel measurement setups

In this chapter we describe the measurement equipment and configuration parameters used for MAMMOET measurement campaigns.

4.1 Measurement equipment

Measurement campaigns for massive MIMO channel modeling were performed using a 128-port cylindrical antenna array at the BS side, shown in Fig. 4.1. The array consists of 64 dual-polarized patch antenna elements distributed in four rings. The rings are stacked on top of each other. The spacing of adjacent elements is half a wavelength at 2.6 GHz. At the user side, we use nine single-polarized omni-directional antennas, of type SkyCross SMT-2TO6MB-A, acting as nine simultaneous users. Note that, although the antennas are vertically polarized and omni-directional in azimuth when measured without users, the radiation pattern and polarization including the users is more complex and is dependent on the exact position of antenna and users. During the measurements the antennas are held in front of the users with approximately 45 degree down tilt.

Measurements were recorded using the RUSK LUND MIMO channel sounder [20]. The sounder consists of a transmit unit (Tx) and a receive unit (Rx), which can operate untethered and be placed at separate locations. The transfer function of the radio channel is measured for all the Tx-Rx antenna pair combinations. At any given time, the measured channels provide an instantaneous description, or *snapshot*, of the double-directional radio channel [18]. Snapshots are taken at a fixed rate in order to track temporal variations of the radio channel. The required sampling rate, f_s, for aliasing-free measurements depends on the mobility of the users, on the selected carrier frequency and, of course, on the environment, and is given by the expression

$$f_s \geq 2\nu_{\max},$$

where $\nu_{\max}$ is the maximum Doppler shift of the channel [14]. For example, for the outdoor measurement campaigns presented in this document, 1152 channel combinations (9 users times 128 BS antennas ports) are sampled 17 times per second, allowing a maximum user velocity of 0.5 meters per second at 2.6 GHz; higher user velocities may result in aliasing of the sampled signal. In this example, we consider the worst case of two users moving towards each other, and we have assumed that the environment is static for the duration of the measurement.

It is also worth mentioning that the RUSK LUND MIMO channel sounder falls into the category of *multiplexed array* channel sounders. This means that the multiple Tx-Rx channel combinations are not measured simultaneously. Instead, each Tx-Rx antenna pair combination

Figure 4.1: (a) The cylindrical array with 128 ports. (b) View from site MS 2.

is measured separately, in rapid succession. At each link end, a fast switch selects the Tx/Rx antenna port of the MIMO channel currently being measured.

The user antennas are connected through optical fibers to the transmit unit of the RUSK LUND MIMO channel sounder [20]. All optical links have a length of 200 meters.

4.2 Configuration for MAMMOET measurements

For the massive MIMO measurement campaigns, the BS was acting as the transmitter and the users were acting as receivers. Measurements were recorded using a center frequency of 2.6 GHz and 40 MHz bandwith. Each measurement took 17 seconds, and 300 snapshots were recorded during this time. The sounding signals were transmitted with 0.5 W output power. Tab. 4.1 summarizes the main configuration parameters for the MAMMOET measurement campaigns.

Fig. 4.2, left, shows a user holding the user equipment (UE) box and the UE antenna. To the right, several users at site MS 8 are connected to the RUSK LUND transmit unit through dedicated optical links.

Figure 4.2: (a) A user holding the MS user equipment antenna with an inclination of 45°. (b) Users moving randomly within the five-meter diameter circle.

Parameter	**Value** (indoor/outdoor)
f_c	2.6 GHz
BW	40 MHz
N_{channels}	129/257
T_{sounding}	3.2/6.4 μs
T_{snap}	$2 * 9 * 128 * T_{\text{sounding}}$
N_{snap}	300
T	17 s
P_{out}	27 dBm
45° tilt on UE antennas	

Table 4.1: RUSK LUND configuration parameters for massive MIMO measurement campaigns.

Chapter 5

Measurement campaigns

Propagation measurements were performed for two MaMi scenarios reflecting both the outdoor and the indoor environments. The chosen scenarios are the "Open Exhibition" scenario (outdoor), and the "Crowded Auditorium" scenario (indoor). In both scenarios, a 128-port cylindrical antenna array at the BS side is used to serve 9 closely-located users each of which is equipped with an omni-directional antenna. Depending on the scenario, different positions for the BS antenna, and different users' antenna polarizations are considered.

5.1 Open Exhibition

This scenario consists of an outdoor-deployed micro BS serving outdoor closely-located UEs. The measurement campaign took place at the campus of Lund University, Lund, Sweden. The propagation measurement can be best described as suburban environment having detached buildings with two to five floors and open areas with modest vegetation.

To emulate the case of having high user density, the 9 users were moving inside a small circle with a diameter of 5 m, which represents a density of 2.18 m^2 per user. Besides performing the measurements with only having 9 active users inside the circle, we considered the case of having heavy crowd where another 10 to 12 persons were moving around the 9 active users inside the circle. All the 9 users and the crowd (if any) were moving randomly with a speed about 0.5 m/s inside the circle. In all cases, the users were asked to tilt their antennas by about 45 degrees to mimic the data mode position.

Fig. 5.1 shows an aerial photo of the measurement area, with coordinates (lat,lon)=(55.71158, 13.21038). The performed measurements consisted of several runs with different BS positions and propagation conditions:

- Positions of the BS. Two BS positions with different heights were considered: low roof of two floors, and high roof of five floors. However, for the current deliverable, only the measurements with the BS at the low roof are analyzed.
- Propagation condition. Five positions, with different propagation conditions, for the users were considered. MS 1 and MS 2 have LOS condition. MS 8 and MS 10 have NLOS conditions. For this deliverable, only the LOS cases are analyzed.

Considering only the MS 1 and MS 2 positions with the low roof BS position, a total of eight measurement runs were performed, four runs per position, two of which are with the presence of the extra crowd and two runs without the crowd.

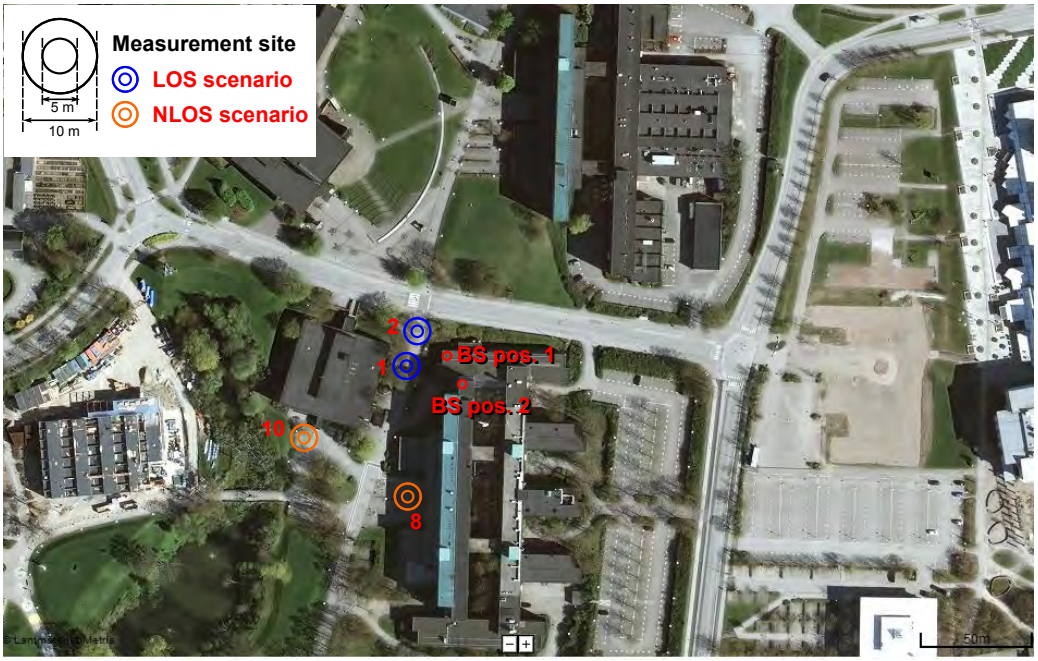

Figure 5.1: Aerial photo of the measurement area. Base station locations are indicated by the label BS. The different positions of the mobile users are labeled by MS 1, MS 2, MS 8 and MS 10, and indicated by the circles. MS 1 and MS 2 have LOS condition. MS 8 and MS 10 have NLOS condition.

5.2 Crowded Auditorium

This scenario represents the indoor counterpart of the above discussed outdoor scenario. The propagation measurements were performed in an auditorium, where 9 active users were seated randomly in two positions, either at the middle or at the back of the auditorium. Each position consists of 20 seats (4 rows by 5 columns). For each measurement run, the 9 users are seated at one position and assigned random seats. In some measurement runs, the rest of the 20 seats at each position remained empty (i.e., no crowd), or got occupied by non-active users in order to capture the effect of having heavy crowd. During the measurement, the users are asked to move their antennas randomly with a speed not more than 0.5 m/s in order to mimic different orientations and shadowing effect. Four different positions for the BS are considered as seen in Fig. 5.2. The height of the BS antenna array was fixed at 3.2 m. For each users' position, for each BS position, two measurement runs were performed: one with the users holding their antennas vertically, and the other with the users holding their antennas tilted 45 degrees. For the analysis reported in this deliverable, only one position of the users (at the back of the auditorium) and two positions of the BS (BS 1, and BS 3) are analyzed.

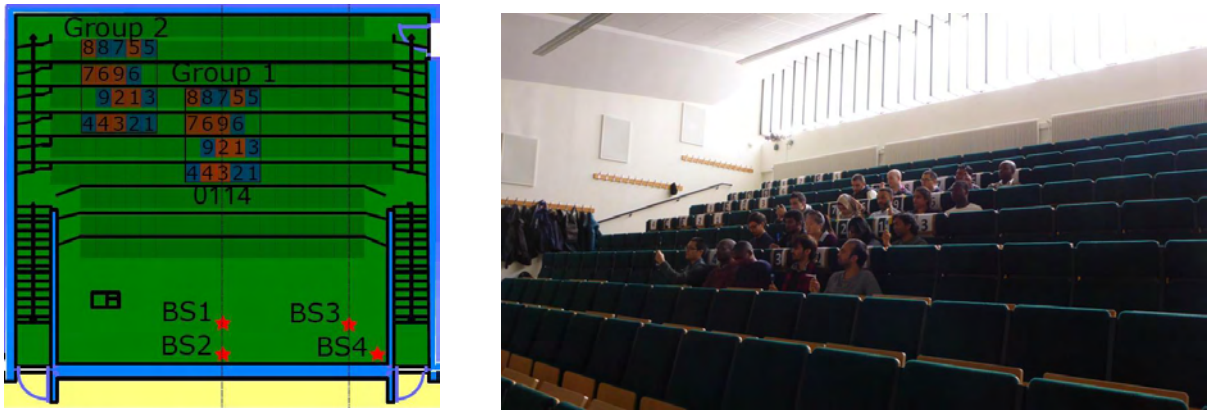

Figure 5.2: Crowded auditorium measurement. (a) Base station locations are indicated by the label BS. Users positions are indicated by Group 1 (back), and Group 2 (middle). (b) A measurement run with 9 active users surrounded with 11 non-active users (crowd).

Chapter 6

Measurement data analysis

This chapter contains plots illustrating system or propagation aspects typical of massive MIMO. Plots for different scenarios (see Chapter 3) are presented and compared. In Sec. 6.1 we look at the singular value spread of measured massive MIMO channels, and in Sec. 6.2 we consider the sum-rate capacity that can be extracted from such channels. Sec. 6.3 introduces directional analysis and multipath component (MPC) extraction. Then, Sec. 6.4 deals with the temporal behavior of massive MIMO channels. Finally, Sec. 6.5 offers a detailed review of the clustering results obtained from the measured data.

6.1 Singular value spreads

This section presents some plots illustrating singular value spreads of measured massive MIMO radio channels. For this analysis we use each of the measured frequency-flat sub-channels for further processing. Let

$$\mathbf{H} = \mathbf{U}\mathbf{\Sigma}\mathbf{V}^{\mathrm{H}} \tag{6.1}$$

be the singular value decomposition of the channel matrix $\mathbf{H}$, where $\mathbf{U} \in \mathbb{C}^{K\times K}$ and $\mathbf{V} \in \mathbb{C}^{M\times M}$ are unitary matrices and $\mathbf{\Sigma} \in \mathbb{C}^{K\times M}$ is a diagonal matrix containing the ordered singular values of the channel, $\sigma_1 \geq \ldots \geq \sigma_K \geq 0$. We define the *singular value spread* of the matrix $\mathbf{H}$, denoted by κ, as the ratio between its largest and smallest singular values, i.e.

$$\kappa = \frac{\sigma_1}{\sigma_K}. \tag{6.2}$$

It follows that $1 \leq \kappa \leq \infty$. Values of κ close to 1 indicate nearly full user orthogonality while, under the assumption of equal average channel gain for all users, large values of κ imply a strong linear dependency of, at least, two of the rows in $\mathbf{H}$ and, thereupon, a relative difficulty in the spatial separation of the corresponding users. The singular value spread of $\mathbf{H}$ is also referred to as the *condition number* of $\mathbf{H}$.

6.1.1 Effect of the number of BS antenna ports on the singular value spread

Fig. 6.1 shows the cumulative distribution function (CDF) of the singular value spreads measured for an indoor auditorium deployment (BS 1, users at the back), Fig. 5.2, and an outdoor suburban microcell deployment (site MS 2), Fig. 5.1. The singular value spread has been converted to logarithmic units according to

$$\kappa_{\mathrm{dB}} = 10\log_{10}(\kappa). \tag{6.3}$$

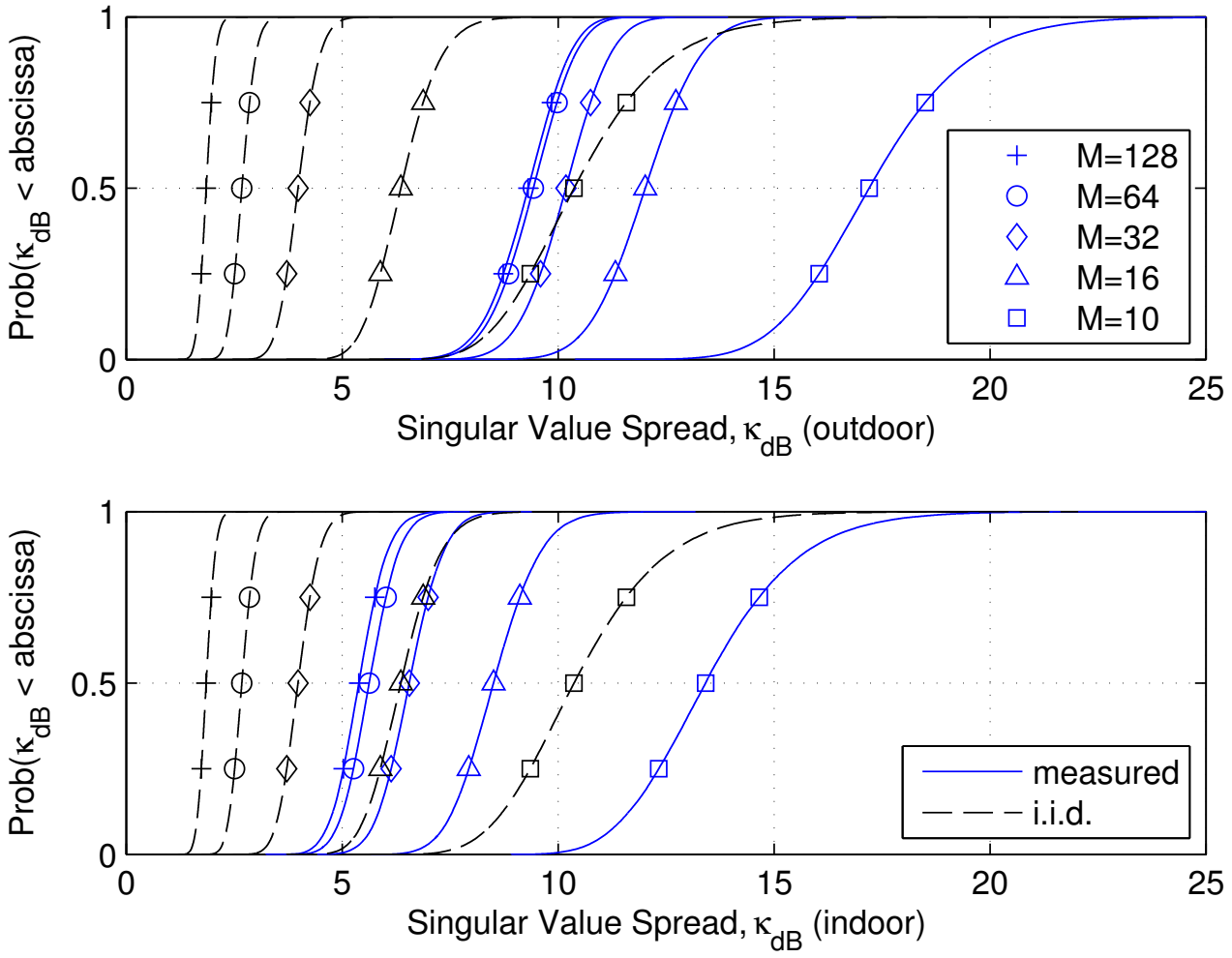

Figure 6.1: CDFs of the singular value spread when using 128, 64, 32, 16 and 10 antenna ports at the BS (in logarithmic units). The BS communicates simultaneously with nine users in the presence of crowd. Plots correspond to outdoor (top) and indoor (bottom) environments. For comparison purposes, CDFs of the singular value spread of i.i.d. Rayleigh channels with the same number of antenna elements are also given. (The legend is shared between both figures.)

To illustrate the effect of equipping the BS with a large number of antennas, CDFs when using 10, 16, 32, 64 and 128 antenna ports at the BS are shown. In this example, the BS communicates simultaneously with nine active users, which are surrounded by 11 additional, passive users. Note that 128 antenna ports correspond to using the full array, while a configuration with 10 antenna ports is representative of conventional MU-MIMO.

We see that user channels decorrelate as the number of antenna ports at the BS increases. For example, when going from 10 antenna ports (conventional MU-MIMO) to 128 antenna ports (massive MIMO), the median of the singular value spread decreases by 8 dB, approximately, in both indoor and outdoor environments. Furthermore, we also observe a hardenning of the radio channel, evidenced by the CDFs becoming steeper as the number of antenna ports at the BS increases. These observations are in good agreement with known theoretical results on the massive MIMO channel [13, 17]. There is, however, a considerable gap between the median of the singular value spread of measured channels and that of i.i.d. Rayleigh channels. This gap is specially large in the case of outdoor measurements. We also notice that, for the same number

of BS antenna ports, users are better separated in indoor environments.

Another interesting observation that we can make from Fig. 6.1 is that improvements to the singular value spreads when using more than 64 antenna ports are modest in comparison to an i.i.d. Rayleigh channel. This observation applies to both indoor and outdoor measured environments.

Although not shown in Fig. 6.1, we end this section with an important remark on the role of diversity in polarization. Based on the measurement data collected, we observe that, for the environments studied and for the BS antenna array and UE antennas used, the median of the singular value spread when using M single-polarized antenna ports (i.e. only vertically- or only horizontally-polarized antenna ports) amounts roughly to that of an array using only $M/2$, but with both polarizations present in equal proportions. In other words, when polarization diversity is not present, half of the antenna ports have a zero net contribution.

6.1.2 Effect of the density of users on the singular value spread

We adopt the "user density" as an indication of the degree of "closeness" of the users. We recall that, for both indoor and outdoor measurements, users are confined to a limited area. Within this area we find users engaged in communication with the BS. In some of the measurements, we also find "passive" users (crowd), which do not transmit any RF signal. We compute the user density as the number of active *and* passive users divided by the size of the confining area, and is given in users per m^2. Passive users, although not transmitting any RF signal, have an influence on the properties of the radio channel between the active users and the BS. It is reasonable to expect that the significance of this influence will depend on the user density.

The measurements collected support various user densities, which are detailed in Tab. 6.1 and Tab. 6.2. Some remarks are in order. In outdoor scenarios, user densities of 0.1 and 0.2 users per m^2 are achieved with two and three active users, respectively. In this case, when reporting on a number of scheduled users greater than two (three), virtual users have been used. This is, user channels from sequential measurements have been brought together. All measurements concerned with virtual users were recorded with a ten-minutes time interval, and users were continuously moving during this time. For indoor scenarios, 0.0 users per m^2 implies that measurements were carried out in complete absence of users and crowd, with the antennas attached to the seat backs.

User density $[m^{-2}]$	**Active users**	**Crowd**	**Area** $[m^2]$
1.0	9	11	19.6
0.5	9	None	19.6
0.2	3	None	19.6
0.1	2	None	19.6

Table 6.1: Supported user densities for outdoor measurements at sites MS 1 and MS 2.

An additional metric, namely, the normalized parallel channel gain (NPCG), γ, is introduced in this section (see [2]). The NPCG is defined as

$$\gamma = \frac{1}{\sigma_1^2} \sum_{k=1}^{K} \sigma_k^2, \tag{6.4}$$

and can be interpreted as the gain of the MIMO channel relative to the gain of the strongest channel mode. The NPCG takes values between 1, for rank-1 channels, and K, for full-rank

User density $[m^{-2}]$	**Active users**	**Crowd**	**Area** $[m^2]$
2.2	9	11	8.9
1.0	9	None	8.9
0.0	None	None	8.9

Table 6.2: Supported user densities for indoor measurements.

ideal channels (user channels perfectly orthogonal and with equal gain). Note, however, that $\gamma(\mathbf{H})$ can take values arbitrarily close to 1 for full-rank matrices $\mathbf{H}$.

The median of the normalized parallel channel gain and the singular value spread in several measured scenarios are illustrated in Fig. 6.2 through Fig. 6.7. For each curve, a point is computed as the median of the corresponding metric (i.e. κ or γ) for a certain number of scheduled users. When the number of scheduled users is less than nine, users are selected randomly from a uniform distribution.

The following observations can be made.

- For any number of scheduled users, indoor measurements display lower values of the singular value spread and larger values of the normalized parallel channel gain, compared to outdoor measurements. In other words, for the measured channels, users are easier to separate in indoor environments.
- For outdoor measurements, plots for sites MS 1 and MS 2 show only minor differences.
- In the same way, for indoor measurements, the location of the BS antenna array (BS 1 or BS 3) and the location of the users (at the back or at the center of the auditorium) has only a minor effect on the median values of the metrics considered.
- In both environments, user separability degrades with an increasing number of scheduled users, and it does so at a faster rate than in the i.i.d. Rayleigh channel case.
- With regard to the effect of user density on user separability, variations observed are small (less than 10%, save for the case displayed in Fig. 6.5), and it is not clear if an increased user density is beneficial or adverse to the ability of massive MIMO systems to separate closely spaced users. For example, in Fig. 6.2 a higher user density (compare 0.1 users/m^2 and 1.0 users/m^2) yields a lower singular value spread while, in Fig. 6.3, the opposite trend is observed. A similar case is seen in Fig. 6.4 and Fig. 6.5, for indoor measurements[1]. Hence, further investigations are needed in order to clarify this point.

In summary, we can say that, in massive MIMO systems, the singular value spread of the radio channel is kept below 10 dB in outdoor deployments, and below 6 dB in indoor deployments. These values enable spatial separation of users at the BS using linear precoders (see next section).

6.2 MRT and ZF capacity

In this section, we consider the downlink of a massive MIMO system and examine the achievable sum-rate capacity based on the measured radio channels. Furthermore, we look into the sum-rates that can be achieve with less expensive linear precoders.

[1]See, however, the limitations that apply to Fig. 6.5.

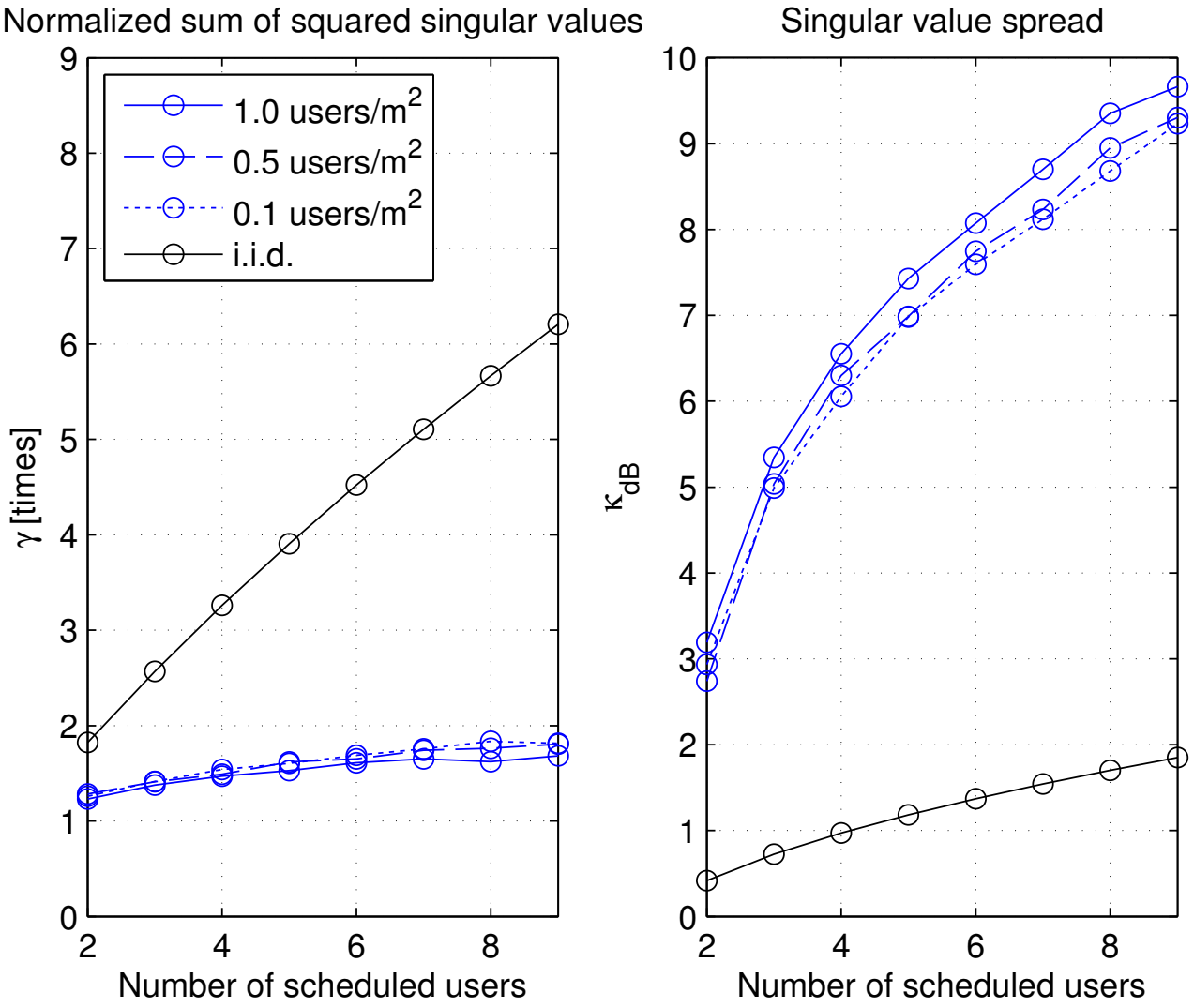

Figure 6.2: Median of the normalized parallel channel gain (left) and singular value spread (right), in logarithmic units, when using 128 antenna ports at the BS in an outdoor, microcell deployment (site MS 2). Various numbers of scheduled users and user densities are considered. For comparison purposes, median values of the singular value spread and normalized parallel channel gain of i.i.d. Rayleigh channels with the same number of users also given.

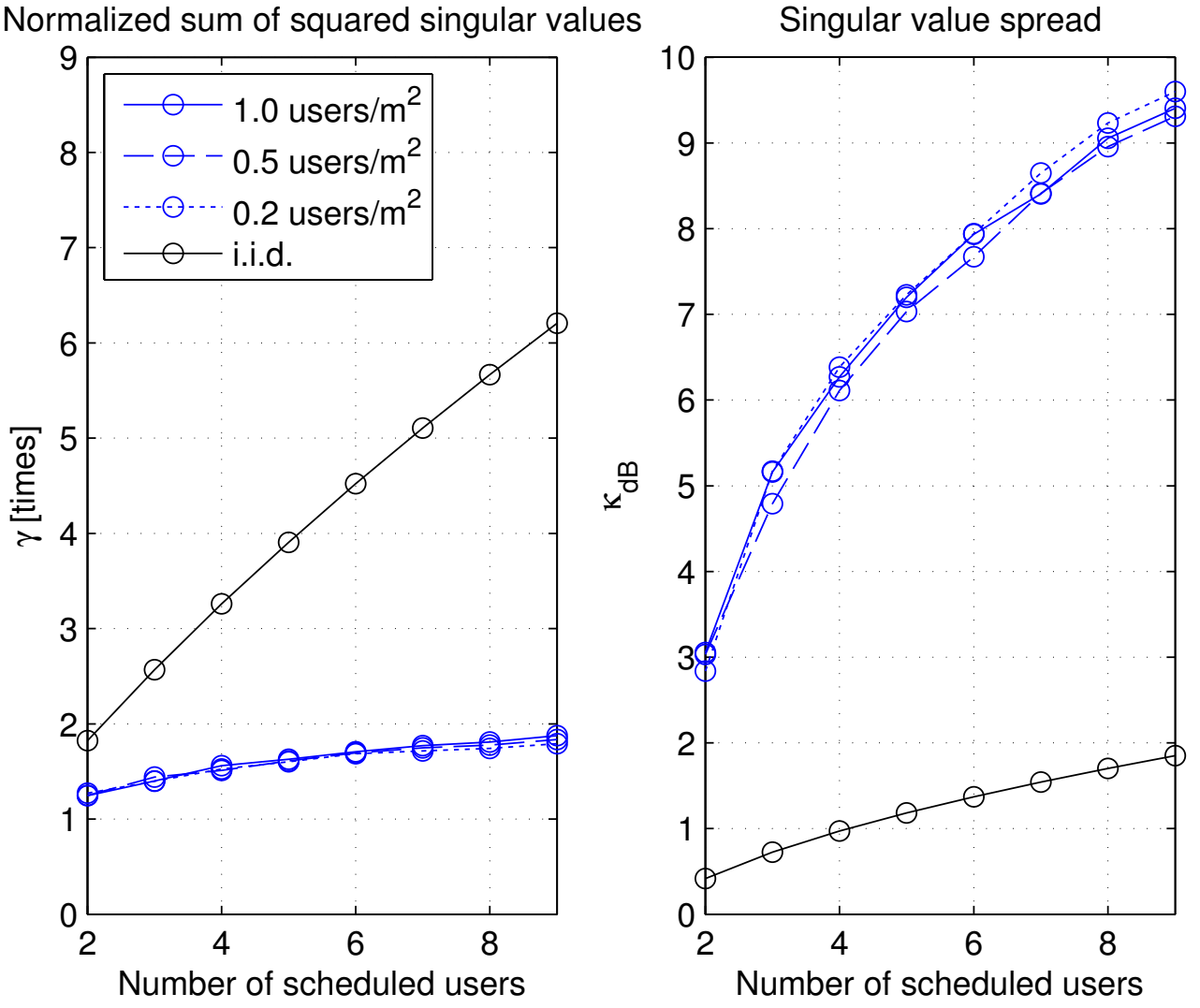

Figure 6.3: Median of the normalized parallel channel gain (left) and singular value spread (right), in logarithmic units, when using 128 antenna ports at the BS in an outdoor, microcell deployment (site MS 1).

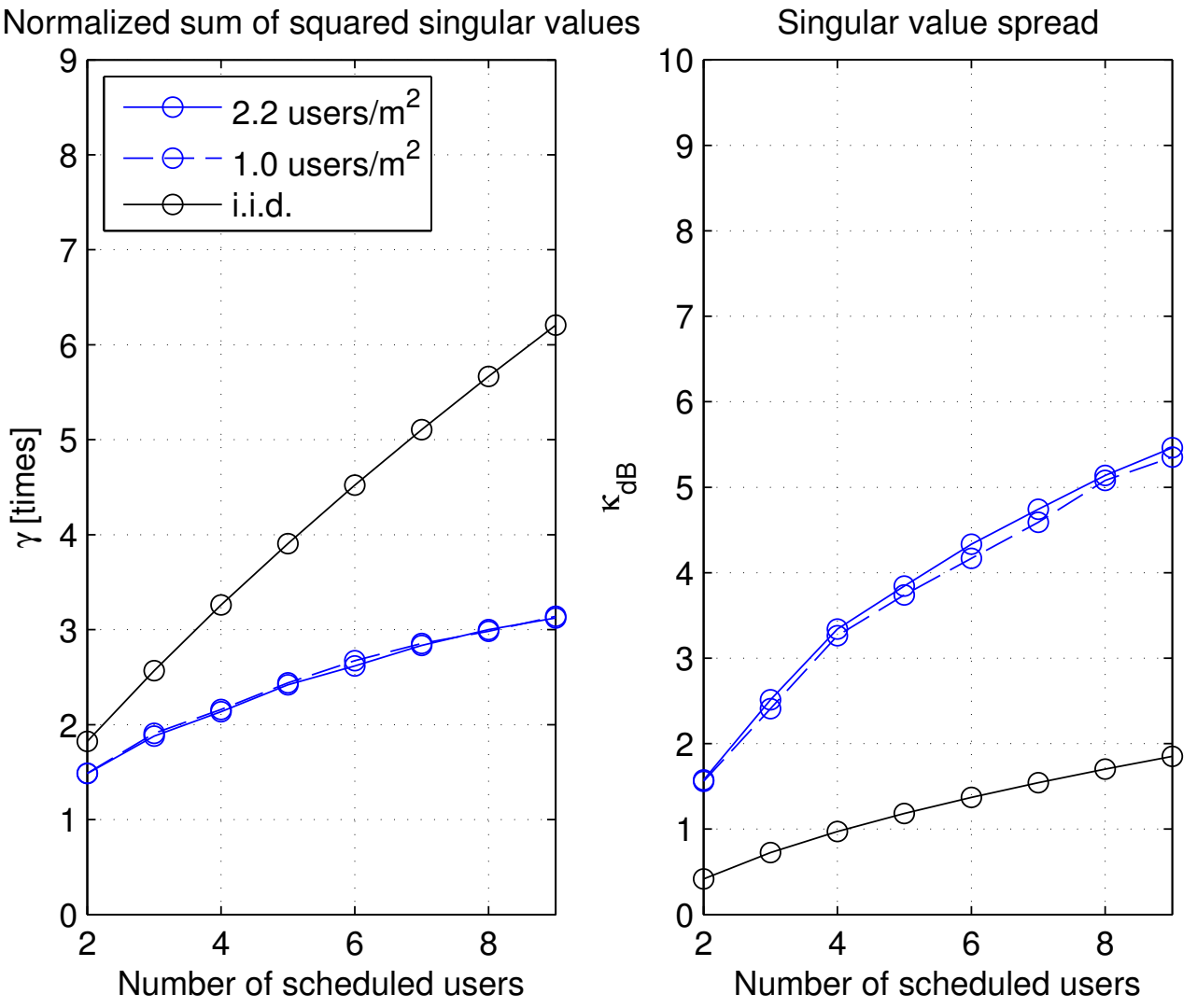

Figure 6.4: Median of the normalized parallel channel gain (left) and singular value spread (right), in logarithmic units, when using 128 antenna ports at the BS in an indoor auditorium deployment (BS 1, users at the back).

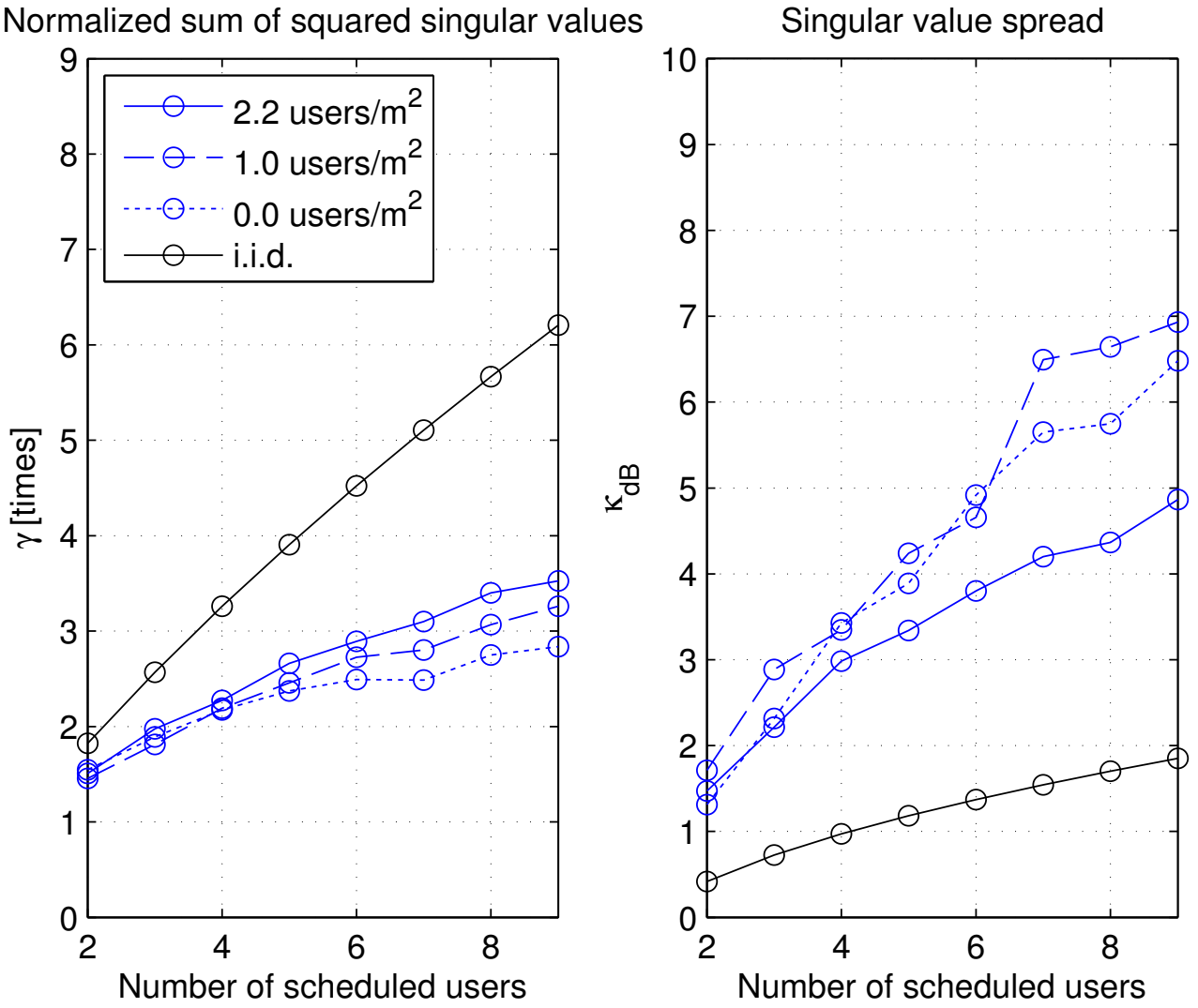

Figure 6.5: Median of the normalized parallel channel gain (left) and singular value spread (right), in logarithmic units, when using 128 antenna ports at the BS in an indoor auditorium deployment (BS 1, users at the center).

NOTE. Several limitations apply to this figure. First, the measurement data corresponding to the user density of 1.0 users/m^2 were obtained after a restart of the measurement equipment and, therefore, this measurement might suffer from a loss of accuracy. Second, the measurement data for the density of 0.0 users/m^2 were acquired on a different measurement occasion. In this case, the positions of UE antennas and BS are only approximate.

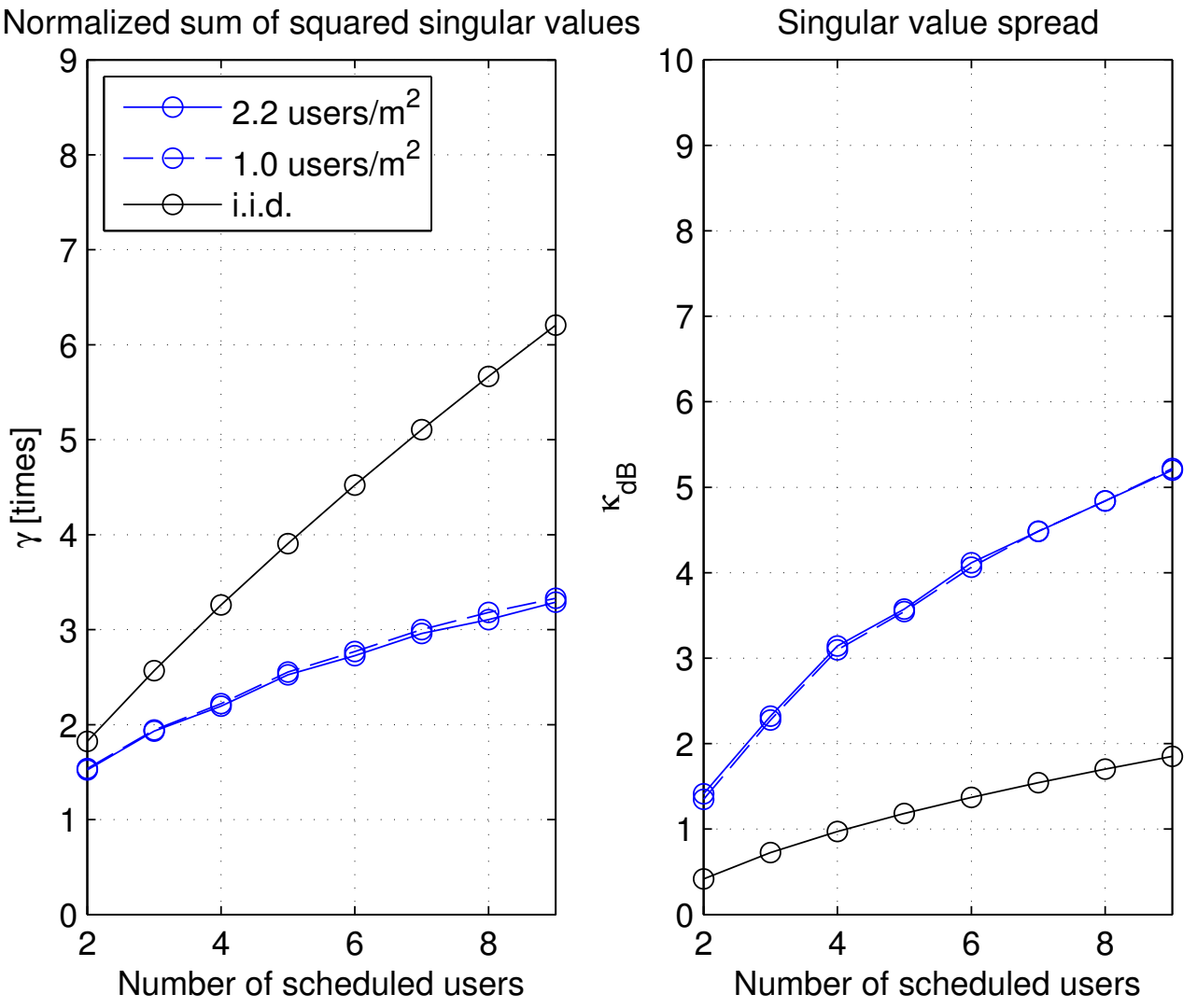

Figure 6.6: Median of the normalized parallel channel gain (left) and singular value spread (right), in logarithmic units, when using 128 antenna ports at the BS in an indoor auditorium deployment (BS 3, users at the back).

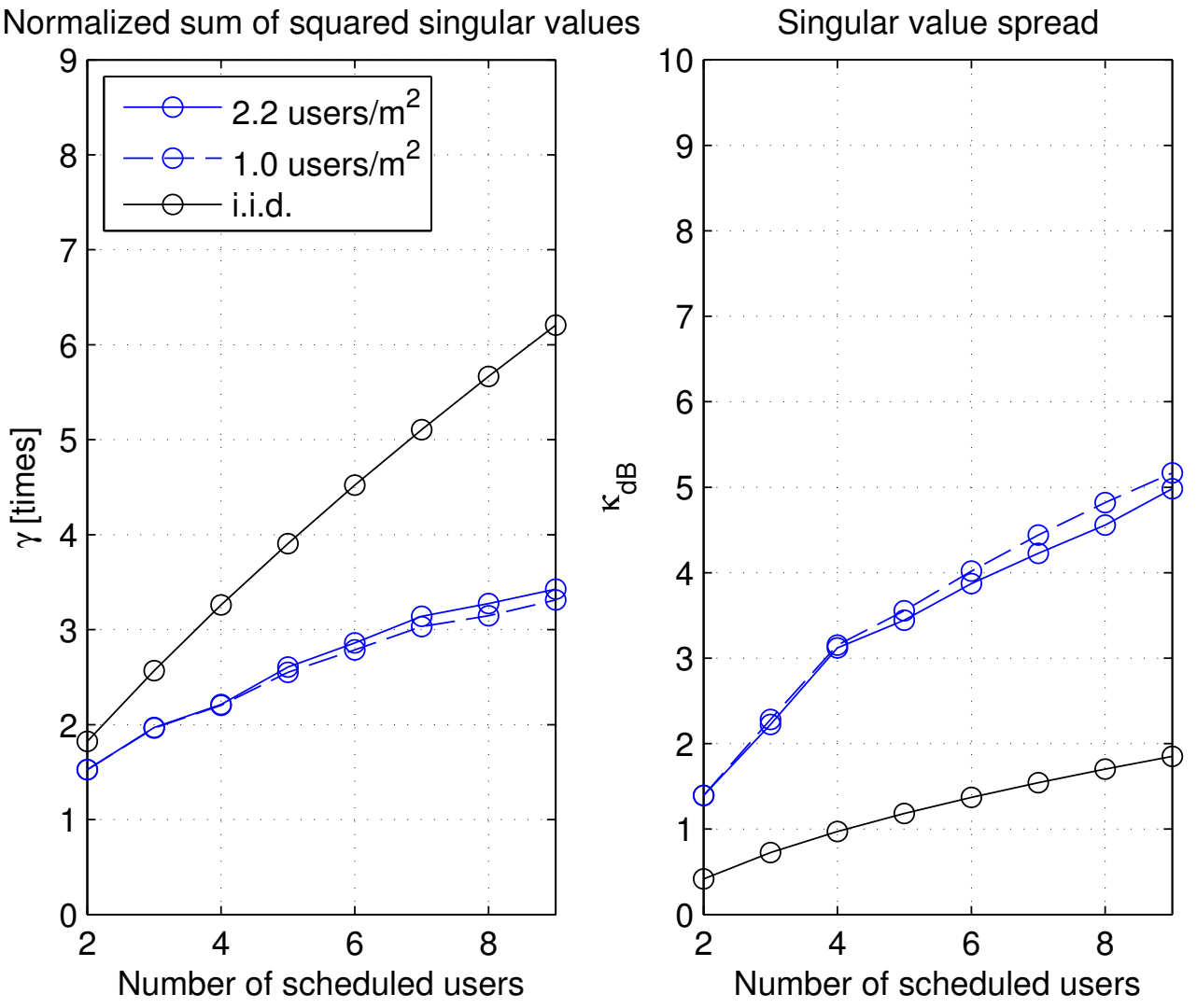

Figure 6.7: Median of the normalized parallel channel gain (left) and singular value spread (right), in logarithmic units, when using 128 antenna ports at the BS in an indoor auditorium deployment (BS 3, users at the center).

The sum-rate capacity of the narrowband MU-MIMO downlink channel with full channel state information at the BS is given by

$$C_{\mathrm{DPC}} = \max_{\{\gamma_k\}} \log_2 \det(\mathbf{I}_M + \mathbf{H}^{\mathrm{H}}\mathbf{D}\mathbf{H})$$
$$\text{subject to} \quad \sum_{k=1}^{K} \gamma_k = P, \quad \gamma_k \geq 0, \quad \forall k, \tag{6.5}$$

with $\mathbf{D} = \mathrm{diag}(\gamma_1, \ldots, \gamma_K)$ and P the total transmit power available at the BS. Problem (6.5) is a convex problem and can be efficiently solved, for instance, by means of the sum-power iterative waterfilling algorithm described in [10].

The sum-rate capacity of the narrowband MU-MIMO downlink channel can be achieved by dirty-paper coding (DPC) [3]. However, the high computational complexity of DPC renders it impractical even for a low number of users. As an alternative to DPC, we consider linear precoding schemes of the form

$$\mathbf{s} = \mathbf{W}\mathbf{x}, \tag{6.6}$$

where $\mathbf{W} \in \mathbb{C}^{M \times K}$ is the precoding filter and $\mathbf{x}$ is the $K \times 1$ vector containing the user data streams. We look at the performance of the popular zero forcing (ZF) and maximum ratio transmission (MRT) linear precoders [15]. The ith column of the ZF prefiltering matrix, $\mathbf{w}_{\mathrm{ZF},i}$, is given by

$$\mathbf{w}_{\mathrm{ZF},i} = \frac{\mathbf{h}_i^{(\dagger)}}{\sqrt{\|\mathbf{h}_i^{(\dagger)}\|_{\mathrm{F}}^2}}, \tag{6.7}$$

where $\mathbf{h}_i^{(\dagger)}$ is the ith column of $\mathbf{H}^{\mathrm{H}}(\mathbf{H}\mathbf{H}^{\mathrm{H}})^{-1}$, the pseudo-inverse of the MU-MIMO channel matrix. The ith column of the MRT prefilter matrix, $\mathbf{w}_{\mathrm{MRT},i}$, is given by

$$\mathbf{w}_{\mathrm{MRT},i} = \frac{\mathbf{h}_i^{\mathrm{H}}}{\sqrt{\|\mathbf{h}_i\|_{\mathrm{F}}^2}}. \tag{6.8}$$

Optimal allocation of transmit power to the user data streams in $\mathbf{x}$, subject to a sum-power constraint

$$\sum_{k=1}^{K} \gamma_k = P,$$

has been performed by means of numerical methods. For the ZF precoder, the product $\mathbf{H}\mathbf{W}_{\mathrm{ZF}}$ is diagonal and optimal power allocation can be achieved by simple water filling [19]. The MRT precoding case, however, constitutes a non-convex problem and the numerical methods used in the preparation on this work do not guarantee the optimality of the transmit power allocations thus obtained.

Fig. 6.8 shows the sum-rate capacity and sum-rates with ZF and MRT precoding filters for several user densities and two deployments, namely, indoor auditorium and outdoor suburban microcell. In this example, all 128 antenna ports are used. We can see that massive MIMO with ZF achieves a large fraction of the sum-rate capacity. For example, at SNR = 10 dB, 70% of the sum-rate capacity is achieved with ZF precoding, in the outdoor case, and this figure increases to 90% for indoor measured channels. We also note that, for the DPC and ZF cases, the achievable sum-rates are largely independent of the user densities considered.

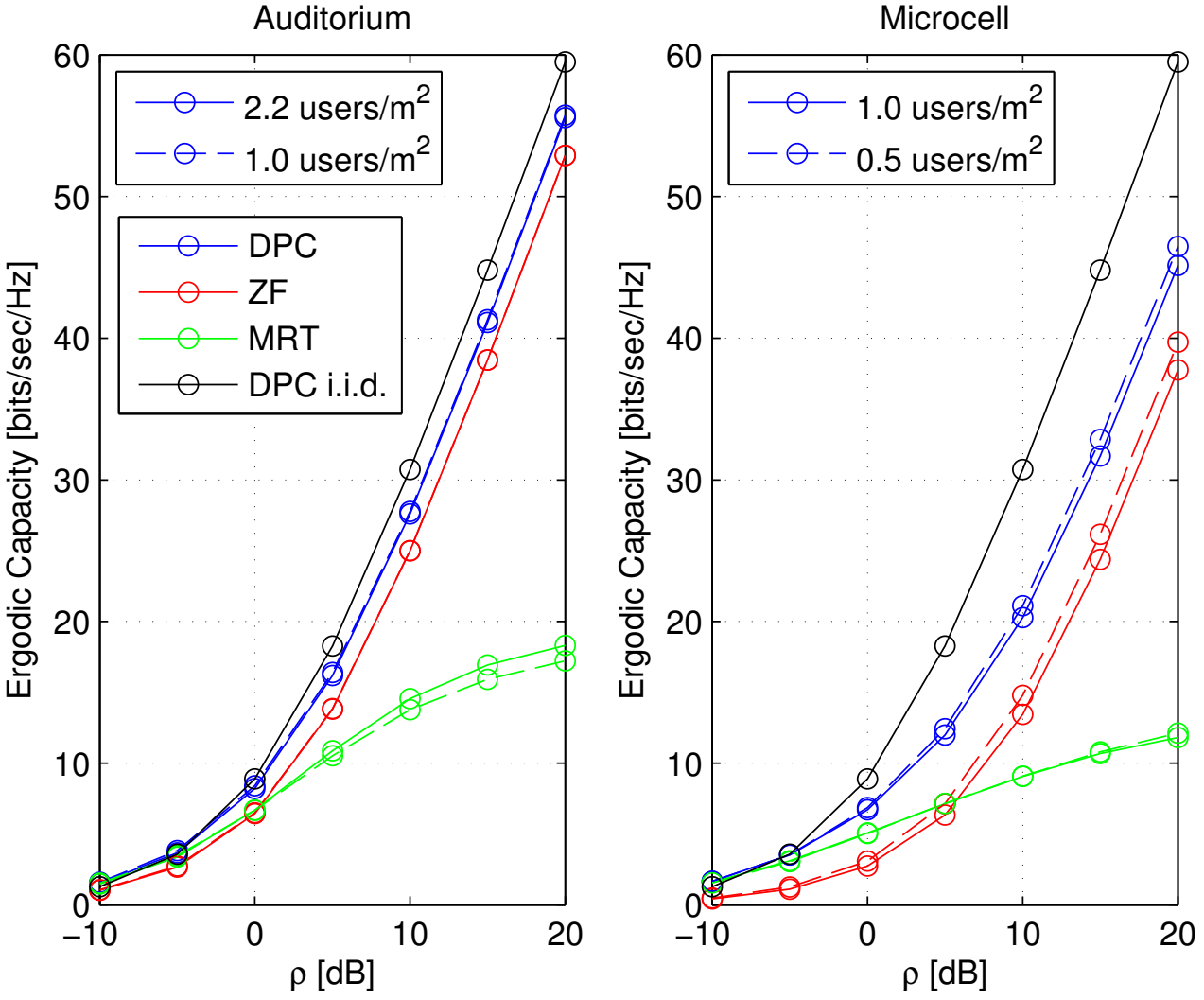

Figure 6.8: Sum-rate capacity and sum-rates with zero forcing (ZF) and maximum ratio transmission (MRT) for several user densities and two deployments: indoor auditorium (left) and outdoor suburban microcell (right). For comparison purposes, the sum-rate capacity of an i.i.d. Rayleigh channel with the same number of users and antennas is also given.

6.3 Directional analysis

In Sec. 6.1 and Sec. 6.2 we have looked at the characteristics and performance of measured massive MIMO channels including the effects of the BS antenna array and UE antennas used during the measurements. This type of channel, comprising the antenna patterns, is referred to as the *radio* channel[2]. For the purpose of channel modeling, however, one wishes to remove the effect of the measurement antennas so that the resulting model depends only on the electromagnetic propagation mechanisms acting between the location of the BS and the location of the users. The latter channel is referred to as the *propagation* channel, and can be obtained from the measured radio channel through the process of *directional analysis*. To do so, we assume that the propagation channel from transmit location $\mathbf{r}_{\mathrm{Tx}}$ to receive location $\mathbf{r}_{\mathrm{Rx}}$, denoted as $h(\tau, \Omega, \Psi; \mathbf{r}_{\mathrm{Tx}}, \mathbf{r}_{\mathrm{Rx}})$, can be described as the sum of a N plane waves impinging on the receiver. This is,

$$h(\tau, \Omega, \Psi; \mathbf{r}_{\mathrm{Tx}}, \mathbf{r}_{\mathrm{Rx}}) = \sum_{n=1}^{N} \mathbf{\Gamma}_n \delta(\tau - \tau_n)\delta(\Omega - \Omega_n)\delta(\Psi - \Psi_n), \tag{6.9}$$

where τ, Ω, Ψ are the delay, angle-of-arrival and angle-of-departure domains, respectively, and τ_n,Ω_n,Ψ_n are the delay, direction of arrival and direction of departure of the nth impinging wave, respectively. The directional domain at each link end can be further decomposed into azimuth and elevation components, i.e. $\Omega = (\phi, \theta)$ and $\Psi = (\varphi, \vartheta)$. Moreover, $\mathbf{\Gamma}_n$ is a 2×2 complex matrix which has the form

$$\mathbf{\Gamma}_n = \begin{pmatrix} \gamma_{n,\mathrm{HH}} & \gamma_{n,\mathrm{HV}} \\ \gamma_{n,\mathrm{VH}} & \gamma_{n,\mathrm{VV}} \end{pmatrix}, \tag{6.10}$$

and describes the polarimetric amplitudes of the propagation channel between Tx and Rx for the nth impinging wave.

The process of directional analysis consists in estimating the set of parameters defining the propagation channel, i.e. $\{\mathbf{\Gamma}_1, \tau_1, \Omega_1, \Psi_1, \ldots, \Psi_N\}$, from the observations of the radio channel, $\mathbf{H}(t, f) \in \mathbb{C}^{N_{\mathrm{Rx}} \times N_{\mathrm{Tx}}}$, with $t = 1, \ldots, T$ and $f = 1, \ldots, L$, where N_{Rx}, N_{Tx}, L and T are the number of receive antenna array ports, the number of transmit antenna array ports, the number of frequency points and the number of snapshots, respectively.

Note that, in the setup considered, we cannot estimate the angle of departure. This is so since all users are single antenna users. Hence, in our case, $N_{\mathrm{Rx}} = M$, $N_{\mathrm{Tx}} = 1$ and model (6.9) reduces to

$$h(\tau, \phi, \theta; \mathbf{r}_{\mathrm{Tx}}, \mathbf{r}_{\mathrm{Rx}}) = \sum_{n=1}^{N} \mathbf{\Gamma}_n \delta(\tau - \tau_n)\delta(\phi - \phi_n)\delta(\theta - \theta_n), \tag{6.11}$$

where only the delay and direction of arrival domains are considered. For the same reason, it is not possible to estimate the full-polarimetric matrix of channel amplitudes, $\mathbf{\Gamma}_n$. Instead, with the UE antenna configuration used for the measurement campaigns and assuming a perfect antenna tilt of 45 degrees, one can only estimate a reduced polarization matrix $\mathbf{\Gamma}'_n$ of the form

$$\mathbf{\Gamma}'_n = \begin{pmatrix} \gamma'_{n,\mathrm{H}} \\ \gamma'_{n,\mathrm{V}} \end{pmatrix}, \tag{6.12}$$

where $\gamma'_{n,\mathrm{H}}$ accounts for the energy transferred through $\gamma_{n,\mathrm{HH}}$ and $\gamma_{n,\mathrm{HV}}$ and, in a similar way, $\gamma'_{n,\mathrm{V}}$ accounts for $\gamma_{n,\mathrm{VH}}$ and $\gamma_{n,\mathrm{VV}}$.

[2]At the user side, the antenna pattern measured for an isolated antenna, e.g. in an anechoic chamber, has to be modified to account for the effect of the user grip. The resulting antenna pattern is often referred to as the *super* antenna pattern.

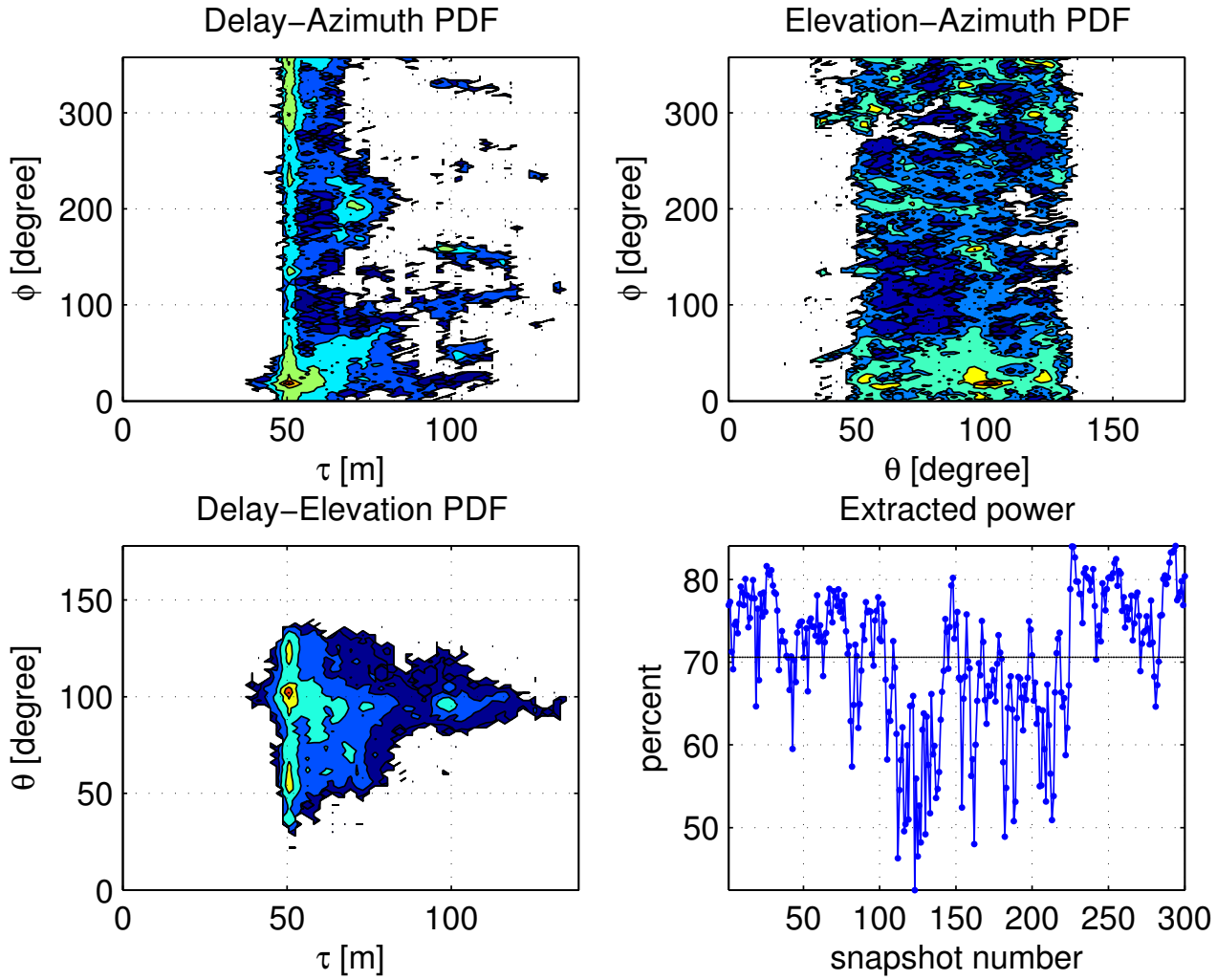

Figure 6.9: Two-dimensional PDFs of the propagation channel from user 1 to BS in an outdoor suburban microcell deployment (site MS 2, with user surrounded by a crowd). The PDFs are based on the estimated gains, directions and delays of 30 000 plane waves. The dynamic range if -110 dB to -60 dB. The amount of transferred energy that can be modeled as deterministic plane waves is also shown (bottom, right).

Several algorithms exist for performing directional analysis. In this work, the SAGE algorithm described in [6] has been used. Directional estimation is performed independently for each of the $K = 9$ users and each of the $T = 300$ snapshots. The number of antenna ports at the BS antenna array is $M = 128$ and the number of frequency points measured is $L = 129$ for indoor scenarios and $L = 257$ for outdoor scenarios. The model order has been selected as $N = 100$.

Fig. 6.9 and Fig. 6.10 show the two-dimensional probability density functions (PDFs) of the propagation channel between user 1 and the BS for an outdoor suburban microcell deployment (site MS 2) and an indoor auditorium deployment (BS 1, users at the back), respectively. The PDFs are based on the estimated gains, directions and delays of 30 000 plane waves using the SAGE algorithm (300 snapshots times 100 plane waves per snapshot).

The second order spatial statistics of the propagation channel of users located close to each other, i.e. the power-angular profiles (see Fig. 6.9 and Fig. 6.10), overlap to a great extent.

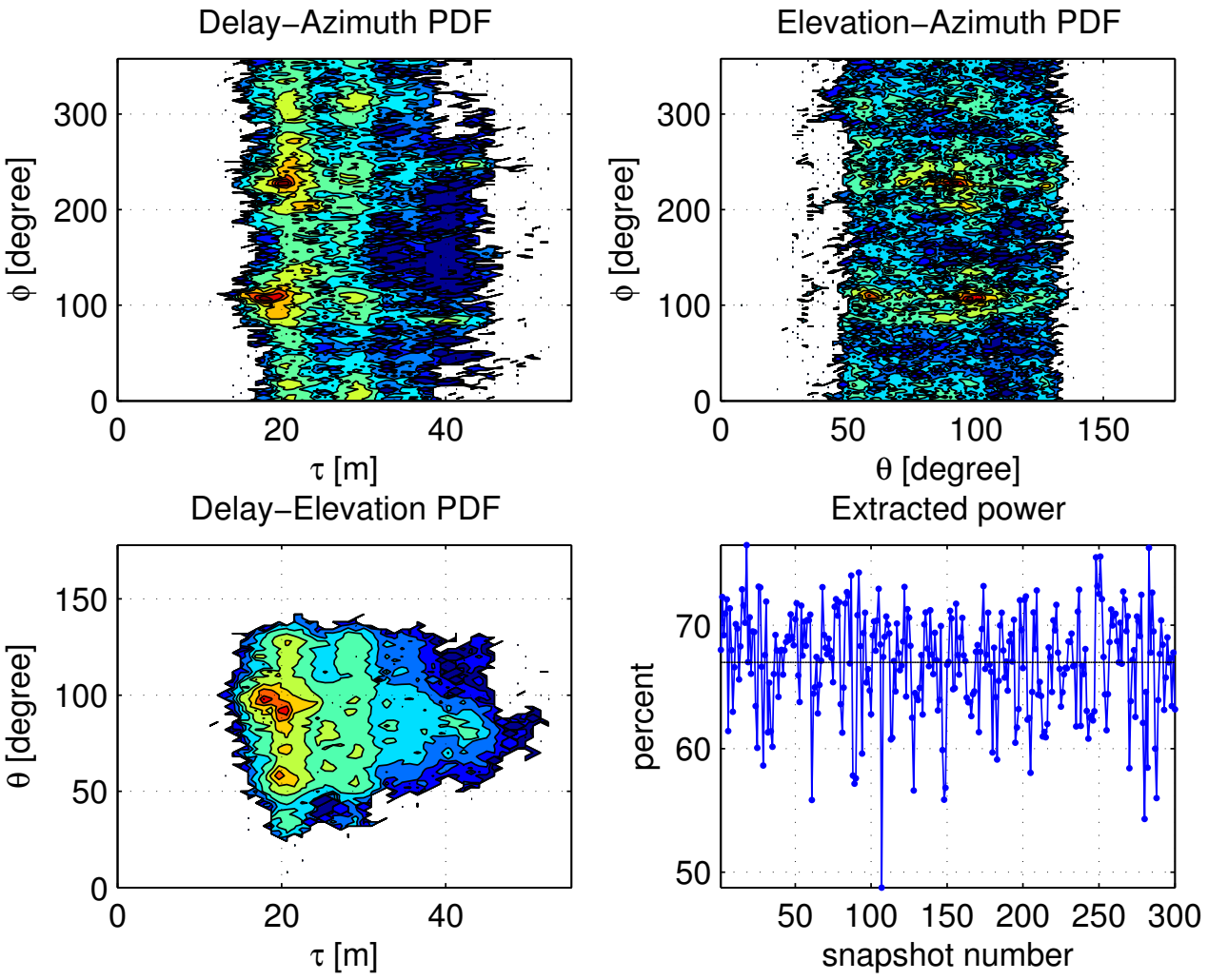

Figure 6.10: Two-dimensional PDFs of the propagation channel from user 1 to BS in an indoor auditorium deployment (BS 1, users at the back surrounded by a crowd). The PDFs are based on the estimated gains, directions and delays of 30 000 plane waves. The dynamic range is -80 dB to -30 dB. The amount of transferred energy that can be modeled as deterministic plane waves is also shown (bottom, right).

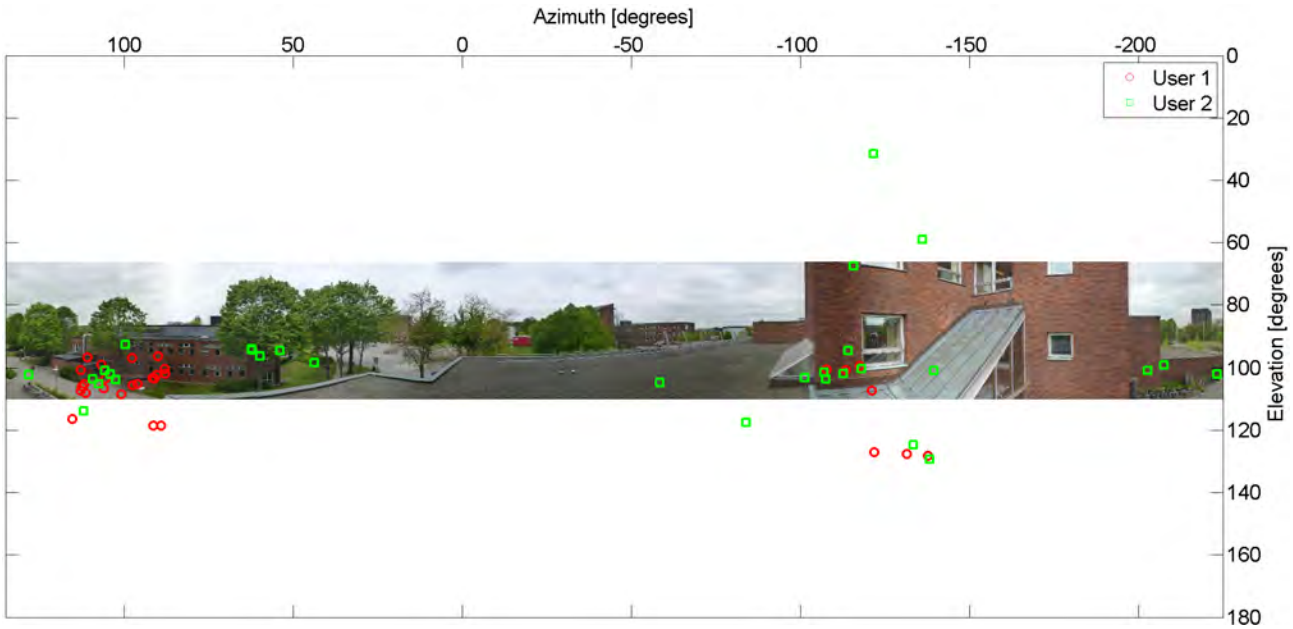

Figure 6.11: LOS component and the 30 strongest multipath components for users 1 and 2, at snapshot 100. This figure corresponds to an outdoor suburban microcell deployment (site MS 1). There is LOS to the BS and a crowd is present.

Hence, if we seek to understand why users in massive MIMO systems, although located close to each other, can still be spatially separated, we need to look at instantaneous realizations of the propagation channel. Fig. 6.11 and Fig. 6.12 show the estimated LOS and the 30 strongest MPCs for the outdoor deployments at sites MS 1 and MS 2. As noticed earlier, these two sites have LOS to the BS. Fig. 6.13 and Fig. 6.14 show the corresponding plots for the NLOS outdoor sites MS 8 and MS 10. In these examples, a crowd of people was present during the measurements. We see that MPCs tend to arrive in groups, or *clusters*, each cluster having a distinct delay-direction of arrival and a limited spread (note that delays are not shown in the figures). Clusters arise from the interaction of the propagating electromagnetic waves with discrete physical objects (*scatterers*) acting as reflecting surfaces. Naturally, we expect two users located close to each other to share some common scatterers. An important observation is that different users "see" the same scatterers in different ways. This point is illustrated in Fig. 6.11 through Fig. 6.14, for outdoor environments. We observe that clusters seen by different users (in different color) but originating from a common scatterer, although clearly overlapping in the same azimuth-elevation region, possess distinct MPCs. Based on this observation, one can expect that differences in the MPCs observed by users will translate into the ability to spatially separate those users. This point, however, needs further verification.

Fig. 6.11, 6.16, 6.17 and 6.18 further illustrate this principle for several measured indoor deployments. It is worth noting that users 1 and 2 in Fig. 6.11, 6.16, 6.17 and 6.18 sit next to each other (see Fig. 5.2, left side.)

6.4 Temporal behavior

In this section we will look into the temporal behavior of the measured radio channels. Fig. 6.19 shows the CDF of the 3-dB coherence time and 3-dB coherence bandwidth of the measured SISO channels (9 times 128 of them). Plots are shown for two different deployments, namely,

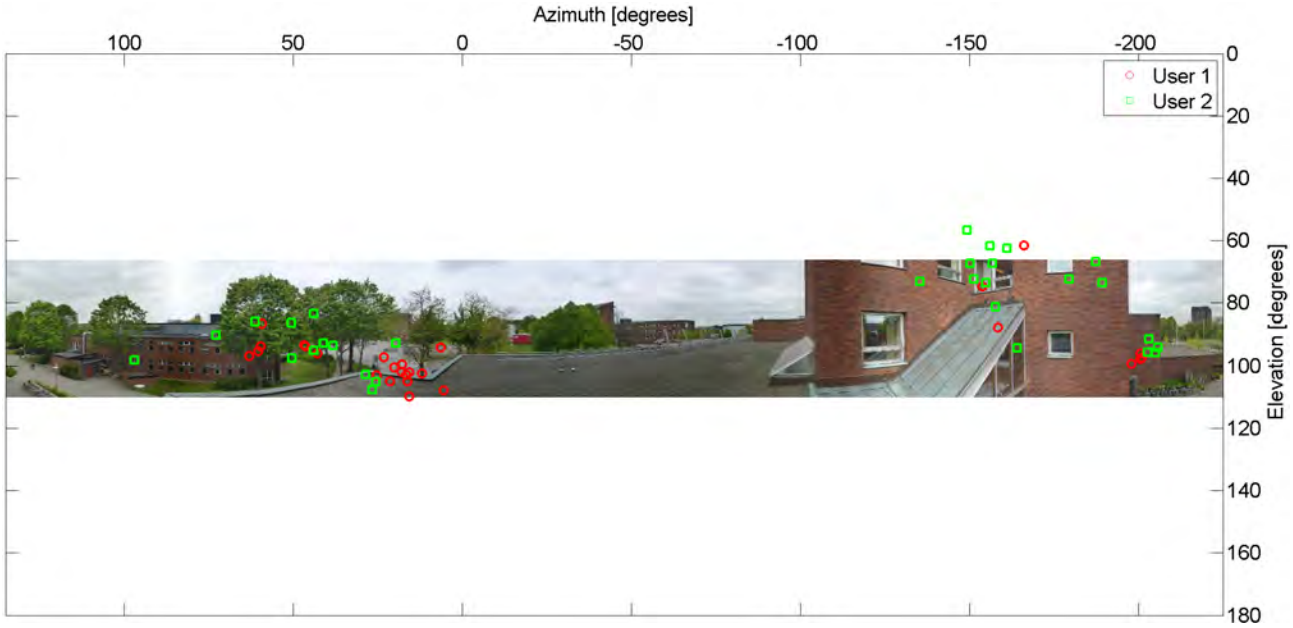

Figure 6.12: LOS component and the 30 strongest multipath components for users 1 and 2, at snapshot 100. This figure corresponds to an outdoor suburban microcell deployment (site MS 2). There is LOS to the BS and a crowd is present.

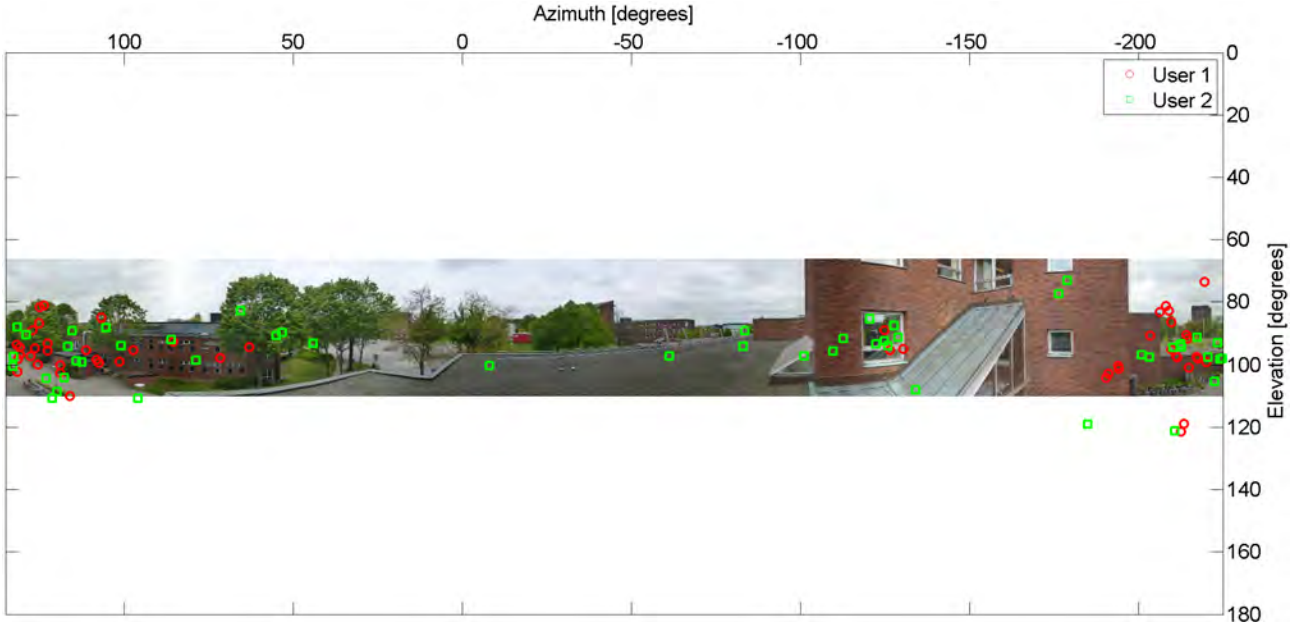

Figure 6.13: LOS component and the 50 strongest multipath components for users 1 and 2, at snapshot 100. This figure corresponds to an outdoor suburban microcell deployment (site MS 8). There is NLOS to the BS and a crowd is present.

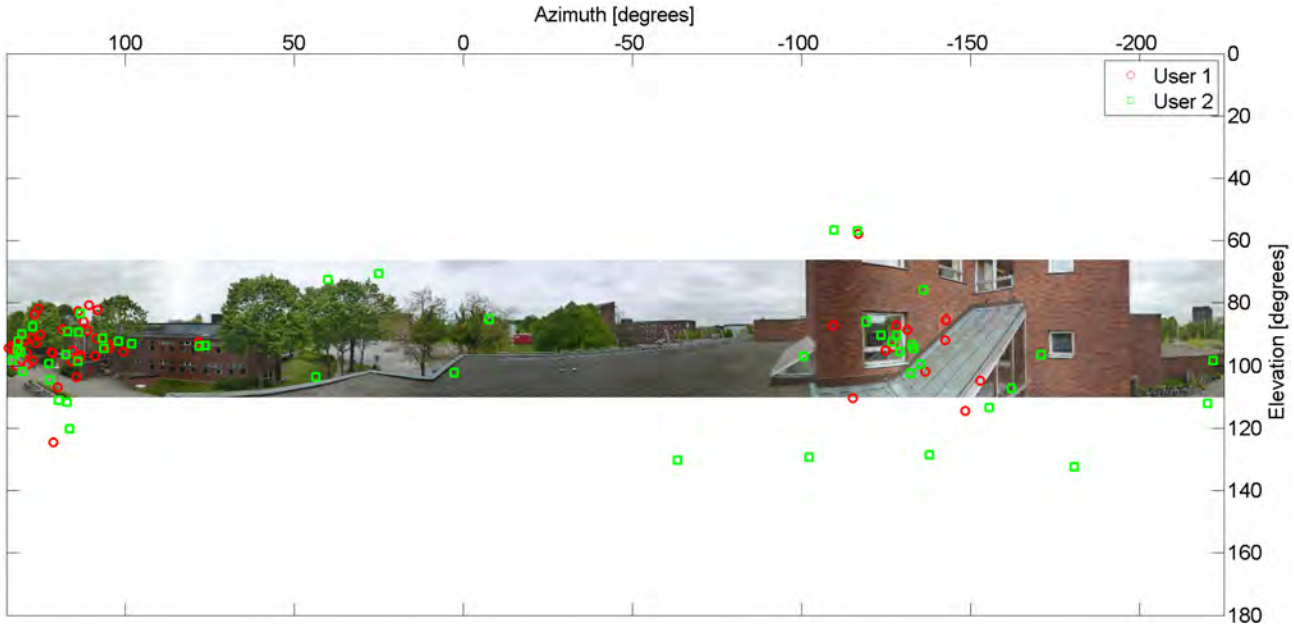

Figure 6.14: LOS component and the 50 strongest multipath components for users 1 and 2, at snapshot 100. This figure corresponds to an outdoor suburban microcell deployment (site MS 10). There is NLOS to the BS and a crowd is present.

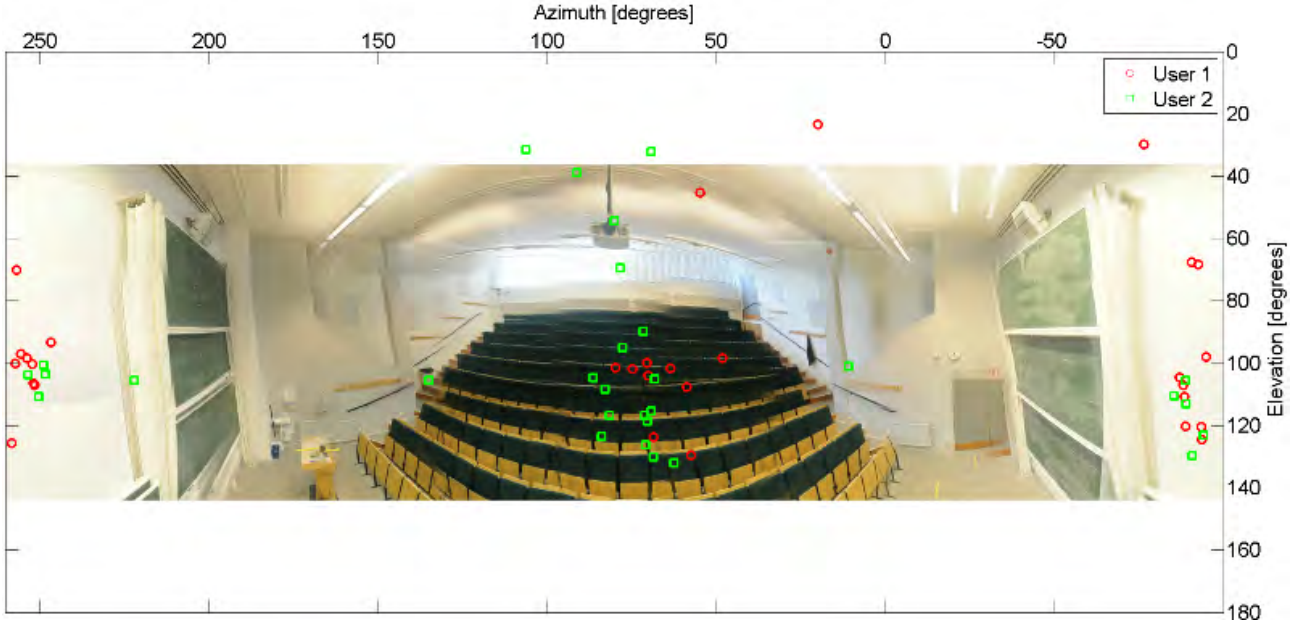

Figure 6.15: LOS component and the 30 strongest multipath components for users 1 and 2, at snapshot 10. This figure corresponds to an indoor auditorium deployment (BS 1, users at the center). There is LOS and no crowd is present.

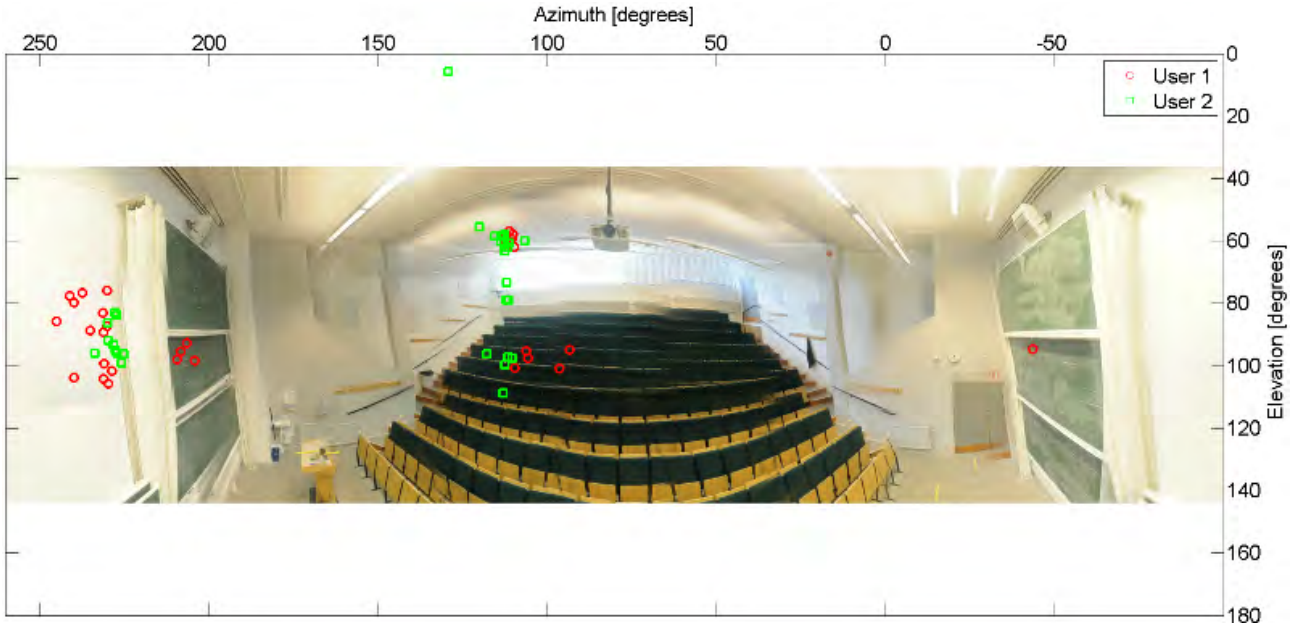

Figure 6.16: LOS component and the 30 strongest multipath components for users 1 and 2, at snapshot 10. This figure corresponds to an indoor auditorium deployment (BS 1, users at the back). There is LOS and no crowd is present.

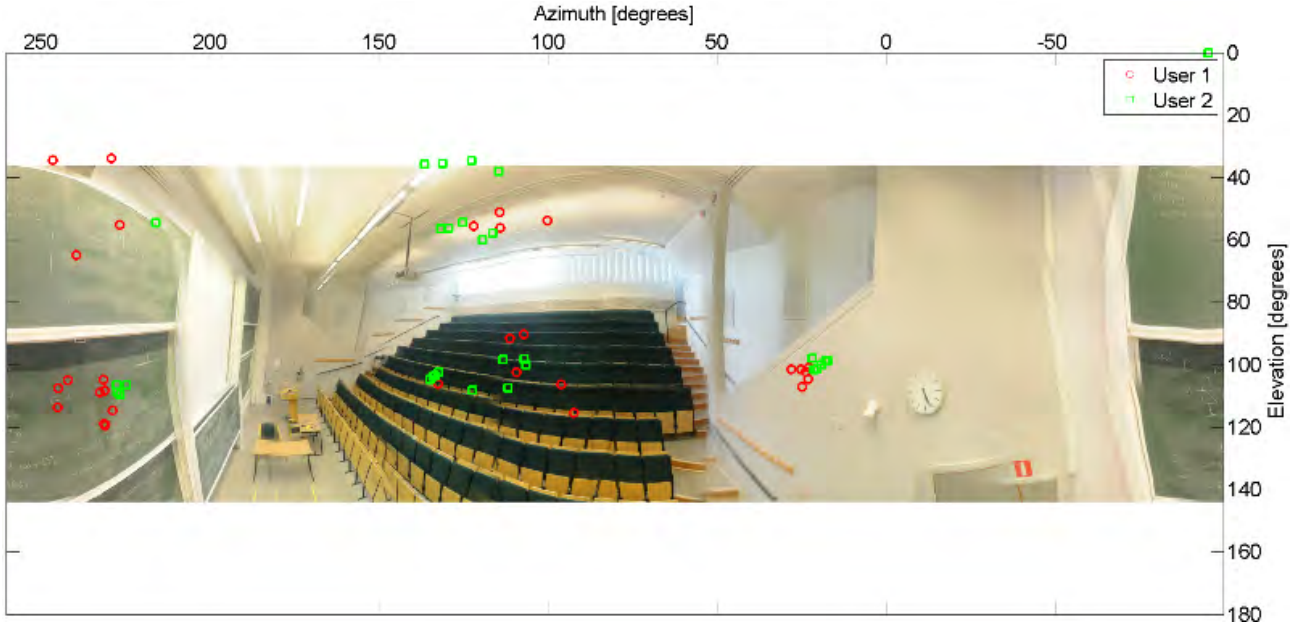

Figure 6.17: LOS component and the 30 strongest multipath components for users 1 and 2, at snapshot 10. This figure corresponds to an indoor auditorium deployment (BS 3, users at the center). There is LOS and no crowd is present.

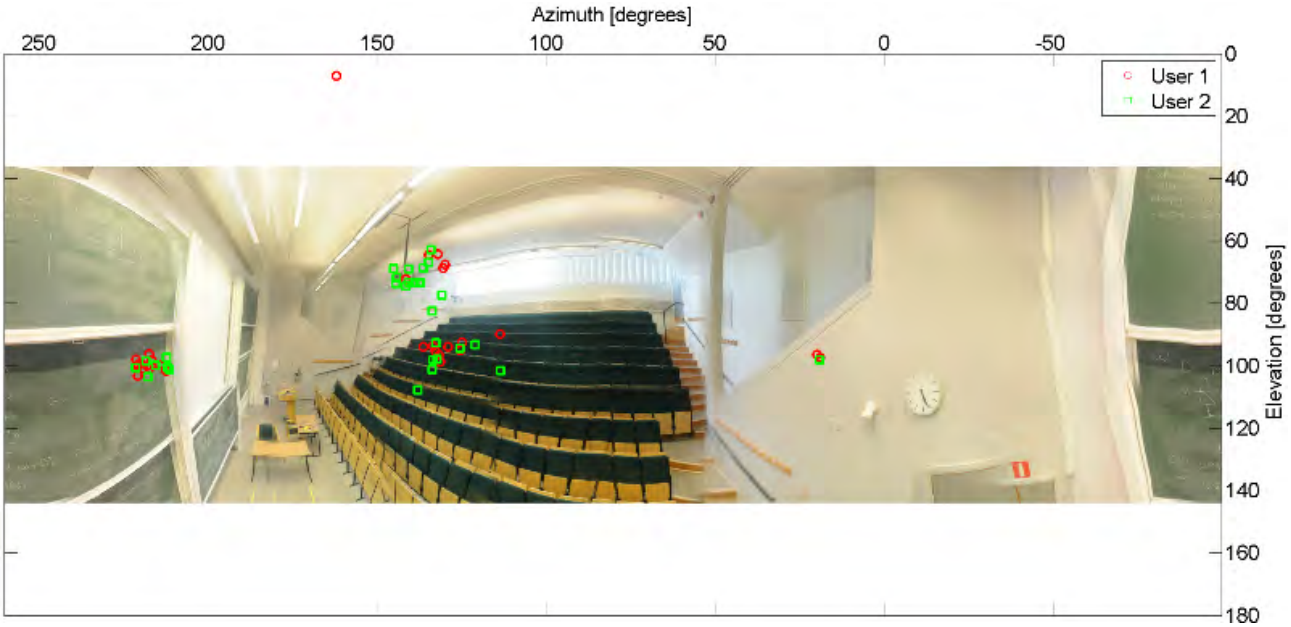

Figure 6.18: LOS component and the 30 strongest multipath components for users 1 and 2, at snapshot 10. This figure corresponds to an indoor auditorium deployment (BS 3, users at the back). There is LOS and no crowd is present.

indoor auditorium (BS 1, users at the back) and outdoor suburban microcell (site MS 2), and for two different user densities. The mean values of the 3-dB coherence time and bandwidth are summarized in Tab. 6.3 and Tab. 6.4, respectively. These figures suggest that channels, of those we have measured, decorrelate faster in the indoor case, implying that, for the same user mobility, channel state information needs to be acquired faster in this case. In reality, however, the expected user mobility is probably higher in outdoor scenarios. On the other hand, the mean coherence bandwidth is smaller for outdoor channels. This can be understood noting that the channel delay spread is likely larger in outdoor scenarios.

Environment	**Crowd**	**No-Crowd**
Outdoor suburban microcell	80.1	75.9
Indoor auditorium	32.0	42.7

Table 6.3: Expected coherence time at 3-dB, in [ms].

Environment	**Crowd**	**No-Crowd**
Outdoor suburban microcell	8.6	8.2
Indoor auditorium	11.0	10.9

Table 6.4: Expected coherence bandwidth at 3-dB, in [MHz].

Of particular importance to the performace of MU-MIMO systems is the correlation between user channels. We define the correlation coefficient c_{ij} between users i and j as

$$c_{ij} = \frac{\mathbf{h}_i^{\mathrm{H}} \mathbf{h}_j}{\|\mathbf{h}_i\| \|\mathbf{h}_j\|}, \quad \text{with } 1 \leq i < j \leq K, \tag{6.13}$$

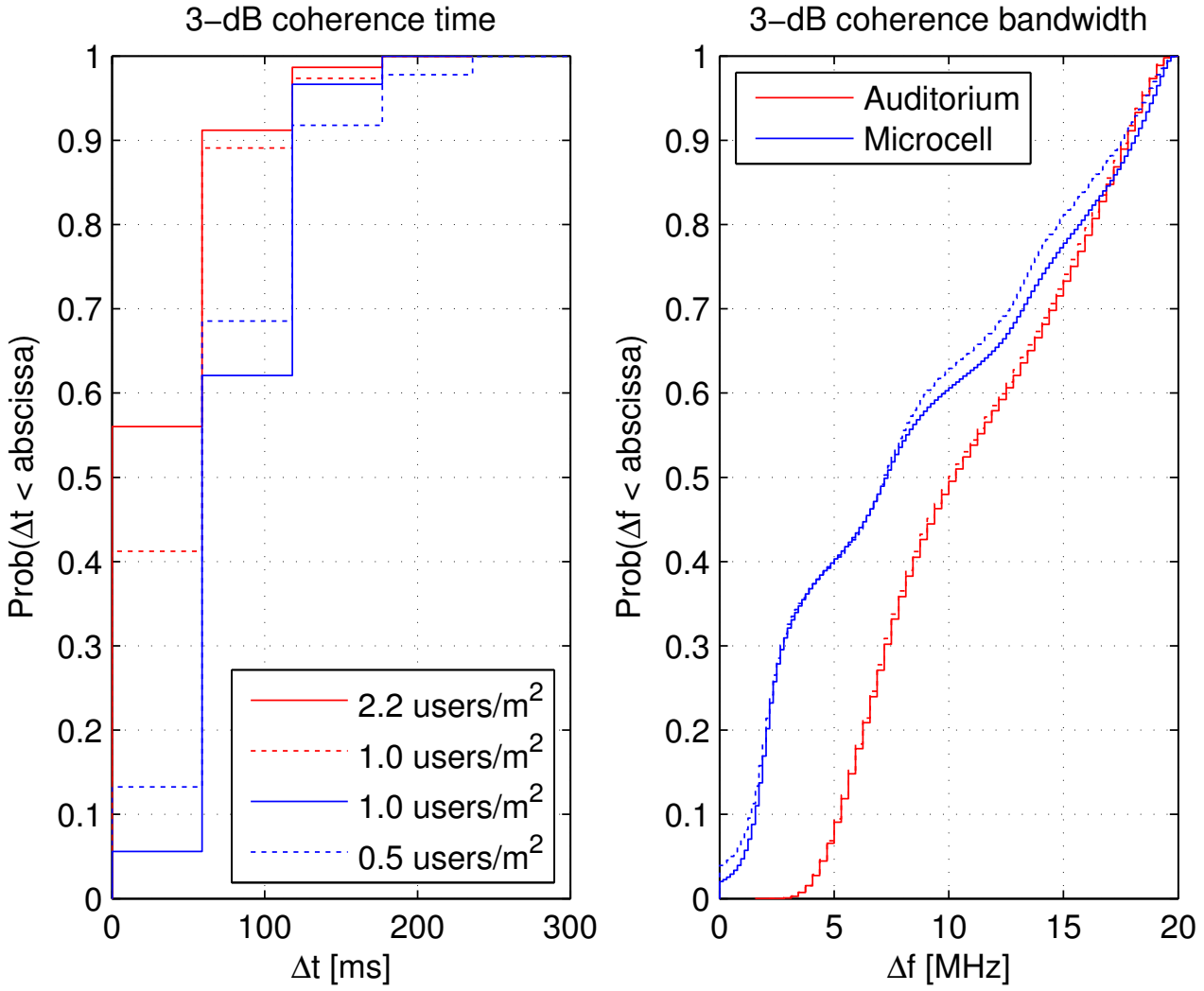

Figure 6.19: Cumulative distribution function (CDF) of the 3-dB coherence time (left) and 3-dB coherence bandwidth (right) of the measured 9×128 SISO channels. The CDF is shown for two different deployments, namely, indoor auditorium (BS 1, users at the back) and outdoor suburban microcell (site MS 2), and for two different user densities. Recall that the snapshot sampling rate is ca. 60 ms (Tab. 4.1); hence, the coarse temporal resolution of the time coherence CDF (left).

where vectors $\mathbf{h}_k \in \mathbb{C}^{1\times M}$, with $k = 1, \ldots, K$, stand for the MISO channel from the BS to the kth user, $(.)^{\mathrm{H}}$ denotes the Hermitian operator, and $\|\mathbf{a}\|$ is the Euclidian length of vector $\mathbf{a}$. The correlation coefficients c_{ij} are, in general, time-dependent and form a time series $\{c_{ij}(t)\}$ for $t = 1, \ldots$. Fig. 6.21 and Fig. 6.20 show plots of the real part of the time-series $\{c_{1,2}(t)\}$ and $\{c_{1,3}(t)\}$ for the indoor and outdoor deployments introduced earlier in this section. The index t takes values $t = 1, \ldots, 300$ and denotes the snapshot number. The dependency with the frequency of $c_{1,2}(1)$ and $c_{1,3}(1)$ is also shown, as well as the probability density function (PDF) of $c_{ij}(t, f)$ computed over the data points $1 \leq i < j \leq 9$, $t = 1, \ldots, 300$ and $f = 1, \ldots, 129$, for the indoor case, and $f = 1, \ldots, 257$, for the outdoor case. (Plots of the imaginary part of c_{ij} are very similar and, therefore, not shown.) We observe that the correlation coefficients of the measured indoor channels vary faster that those of measured outdoor channels, which is in good agreement with Fig. 6.19. It should be mentioned that, due to the fact that in our measurement campaigns, users have been asked to make artificial movements (walking and turning around in the outdoor campaign, and waving the antenna in order to experience different orientations, and positions relative to the user's body in the indoor campaign), the aforementioned conclusion can't be generalized to all outdoor and indoor channels. Variations of the correlation coefficients over the frequency band are much slower, for both indoor and outdoor measured channels. The PDF plots show that user channel correlation can be significant, specially for measured outdoor channels. For example, the probability that $|c_{ij}| > 0.50$ is 50% for measured outdoor channels and 2% for measured indoor channels. As a result, we can expect that indoor users will be easier to separate than outdoor ones.

We look also into the temporal behaviour of the small-scale gain of the user channels, which we denote as g_k. In this example, the small-scale gain of the kth user has been computed as

$$g_k(t, f) = \frac{\|\mathbf{h}_k(t, f)\|^2}{\sum_{f=1}^{129\,(257)} \|\mathbf{h}_k(t, f)\|^2}. \tag{6.14}$$

With this definition, the effects the path loss and large-scale fading are removed, while power variations due to small-scale fading and to the directional properties of the elements of the BS antenna array are retained. Plots of $g_k(t, 1)$ and $g_k(1, f)$ for two users, as well as a plot of the PDF of $g_k(t, f)$, are shown in Fig. 6.22.

6.5 Multipath component clustering

6.5.1 Approach

By using SAGE algorithm, we obtain the estimation of the specular multipath components in the radio channels. With cluster-based channel modeling approach, we group these multipath components into clusters. Multipath components that have similar delays, angles in azimuth and angles in elevation are grouped into the same cluster. We approach the clustering in the following way. First, all the multipath components available, i.e., from all users and snapshots, are merged together as one data set, then we apply KpowerMeans clustering algorithm [4, 5] to this data set. In this step, temporal variations are disregarded, as well as variations across users. This is reasonable if we recall that, in the measurement setup, users move within a limited area and interact with the same scattering environment. Therefore, one can expect that the users behave in an equivalent way over snapshots. Furthermore, due to the limited dimensions of the area in which users move, user behavioral patterns will repeat over time. From a modeling

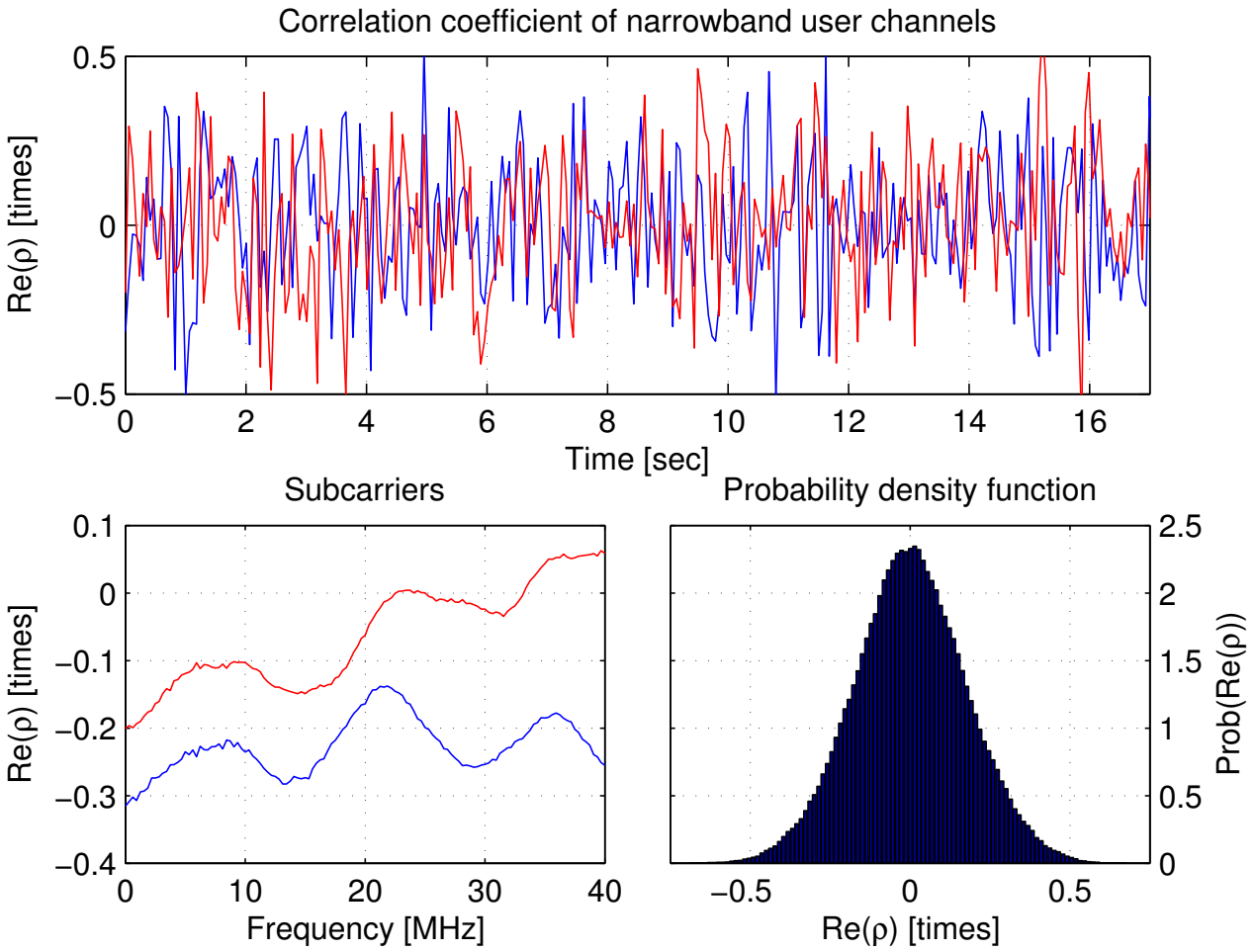

Figure 6.20: For an indoor auditorium deployment (BS 1, users at the back in the presence of a crowd) the plots show: time series of the real part of the correlation coefficients $c_{1,2}$ and $c_{1,3}$ (top); frequency dependency of the real part of the correlation coefficients $c_{1,2}$ and $c_{1,3}$ (bottom left); and, probability density function (PDF) of the real part of the correlation coefficients over all user pairs, snapshots and subcarriers.

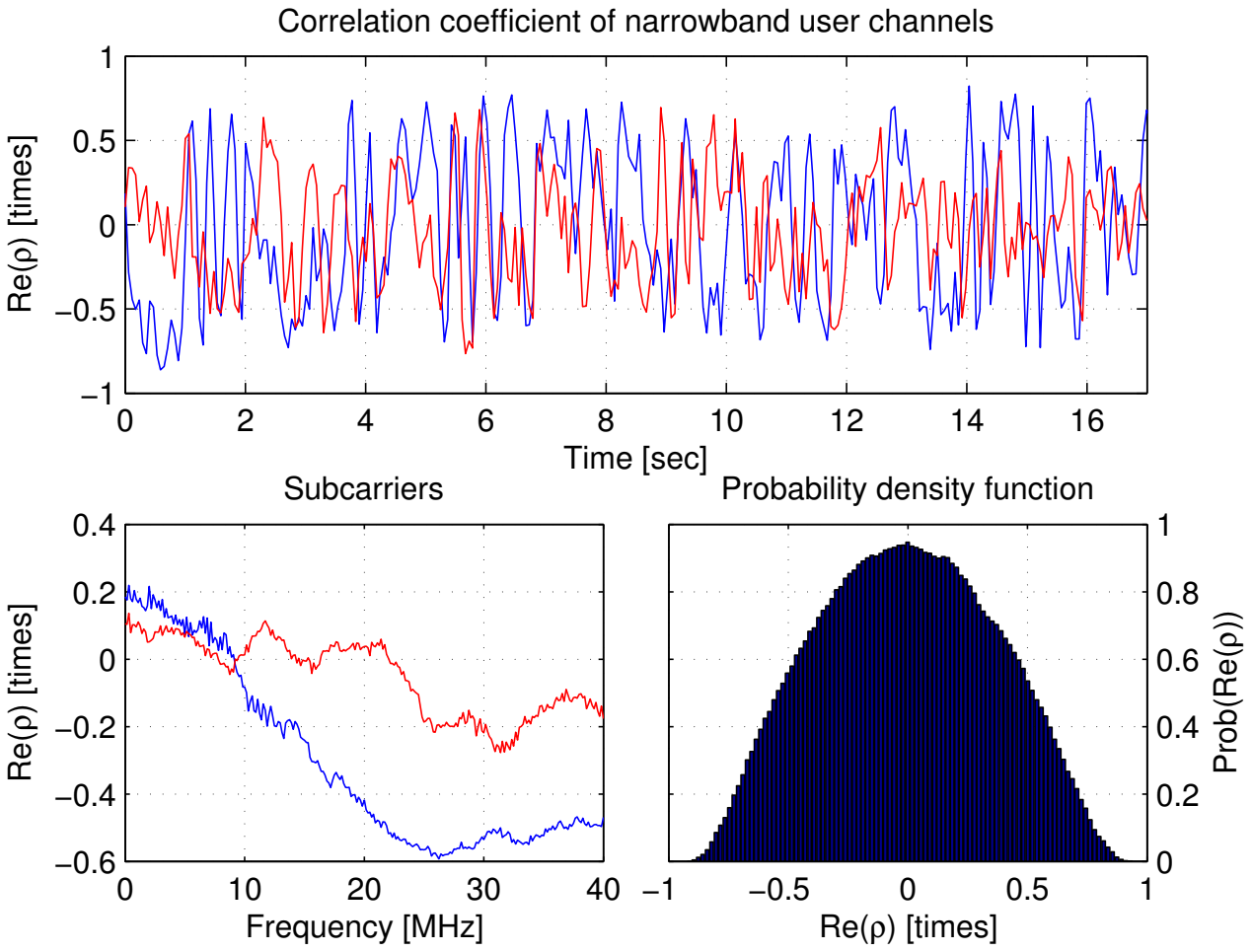

Figure 6.21: For an outdoor suburban microcell deployment (site MS 2, in the presence of a crowd) the plots show: time series of the real part of the correlation coefficients $c_{1,2}$ and $c_{1,3}$ (top); frequency dependency of the real part of the correlation coefficients $c_{1,2}$ and $c_{1,3}$ (bottom left); and, probability density function (PDF) of the real part of the correlation coefficients over all user pairs, snapshots and subcarriers.

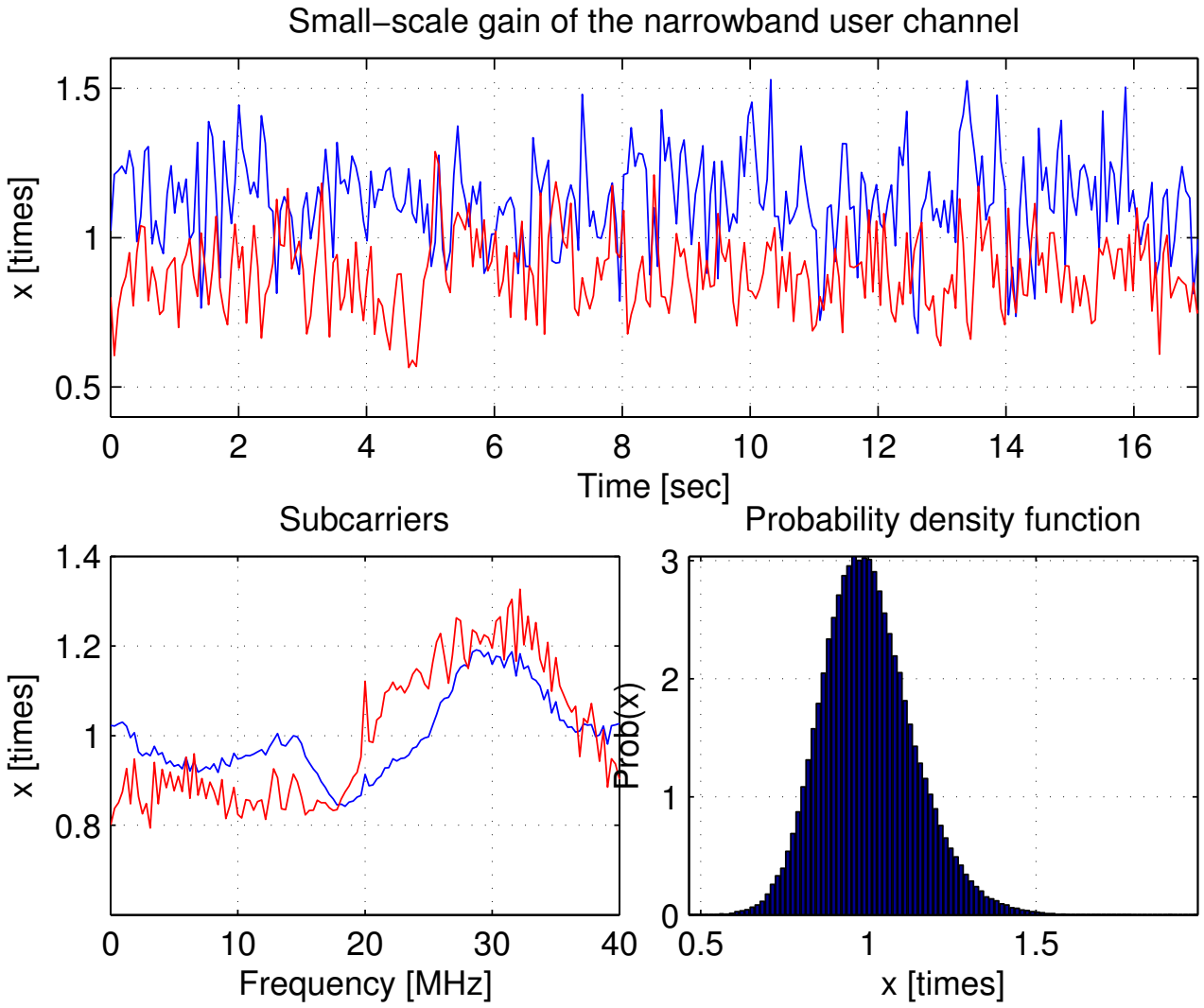

Figure 6.22: For an indoor auditorium environment (BS 1, users at the back in the presence of a crowd) the plots show: time series of the small-scale gain of the narrowband channel for users 1 and 2 (top); frequency dependency of the small-scale gain of the narrowband channel of users 1 and 2 (bottom left); and, probability density function (PDF) of the small-scale gain of the narrowband channels over all users, snapshots and subcarriers.

point of view, it is plausible to assume that all clusters are seen by all users, i.e., all users are within the same cluster visibility regions. However, clusters are not seen by the users all the time. This is due to the change of the user directions as well as the shadowing caused by the crowd. It is clear that, in the first step of our clustering approach, the number of clusters, their positions and spreads are extracted. In the second step, we look at the temporal behavior of each cluster on a per-user basis.

This approach that clusters the multipath components from all users and all snapshots works for outdoor environment, however, this may not work for the indoor environment due to short distances of scatterers, and spacing between users may make a difference on the clustering results. Therefore, for indoor measurement, we cluster the multipath components from all snapshots but on per-user basis.

To determine the appropriate number of clusters in each scenario, we also refer to the WINNER II channel models [11]. There, for indoor office (A1) scenario, the cluster number is 12-16 (for LOS and NLOS); for indoor hotspot (B3) scenario which defines large indoor hall, the number is 10-15; for urban micro-cell (B1), the number is 8-16; for urban macro-cell (C2), the number is 8-20. Hence, we select the cluster number in our measurements and modeling to be around 10-16 for indoor scenarios, and 8-16 for outdoor scenarios (urban micro). In the clustering algorithm, we set the maximum number of clusters to be 16 for both indoor and outdoor scenarios. To form a cluster, the power of a group of MPCs must have at least 0.05% of the total power. The output of the clustering algorithm gives us a small variation in the cluster number in different scenarios.

Clustering for indoor measurements is performed based on the multipath components that have channel gain above -70 dB in power, while for outdoor measurements, it is done based on all multipath components. Next, we report our clustering results.

6.5.2 Results and discussion

Outdoor scenarios

For the outdoor measurements, we show one LOS scenario and one NLOS scenario as examples. Fig. 6.23-Fig. 6.27 show the clustering results for Site 1 with crowd. Through the satellite map and panorama picture with multipath components and clusters plotted on top, we can see how multipath components are grouped based on parameters such as delay, azimuth angle and elevation angle. Furthermore, we can also see how the multipath components and clusters match with the scatterers in the environment.

Fig. 6.28-Fig. 6.32 show the clustering results for measurement at Site 10 with crowd. This is an NLOS scenario. From these figure, we again see how multipath components are grouped into clusters that are separated by delay, azimuth angle and elevation angle.

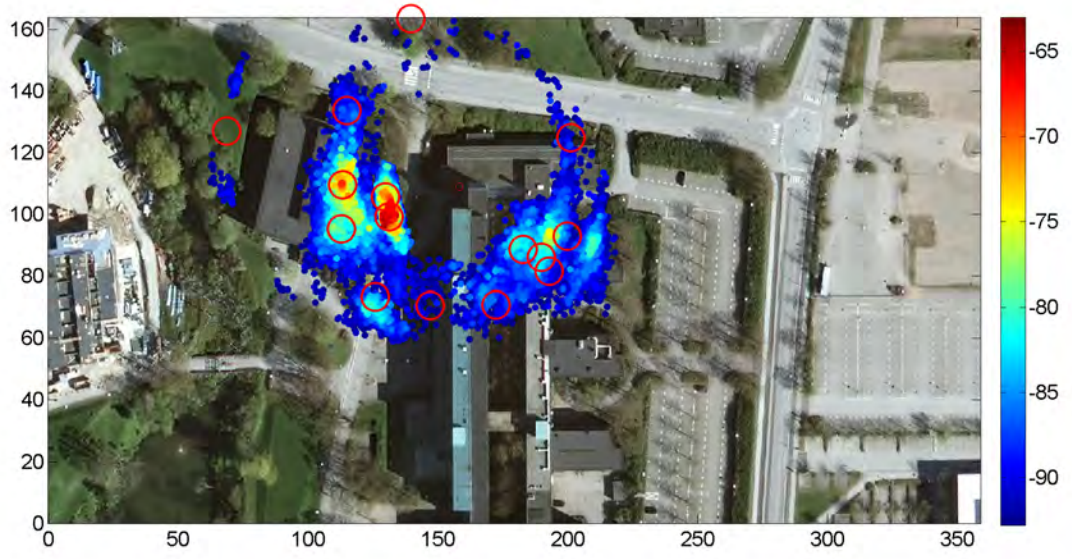

Figure 6.23: MPC strengths from all 9 users in all 300 snapshots, Site 1, with crowd. Color coding represents the channel gain of the MPCs in dB. The distance of each MPC point to the base station is the delay of the corresponding MPC. The circles indicate the positions of cluster centroids. Here we see that the clusters with different delays and azimuth angles are captured.

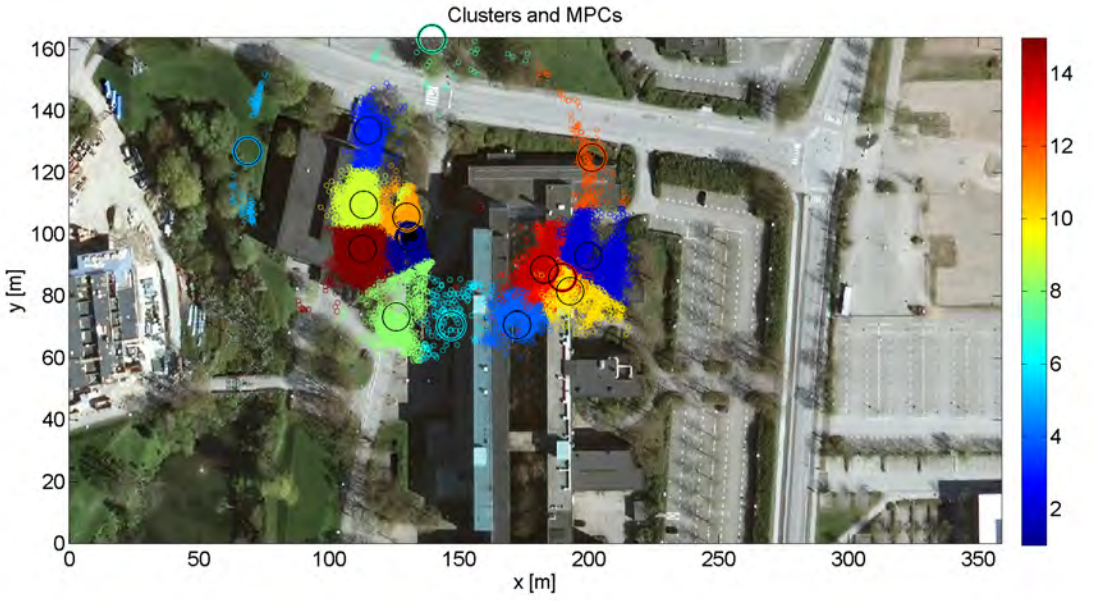

Figure 6.24: Clusters based on MPCs from all 9 users in all 300 snapshots, Site 1, with crowd. There are 15 clusters. Color coding represents different clusters.

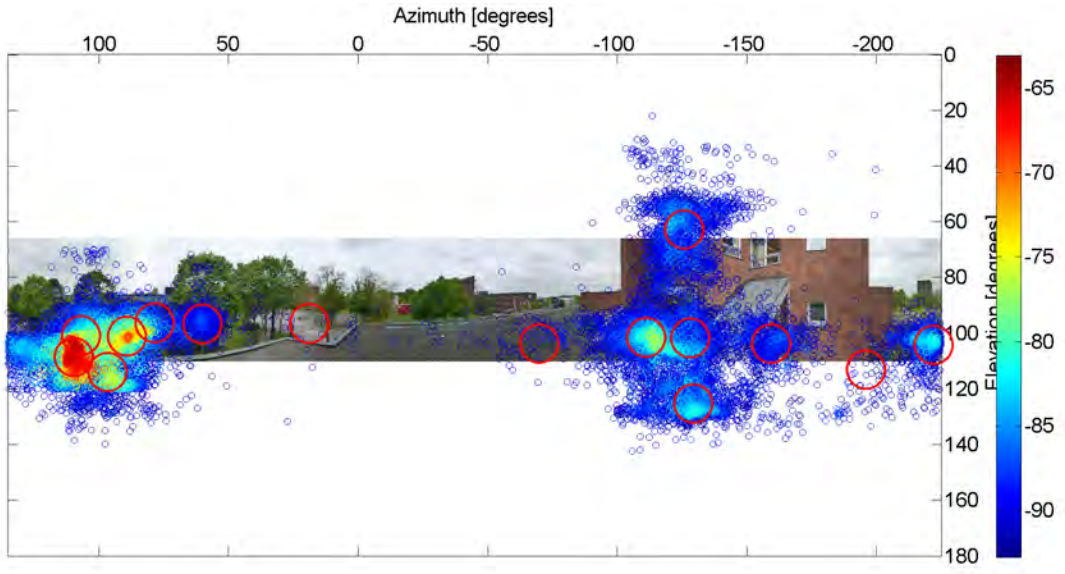

Figure 6.25: MPC strengths from all 9 users in all 300 snapshots, Site 1, with crowd. Color coding represents the channel gain of the MPCs in dB. The strongest energy contribution comes from around 100 degrees azimuth angle, which is the direction of LOS. There are also strong signals due to scattering at the buildings around.

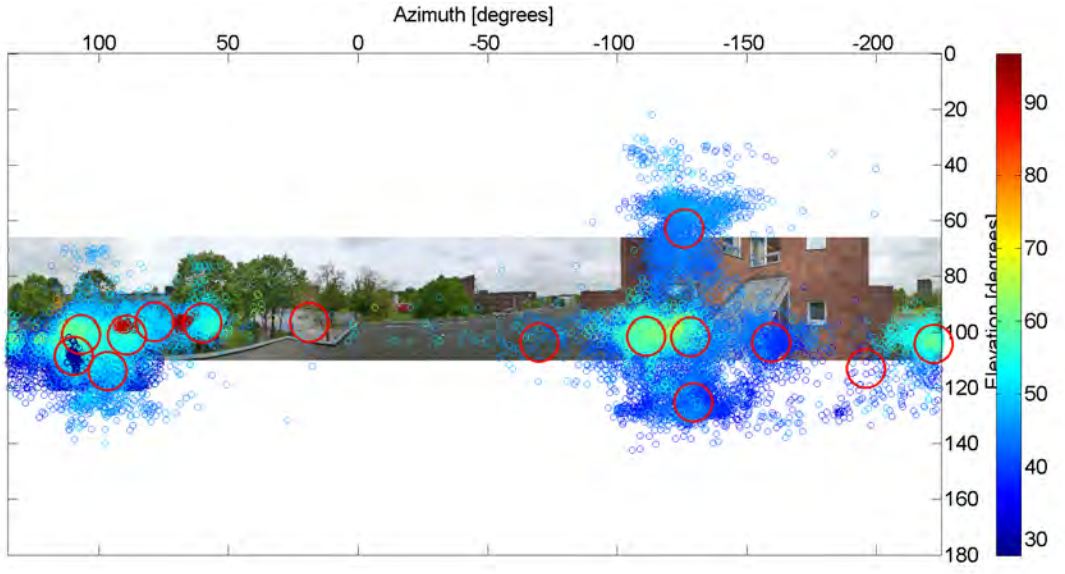

Figure 6.26: MPC delays from all 9 users in all 300 snapshots, Site 1, with crowd. Color coding represents the delay of the MPCs in meter. We can see that clusters with large delays are captured.

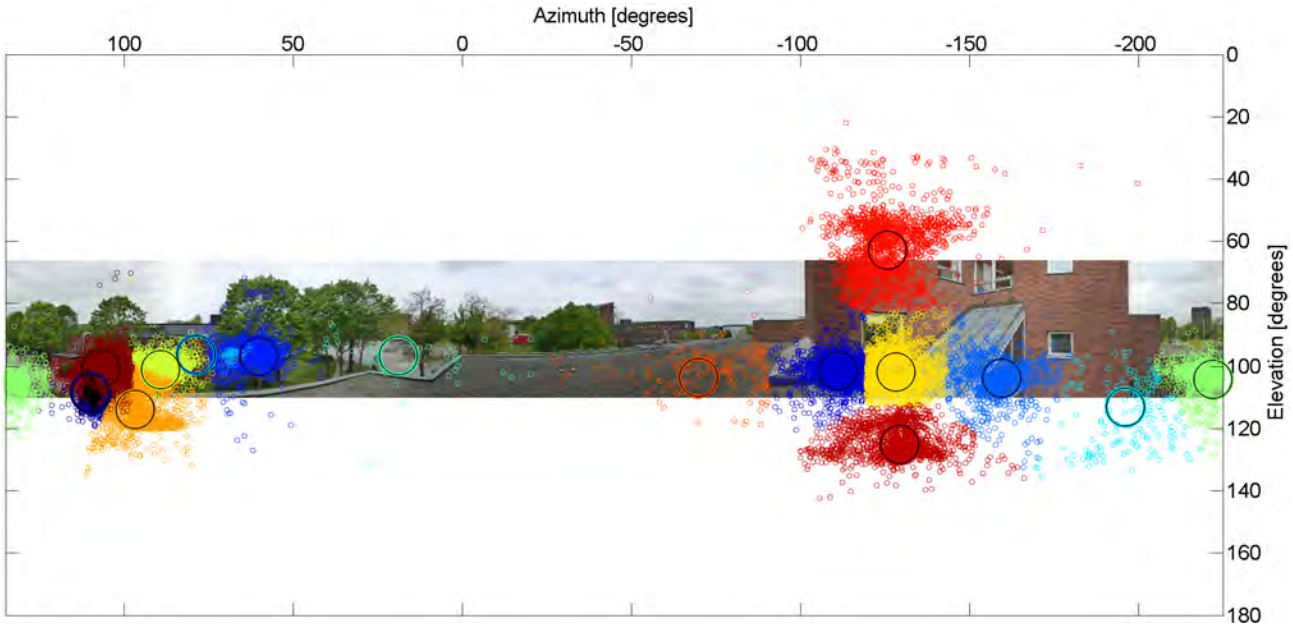

Figure 6.27: Clusters based on MPCs from all 9 users in all 300 snapshots, Site 1, with crowd. There are 15 clusters. Color coding represents different clusters.

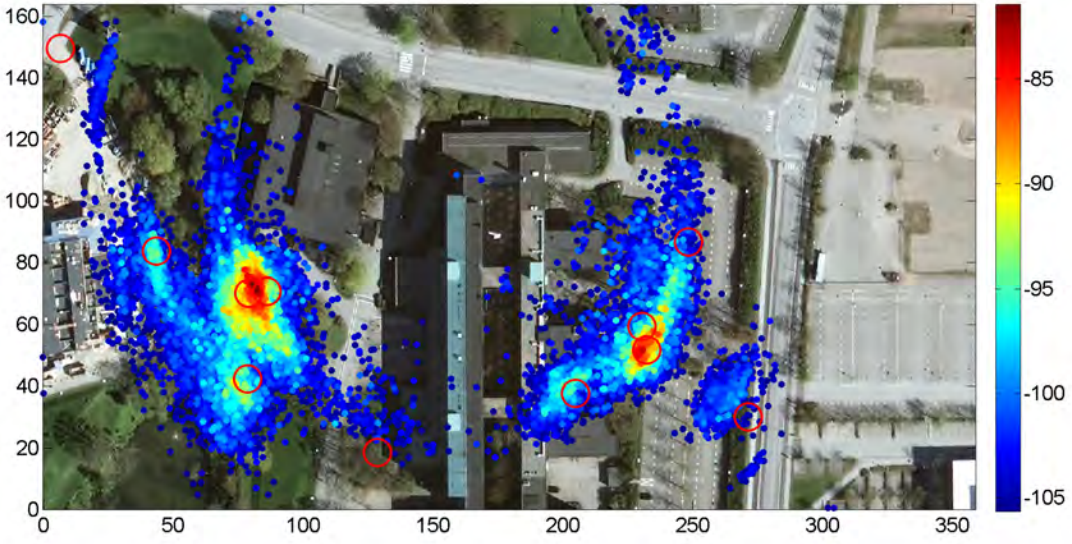

Figure 6.28: MPC strengths from all 9 users in all 300 snapshots, Site 10 (at entrance of study center), with crowd. Color coding represents the channel gain of the MPCs in dB. Here we can see clusters are separated in delay and azimuth angle.

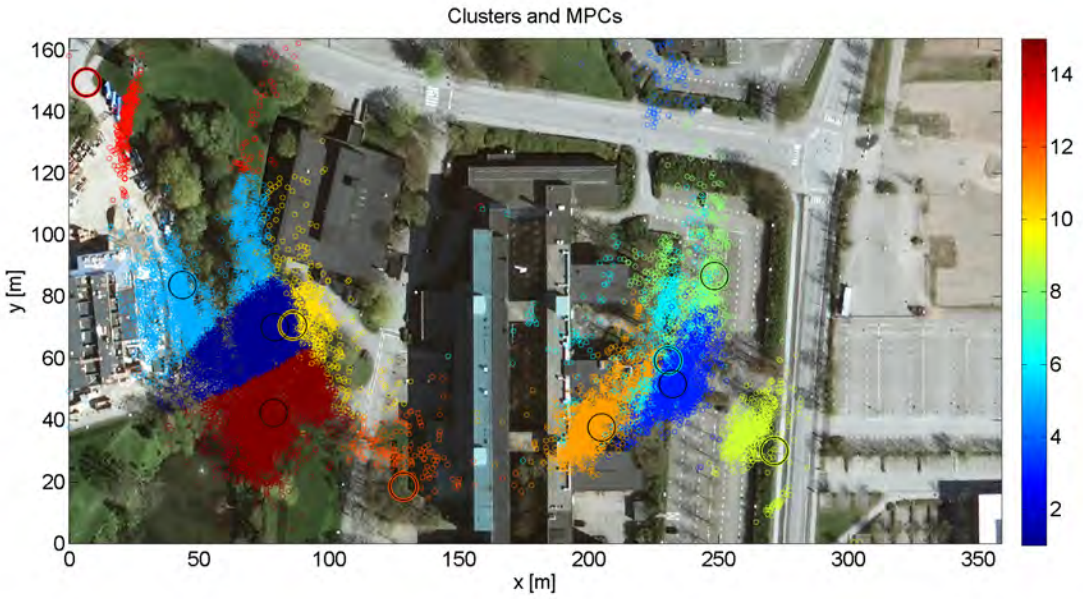

Figure 6.29: Clusters based on MPCs from all 9 users in all 300 snapshots, Site 10 (at entrance of study center), with crowd. There are 15 clusters. Color coding represents different clusters.

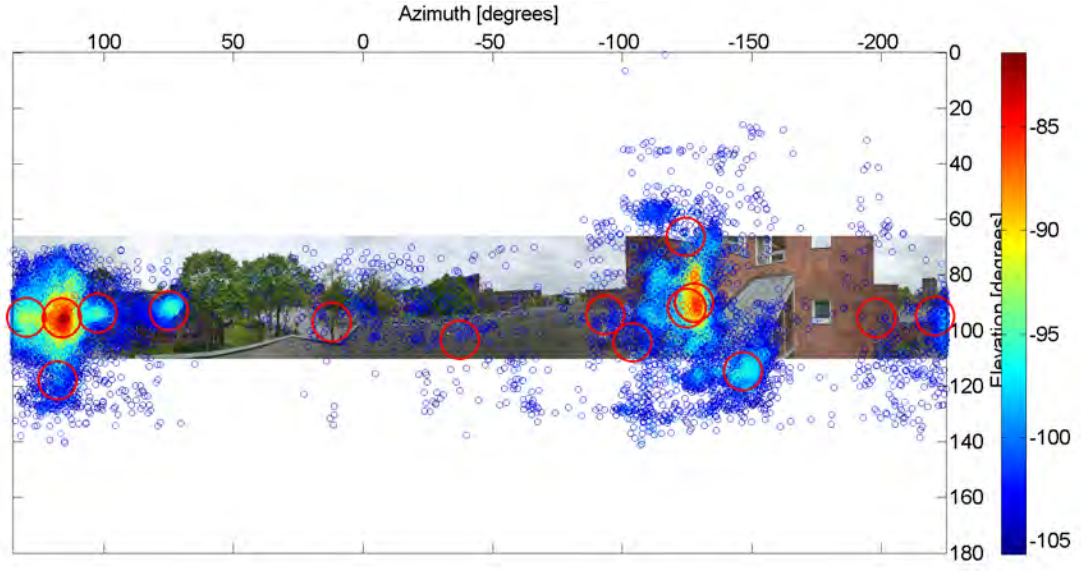

Figure 6.30: MPC strengths from all 9 users in all 300 snapshots, Site 10 (at entrance of study center), with crowd. Color coding represents the channel gain of the MPCs in dB. Here we see how the incoming energy is distributed in azimuth and elevation.

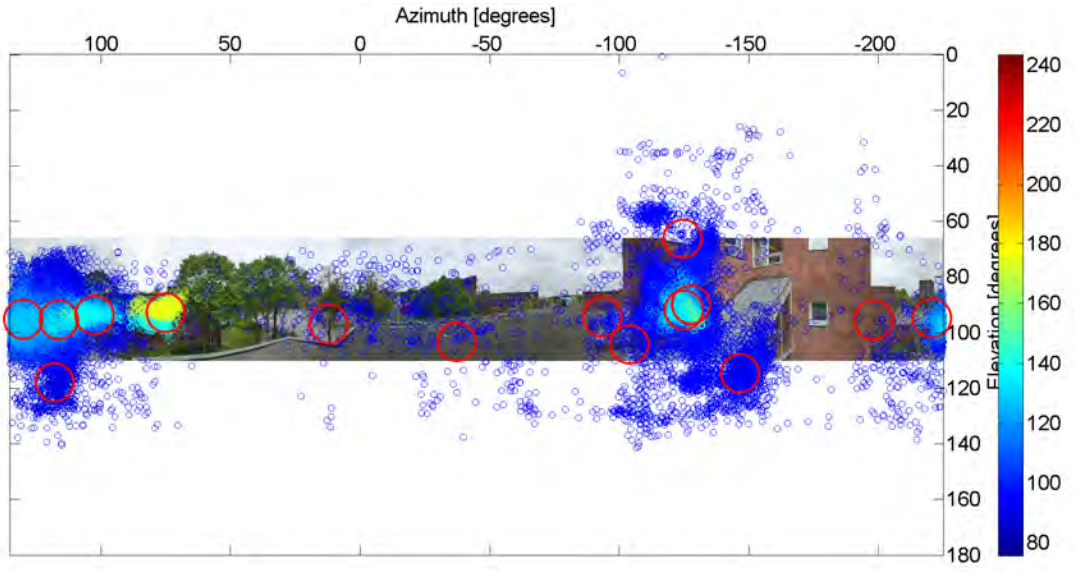

Figure 6.31: MPC delays from all 9 users in all 300 snapshots, Site 10 (at entrance of study center), with crowd. Color coding represents the delay of the MPCs in meter. Clusters with large delays are captured.

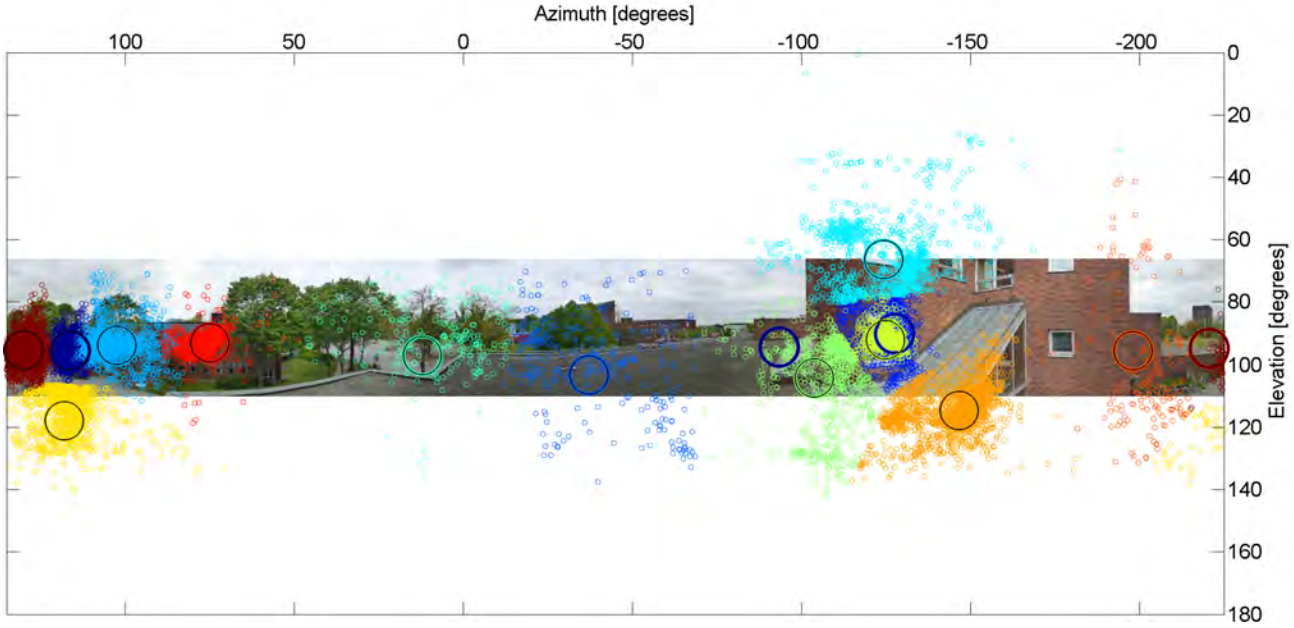

Figure 6.32: Clusters based on MPCs from all 9 users in all 300 snapshots, Site 10 (at entrance of study center), with crowd. There are 15 clusters. Color coding represents different clusters.

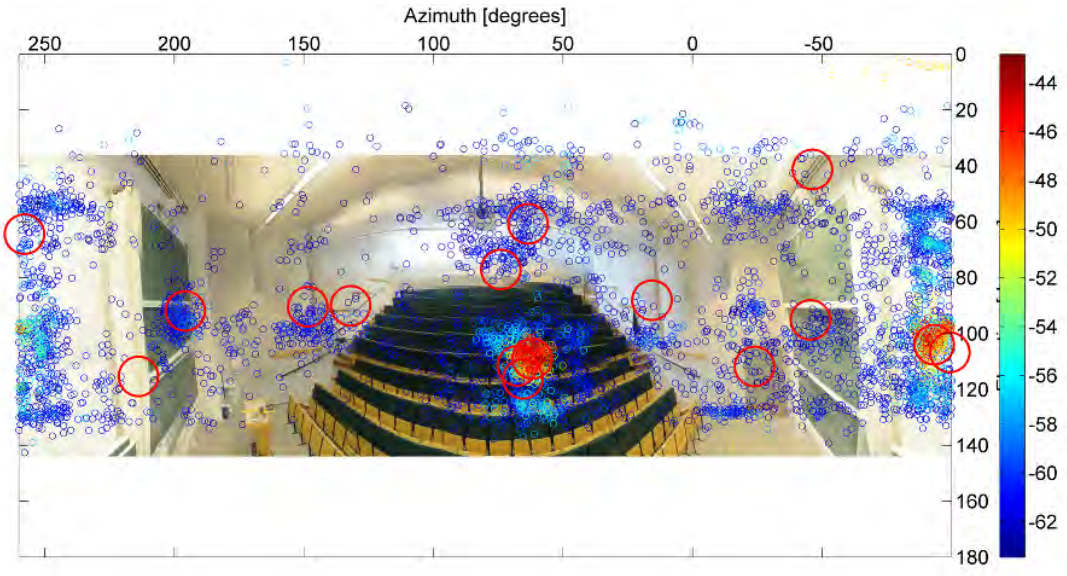

Figure 6.33: MPC strengths from user 1 in all 300 snapshots. Color coding represents the channel gain of the MPCs in dB. BS position 1, user group 1 (center seats), user arrangement 1, without crowd.

Indoor scenarios

Next we report the clustering results for indoor environment based on multipath components from one users in all snapshot. Panorama pictures with multipath components and clusters on top illustrate how the incoming energy is distributed in the auditorium room. Fig. 6.33- Fig. 6.37 show the situation for user 1 that sits in the center of the room, BS is at position 1, without crowd. Among these, in Fig. 6.36 and Fig. 6.37 we assume multipath components and clusters are single-bounce and calculate the scattering points in the room. When plotting these scattering points and clusters on top of the room plan, the "real" single-bounced MPCs and clusters will appear inside the room, while multiple-bounce ones may be outside the room. In this way we can estimate the number of single-bounce clusters and the number of multipath-bounce clusters. Multi-bounce clusters are modeled as "twin clusters" in the COST 2100 model.

Fig. 6.38- Fig. 6.42 illustrate the situation of user 1 that sits at one of the back seats in the room, while base station is at position 1, i.e., the center front of the room.

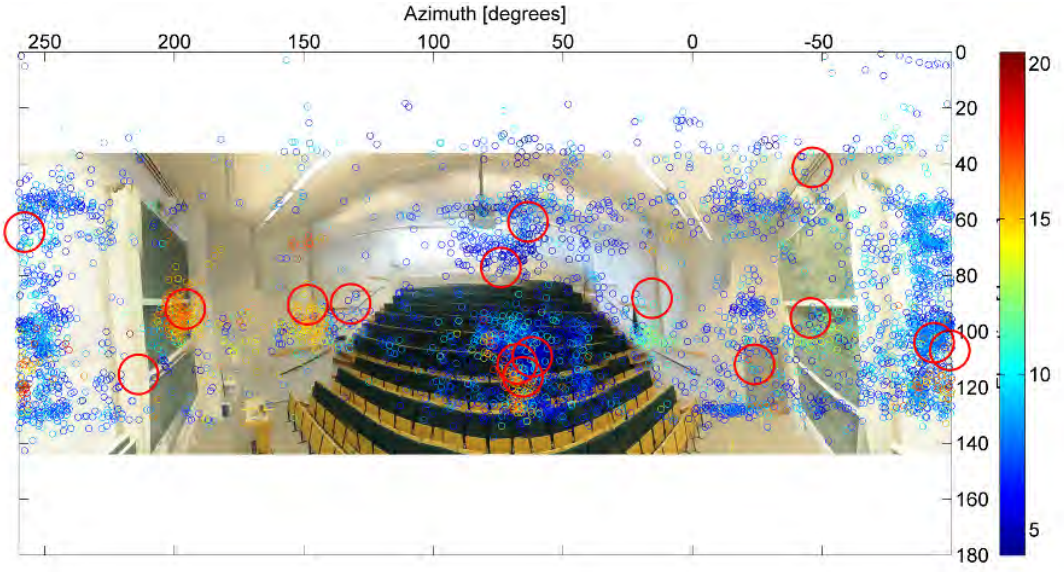

Figure 6.34: MPC delays from user 1 in all 300 snapshots. Color coding represents the delay of the MPCs in meter. BS position 1, user group 1 (center seats), user arrangement 1, without crowd.

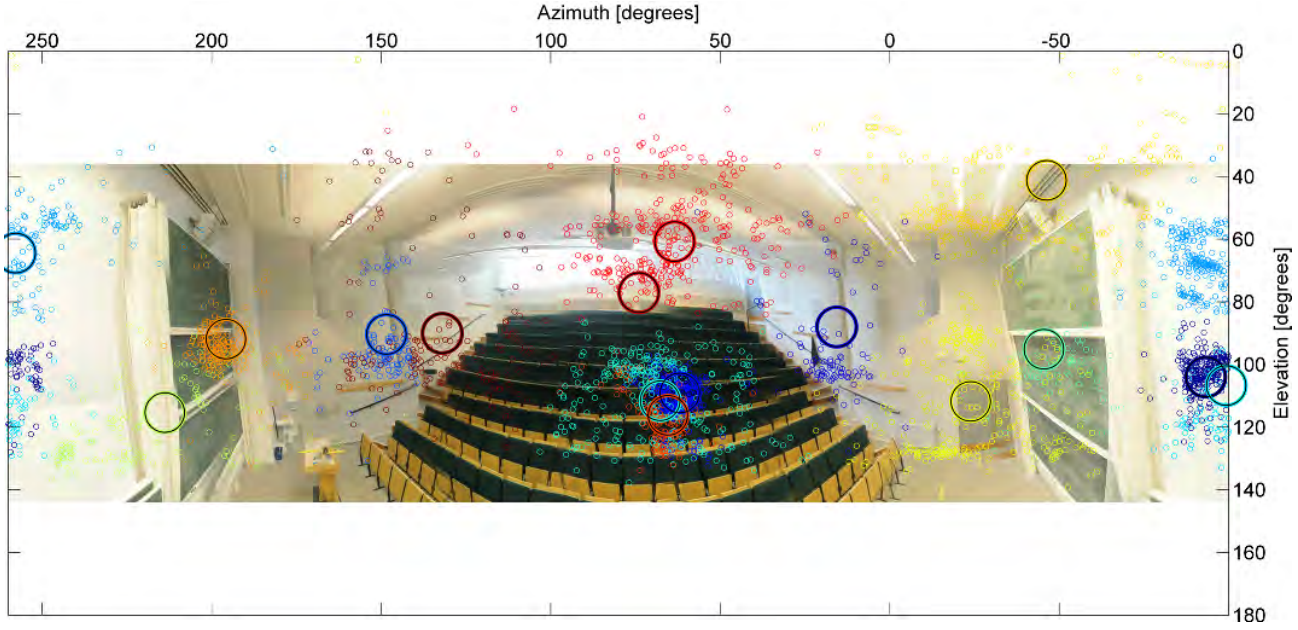

Figure 6.35: Clusters and MPCs from user 1 in all 300 snapshots. Color coding represents different clusters. BS position 1, user group 1 (center seats), user arrangement 1, without crowd. There are 15 clusters.

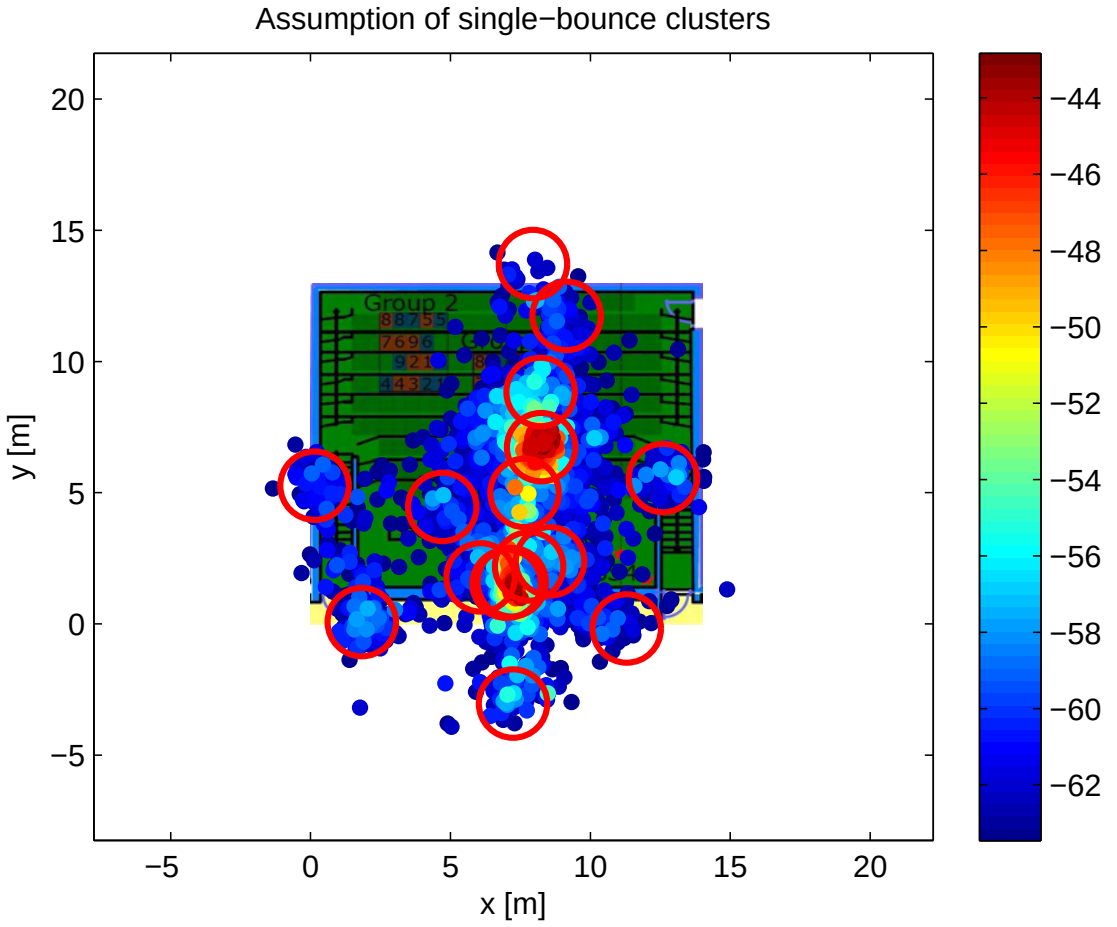

Figure 6.36: Single-bounce scatterers from user 1 in all 300 snapshots. Color coding represents the channel power contribution of the scatterers in dB. There are 16 clusters, among which at least 12 are single-bounced clusters. BS position 1, user group 1 (center seats), user arrangement 1, without crowd. Here we clearly see strong incoming energy from the center seats and reflections on the walls.

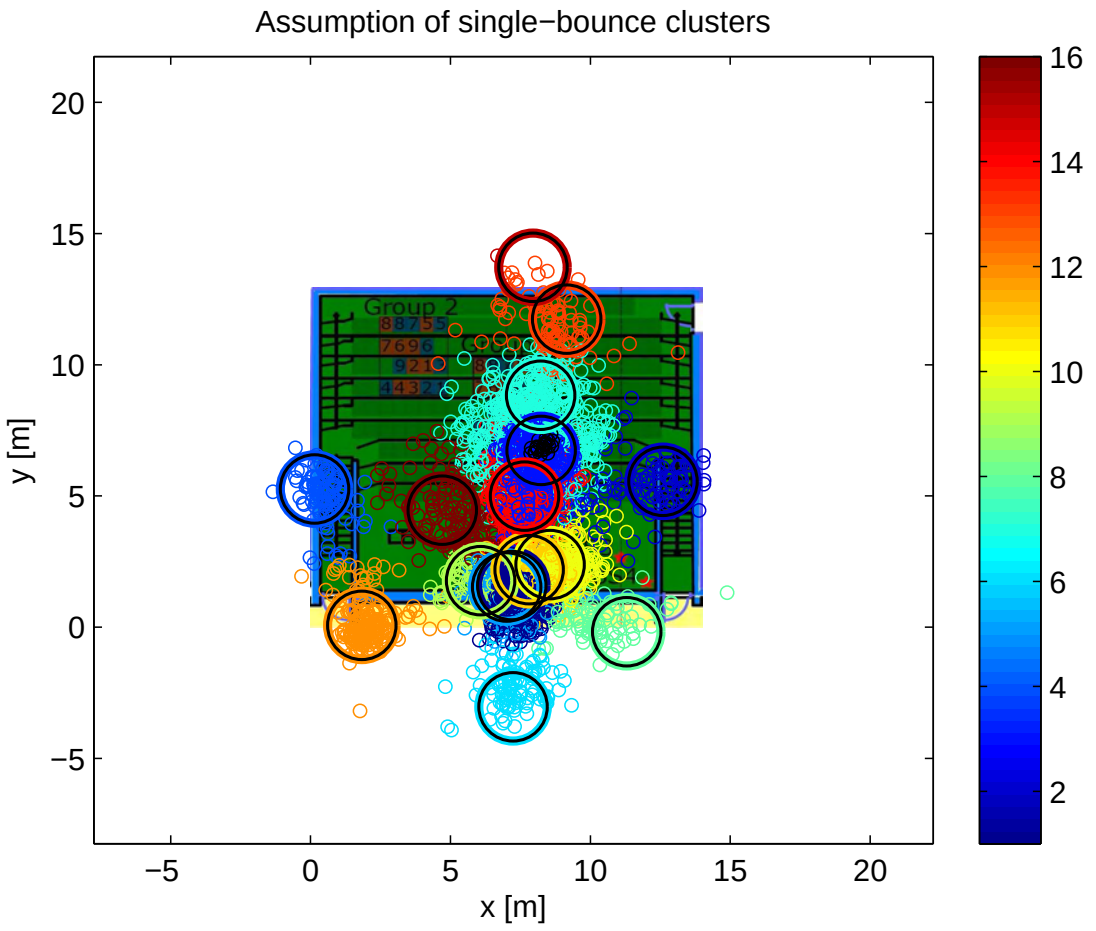

Figure 6.37: Scatterers based on single-bounce assumption, from user 1 in all 300 snapshots. Color coding represents different clusters. There are 16 clusters, among which at least 12 are single-bounced clusters. BS position 1, user group 1 (center seats), user arrangement 1, without crowd.

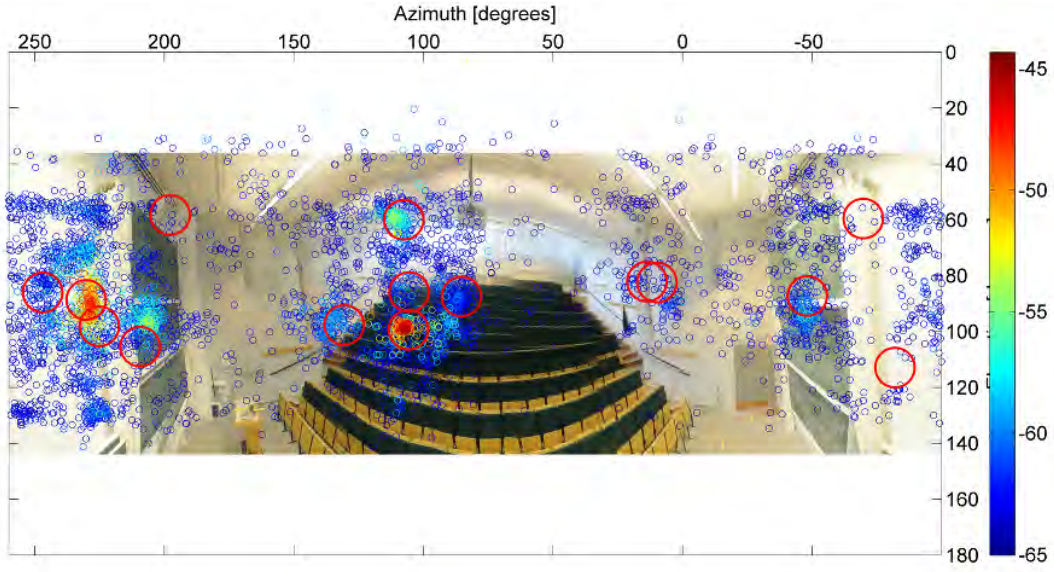

Figure 6.38: MPC strengths from user 1 in all 300 snapshots. Color coding represents the channel power contribution of the MPCs in dB. BS position 1, user group 2 (back seats), user arrangement 1, without crowd.

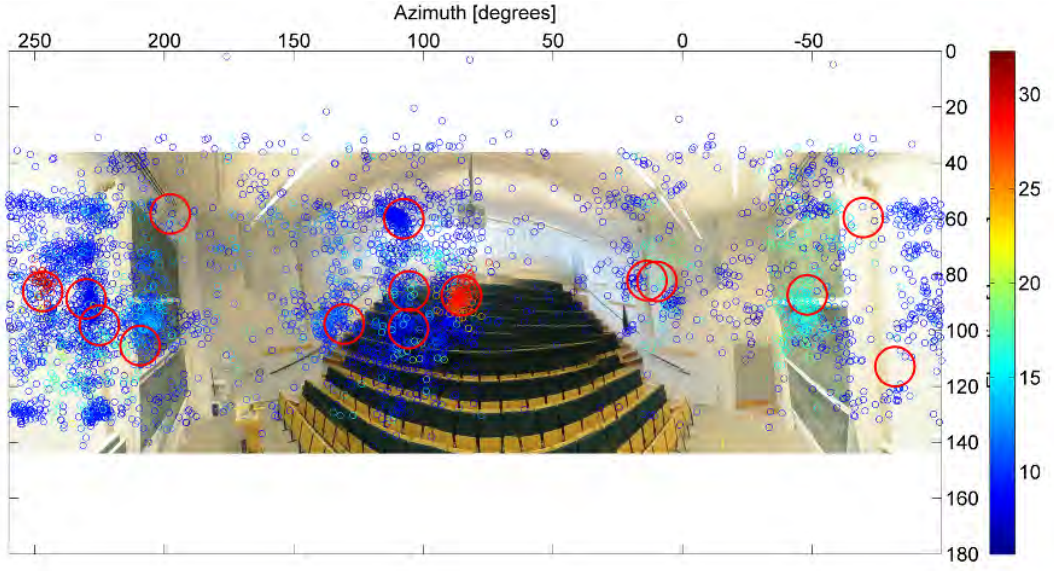

Figure 6.39: MPC delays from user 1 in all 300 snapshots. Color coding represents the delay of the MPCs in meter. BS position 1, user group 2 (back seats), user arrangement 1, without crowd.

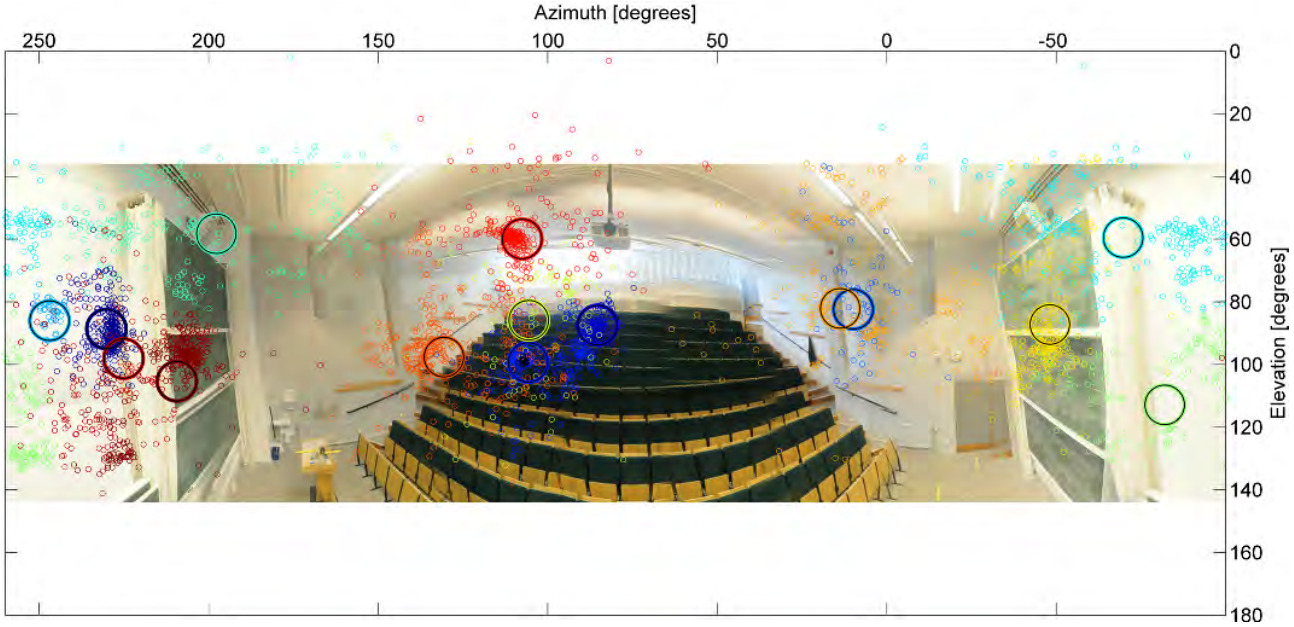

Figure 6.40: Clusters and MPCs from user 1 in all 300 snapshots. Color coding represents different clusters. BS position 1, user group 2 (back seats), user arrangement 1, without crowd. There are 15 clusters.

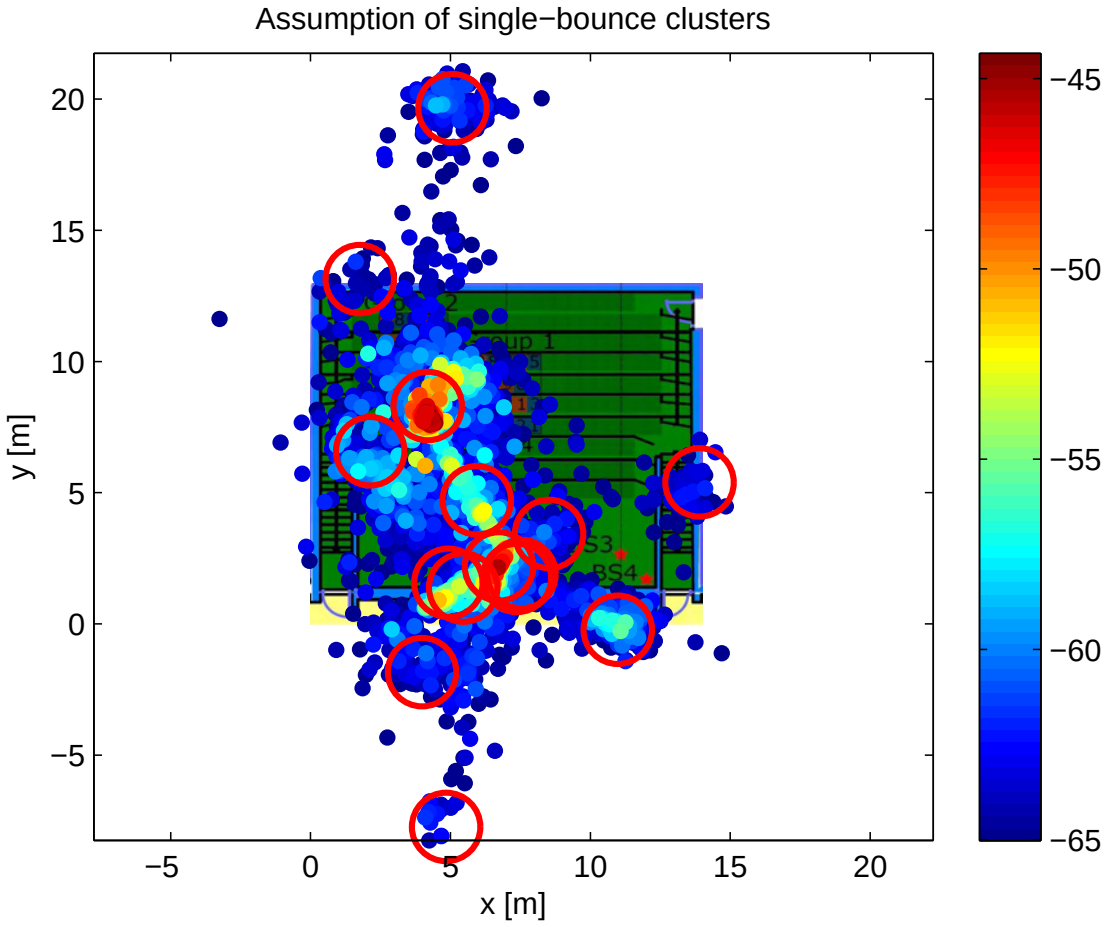

Figure 6.41: Single-bounce scatterers from user 1 in all 300 snapshots. Color coding represents the channel power contribution of the scatterers in dB. There are 15 clusters, among which 11 are single-bounced clusters. BS position 1, user group 2 (back seats), user arrangement 1, without crowd. We can see that strong incoming energy from the back seats and the back-left corner of the room, as well as the front wall and the right wall.

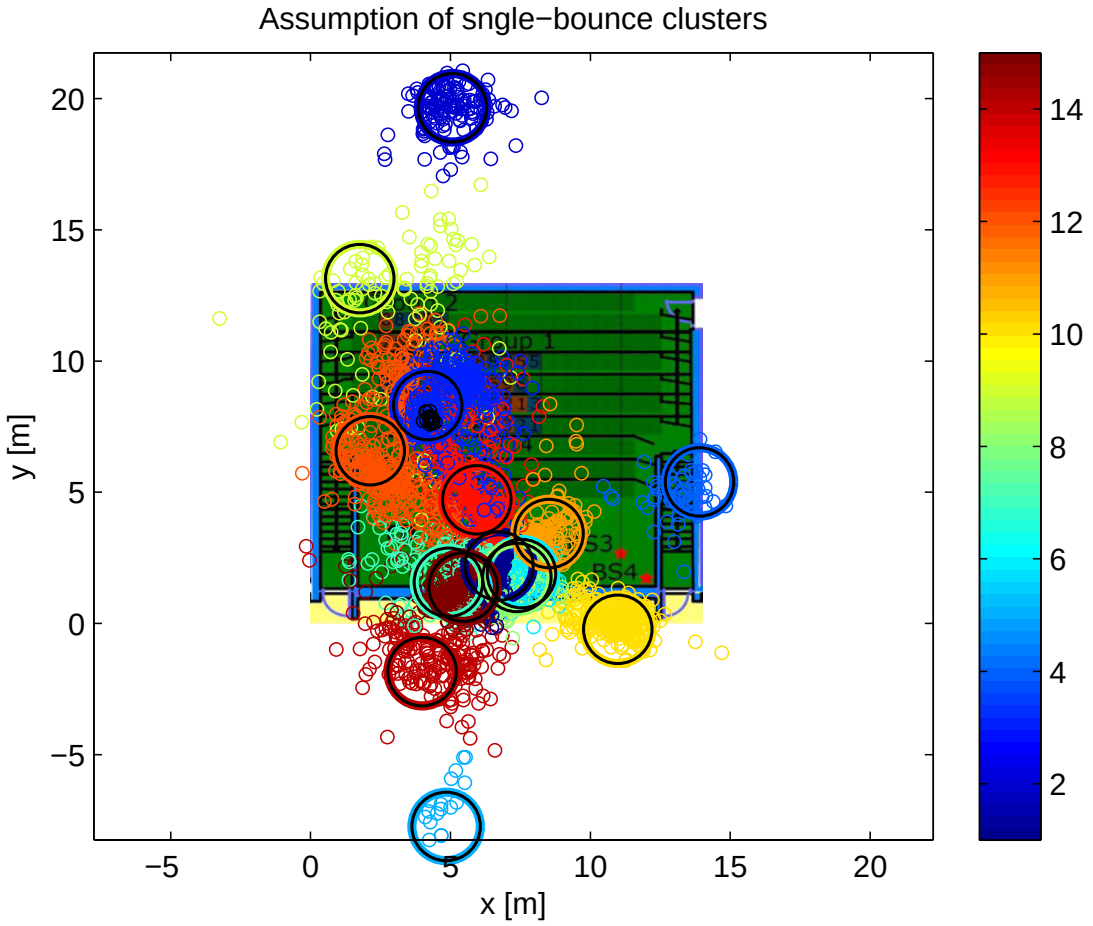

Figure 6.42: Scatterers based on single-bounce assumption, from user 1 in all 300 snapshots. Color coding represents different clusters. There are 15 clusters, among which 11 are single-bounced clusters. BS position 1, user group 2 (back seats), user arrangement 1, without crowd.

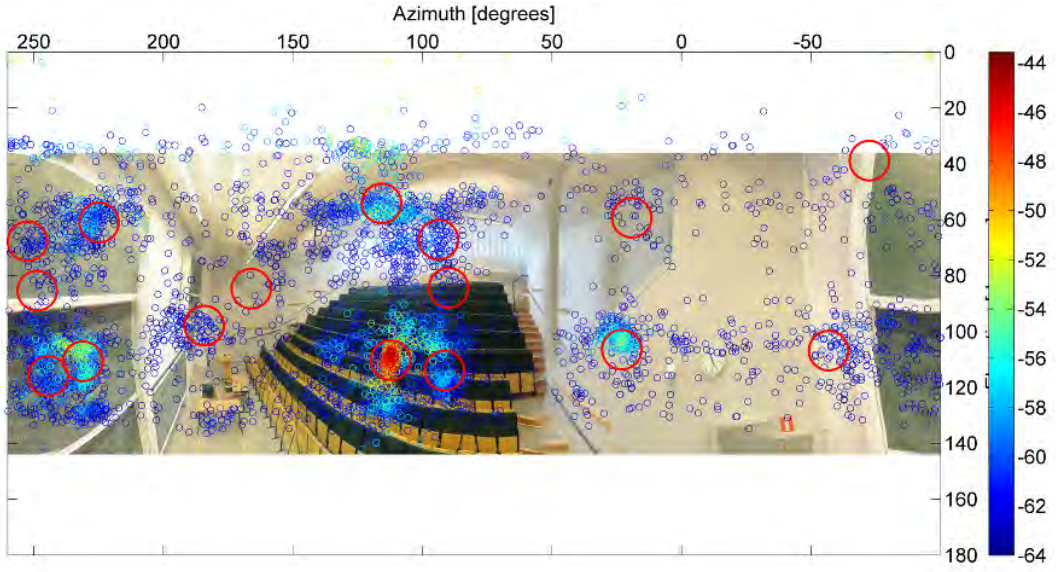

Figure 6.43: MPC strengths from user 1 in all 300 snapshots. Color coding represents the channel power contribution of the MPCs in dB. BS position 3, user group 1 (center seats), user arrangement 1, without crowd.

Table 6.5: Cluster information for all outdoor measurements.

	LOS scenario				NLOS scenario			
	Site 1		Site 2		Site 8		Site 10	
	Crowd	No crowd	Crowd	No crowd	Crowd	No crowd	Crowd	No crowd
No. of clusters	15	16	15	12	13	14	15	15
Cluster delay spread (m)	6	6	7	7	20	19	22	17
Cluster azimuth spread (deg)	9	9	9	9	10	9	11	9
Cluster elevation spread (deg)	7	7	7	8	8	9	10	9
No. of cluster MPCs per user[1]	3	3	2	3	7	6	6	6
No. of cluster MPCs all users[2]	31	31	19	25	61	58	56	56
Arvg. K-factor (dB)	9	9	15	13	-	-	-	-

[1] Number of MPCs per cluster per user in one snapshot.
[2] Number of MPCs per cluster fro all users in one snapshot.

Fig. 6.43- Fig. 6.47 illustrate the situation of user 1 that sits at one of the center seats in the room, while base station is at position 3, i.e., the corner of the room.

Fig. 6.48- Fig. 6.52 illustrate the situation of user 1 that sits at one of the back seats in the room, while base station is at position 3, i.e., the corner of the room.

6.5.3 Cluster parameters

Cluster information for all outdoor measurement cases are listed in Table 6.5.

From Table 6.5, we see that the number of clusters for outdoor scenarios are 12-16. The cluster spreads in delay and azimuth angle are larger in NLOS scenarios than those in LOS scenarios, while the cluster spreads in elevation are similar for both LOS and NLOS scenarios. This indicates that energy are more spread out in radio channels under NLOS conditions. If considering all users, the number of MPCs per cluster is 19-31 in LOS scenarios, while more in NLOS scenarios, i.e., 56-61. If considering per user case, the number of MPCs per cluster is 2-3 in LOS and 6-7 in NLOS. In massive MIMO channels, closely-spaced users may "see" a cluster

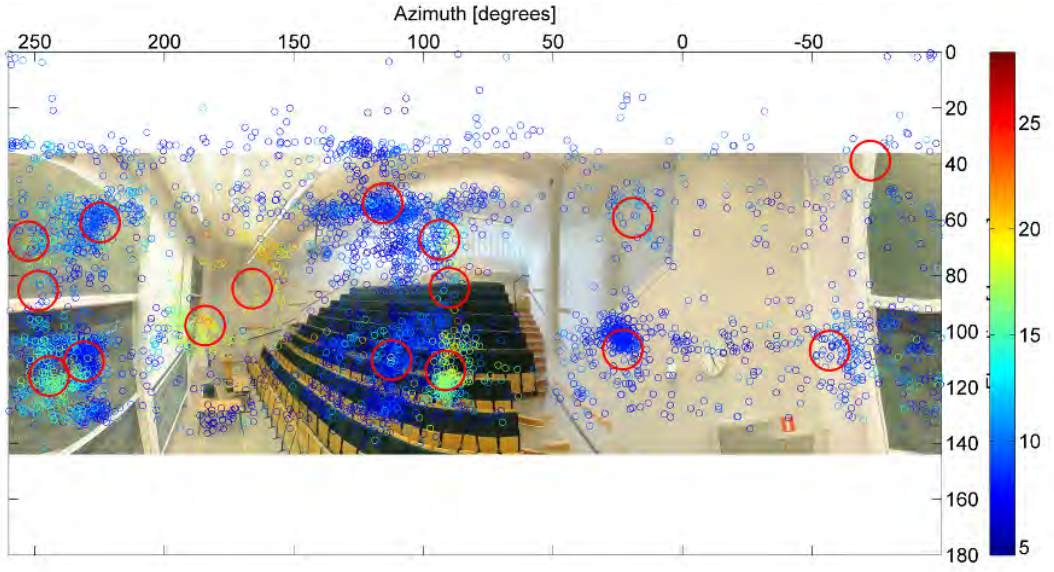

Figure 6.44: MPC delays from user 1 in all 300 snapshots. Color coding represents the delay of the MPCs in meter. BS position 3, user group 1 (center seats), user arrangement 1, without crowd.

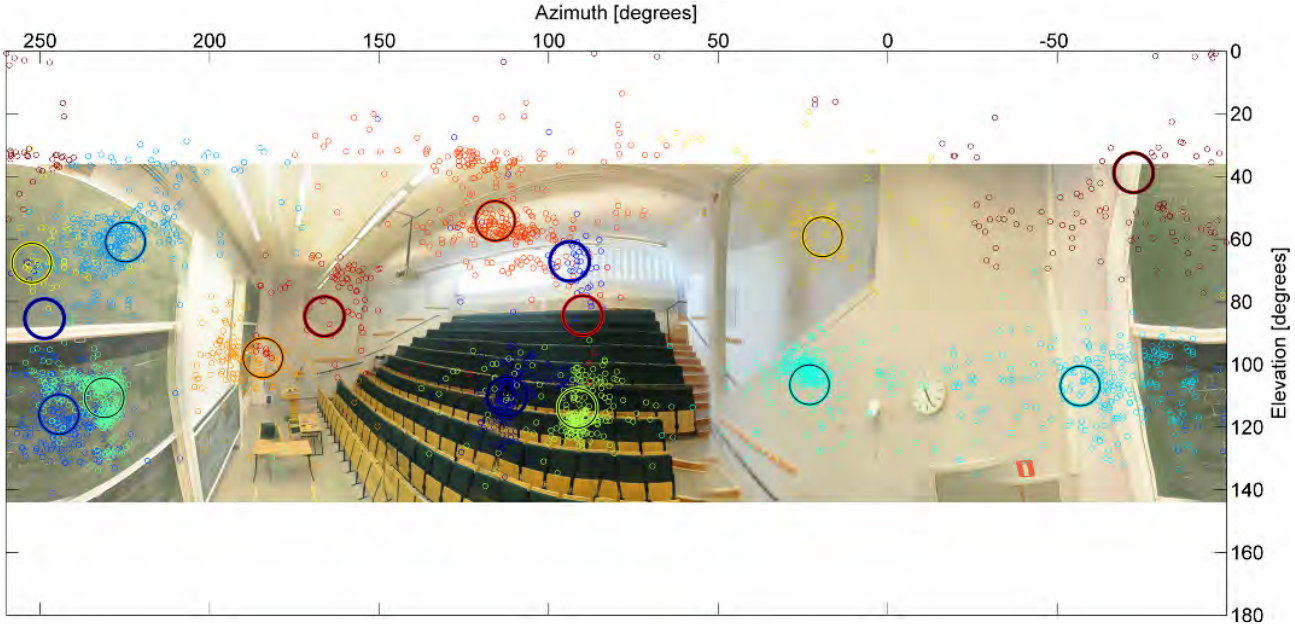

Figure 6.45: Clusters and MPCs from user 1 in all 300 snapshots. Color coding represents different clusters. There are 15 clusters. BS position 3, user group 1 (center seats), user arrangement 1, without crowd.

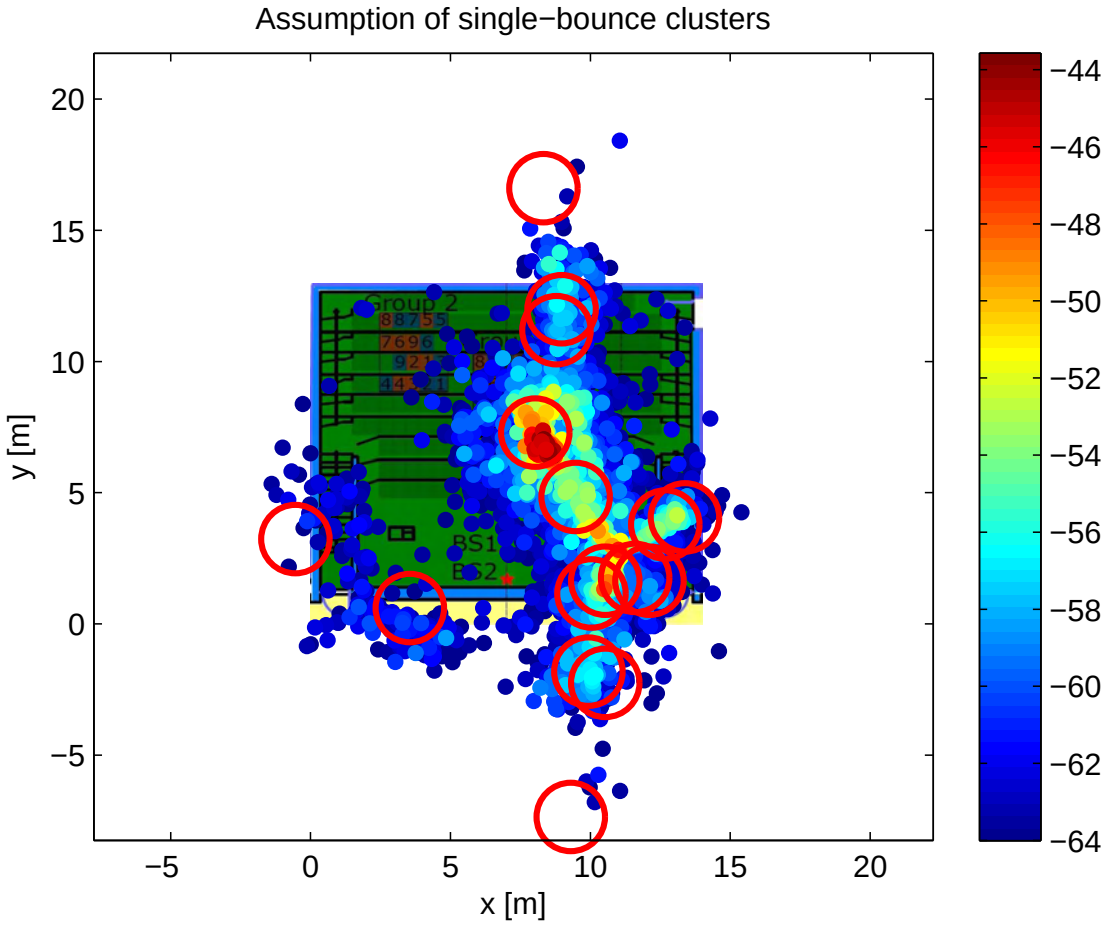

Figure 6.46: Single-bounce scatterers from user 1 in all 300 snapshots. Color coding represents the channel power contribution of the scatterers in dB. There are 16 clusters, among which 12 are single-bounced clusters. BS position 3, user group 1 (center seats), user arrangement 1, without crowd. Strong energy comes from the center seats and the wall corner where the base station is located.

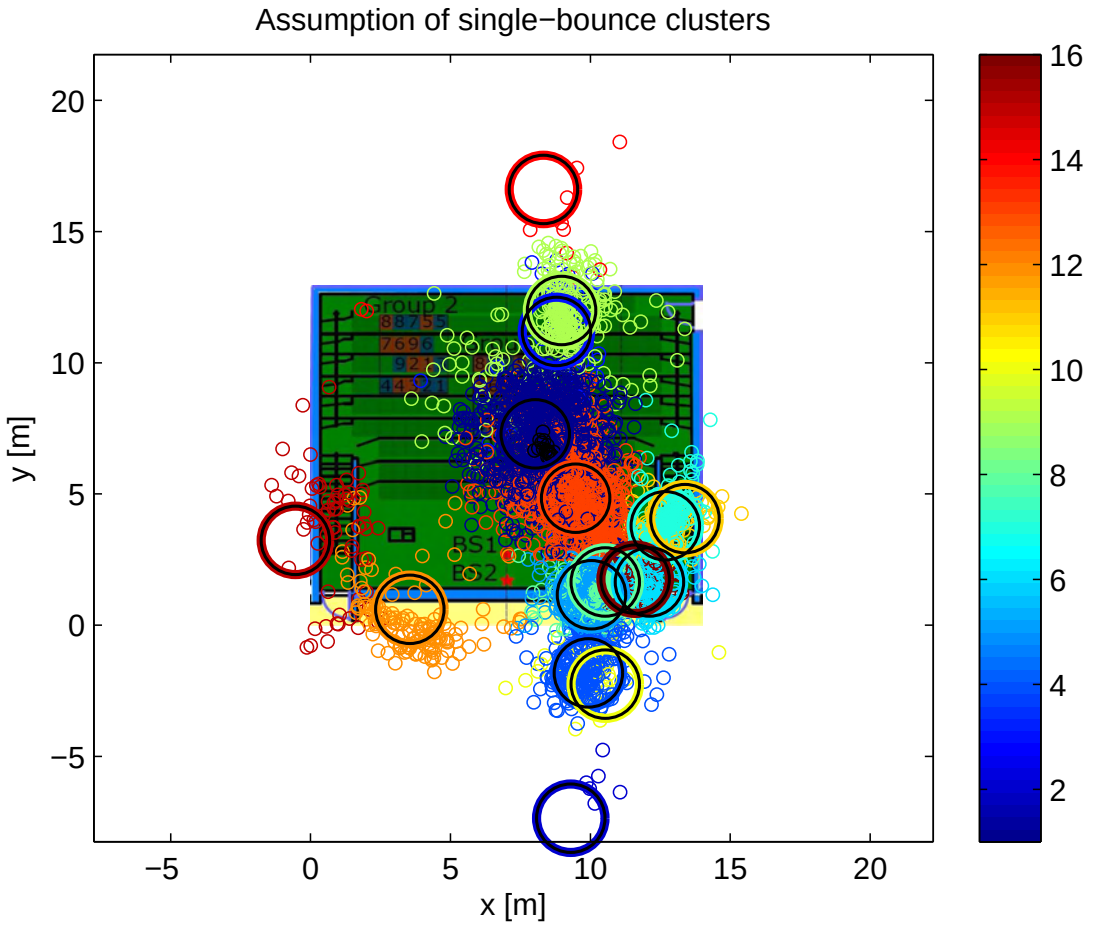

Figure 6.47: Scatterers based on single-bounce assumption, from user 1 in all 300 snapshots. Color coding represents different clusters. There are 16 clusters, among which 12 are single-bounced clusters. BS position 3, user group 1 (center seats), user arrangement 1, without crowd.

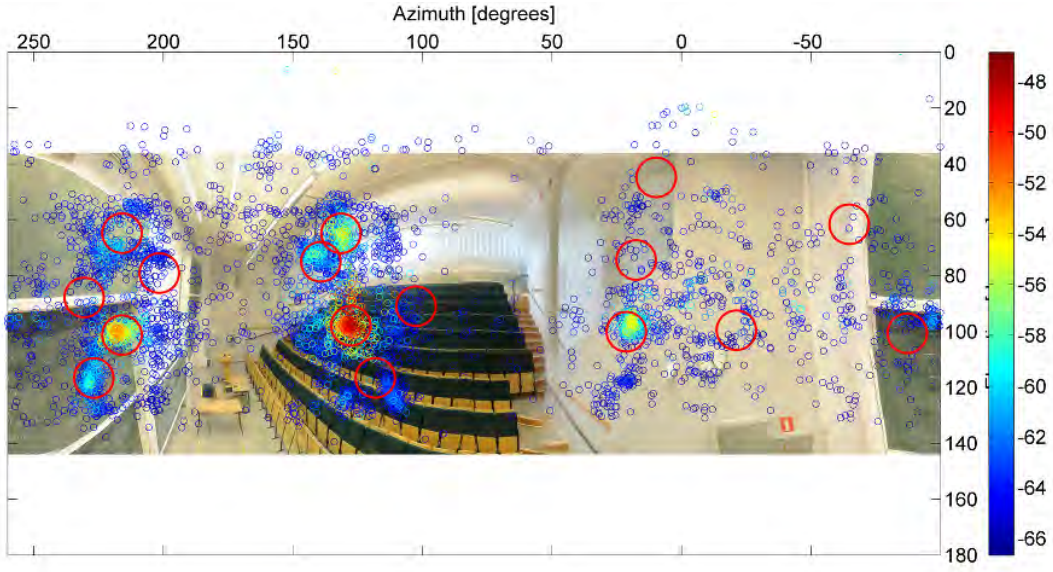

Figure 6.48: MPC strengths from user 1 in all 300 snapshots. Color coding represents the channel power contribution of the MPCs in dB. BS position 3, user group 2 (back seats), user arrangement 1, without crowd.

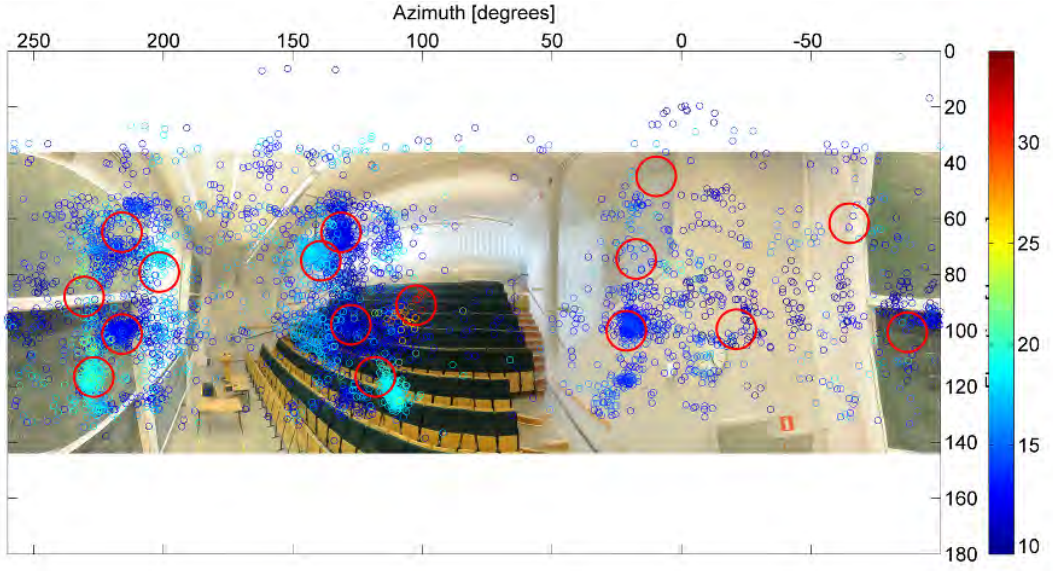

Figure 6.49: MPC delays from user 1 in all 300 snapshots. Color coding represents the delay of the MPCs in meter. BS position 3, user group 2 (back seats), user arrangement 1, without crowd.

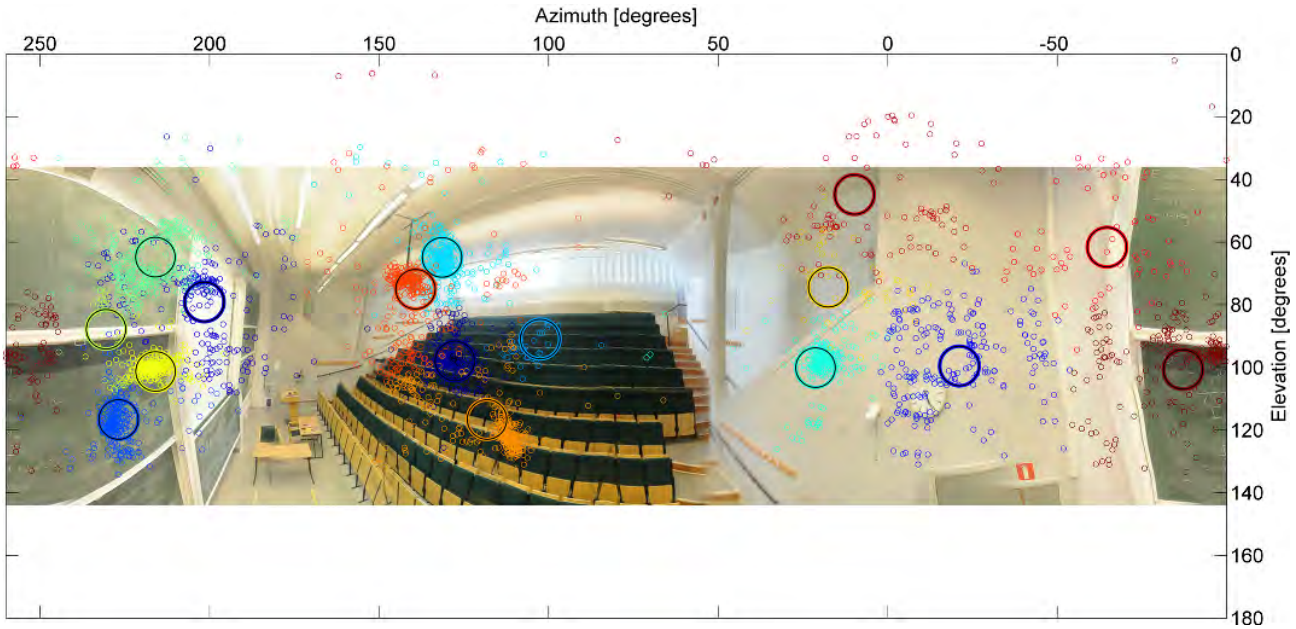

Figure 6.50: Clusters and MPCs from user 1 in all 300 snapshots. Color coding represents different clusters. BS position 3, user group 2 (back seats), user arrangement 1, without crowd. There are 16 clusters.

through different scattering points, depending on their inter-spacing and the distance of the cluster to the users. For all users, some scattering points in a cluster may also overlap, hence here we may over-estimate the number of MPCs in one cluster, i.e., less than 19-31 in LOS, less than 56-61 in NLOS. This issue needs further investigation. Besides, the K-factor is higher at site 2 than at site 1. At site 2, the LOS components are obstructed by tree leaves or have diffraction at the roof edge, however, due to less scatterers (buildings) around we experience high K-factors. At site 1, the users are in-between buildings which cause strong scatterings, thus the K-factors are lower in this case.

Next, we extract some cluster parameters which are used in COST 2100 channel model, for outdoor LOS and NLOS scenarios, respectively. These parameters are input to the implementation of the COST 2100 channel model. The statistics of these parameters such as number of MPCs, cluster spread, cluster power decay, shadowing, and LOS power factor are shown in Fig. 6.53-Fig. 6.65. The full parameter sets and values for the COST 2100 channel model is reported in next chapter.

For indoor measurements, since the clustering is performed for single user only and no cluster tracking between users has been done, we only list the information in term of the number of single-bounce clusters in Table 6.6. The ratio of the number of single-bounce clusters among all clusters is around 0.7-0.75, which means most clusters are single-bounce clusters in this indoor environment.

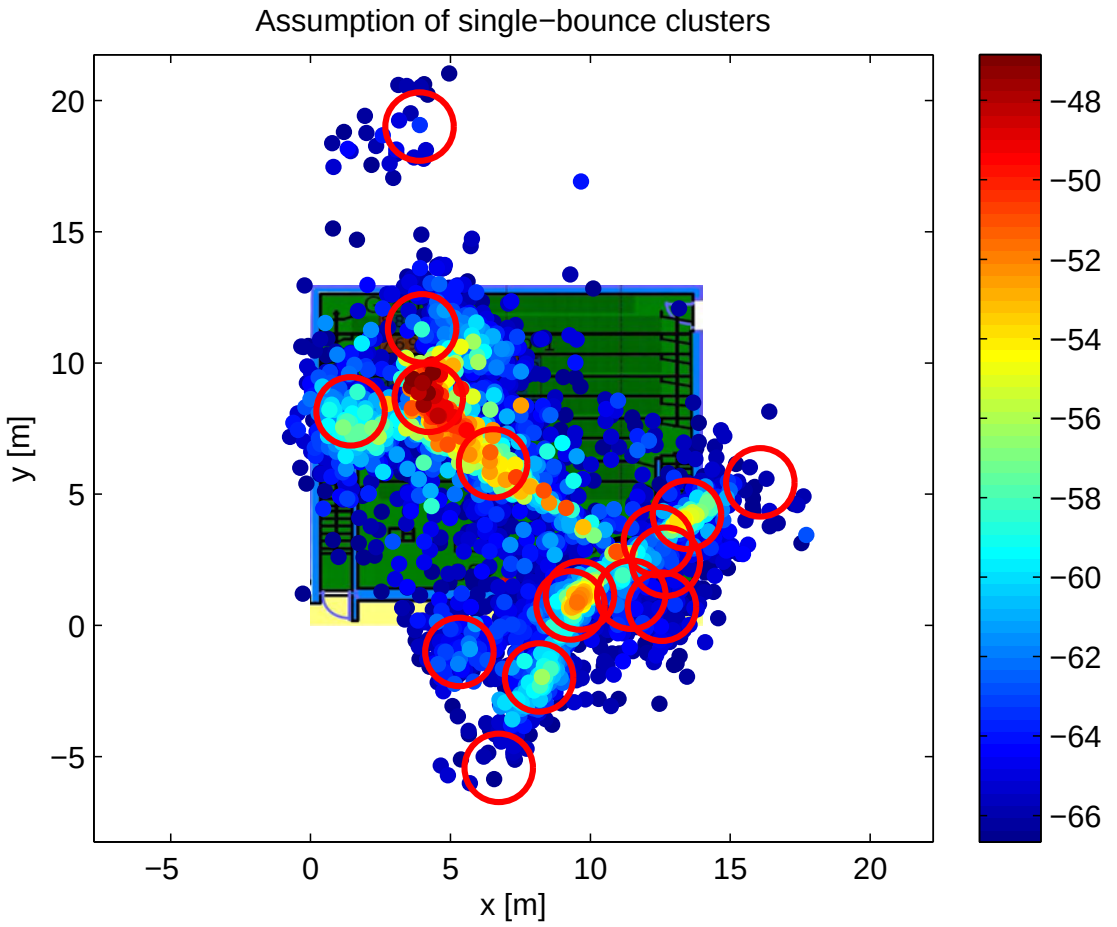

Figure 6.51: Single-bounce scatterers from user 1 in all 300 snapshots. Color coding represents the channel power contribution of the scatterers in dB. There are 16 clusters, among which 11 are single-bounced clusters. BS position 3, user group 2 (back seats), user arrangement 1, without crowd. Strong energy comes the back seats as well as the wall corner where the base station is located.

Table 6.6: Ratio of the number of single-bounce clusters and the number of all types of clusters, from indoor measurements.

	BS position 1		BS position 3	
User position	Center seat	Back seat	Center seat	Back seat
No. of clusters	16	15	16	16
No. of single-bounce clusters	12	11	12	11
Ratio	0.75	0.73	0.75	0.69

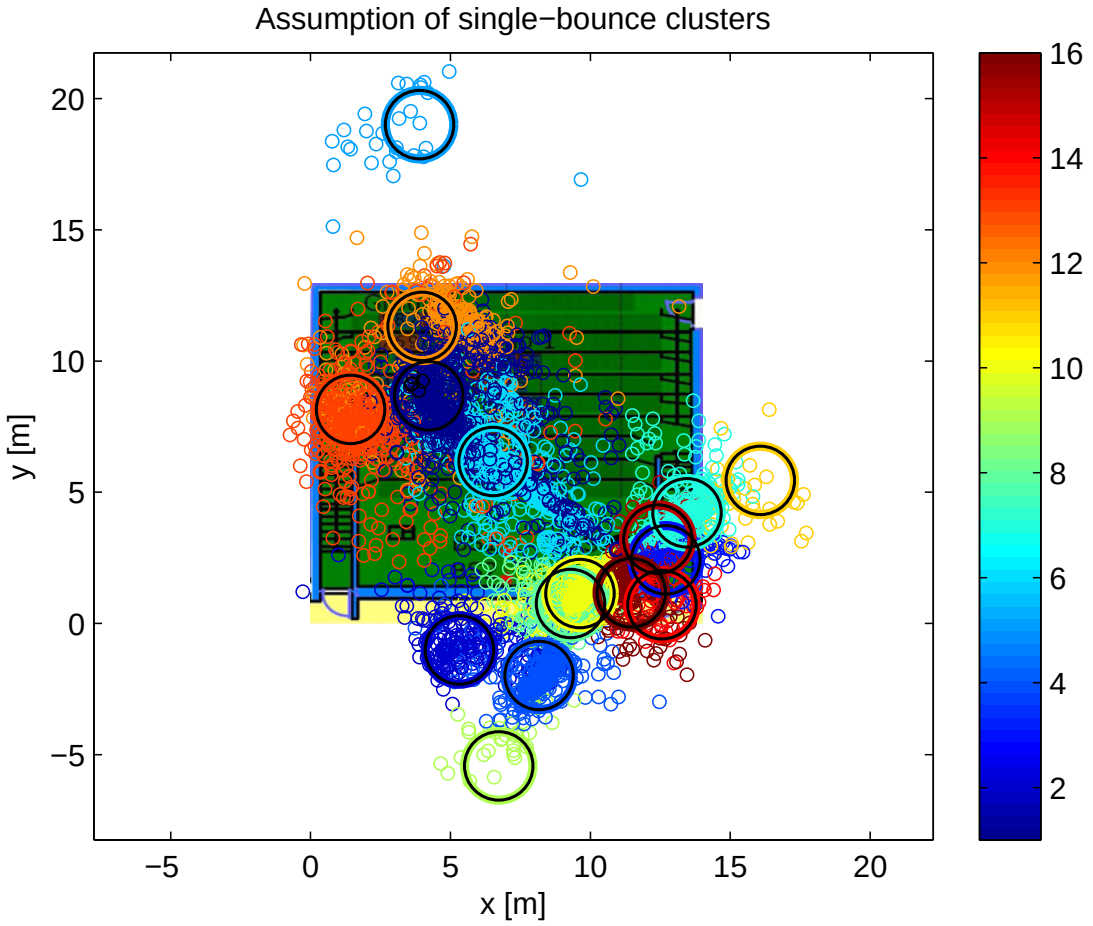

Figure 6.52: Scatterers based on single-bounce assumption, from user 1 in all 300 snapshots. Color coding represents different clusters. There are 16 clusters, among which 11 are single-bounced clusters. BS position 3, user group 2 (back seats), user arrangement 1, without crowd.

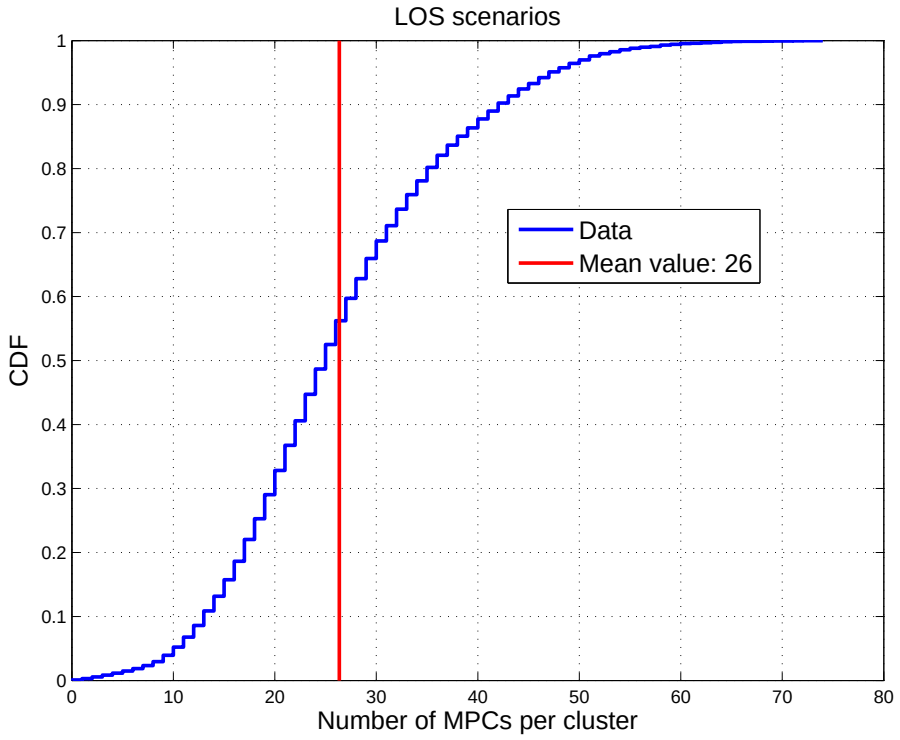

Figure 6.53: CDF of the number of MPCs from all users in one cluster, LOS scenarios.

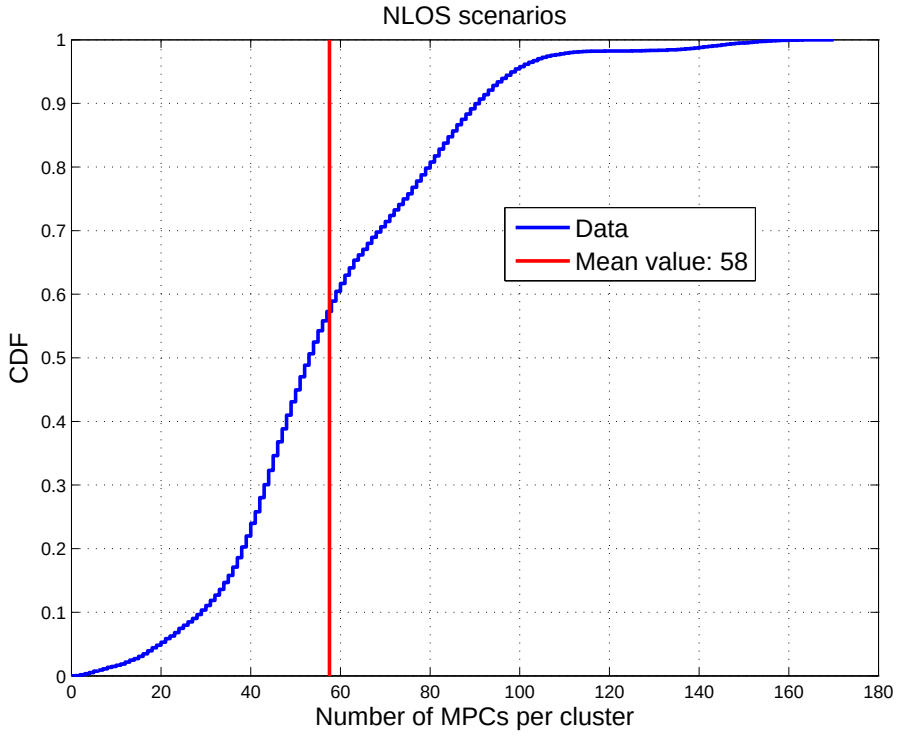

Figure 6.54: CDF of the number of MPCs from all users in one cluster, NLOS scenarios.

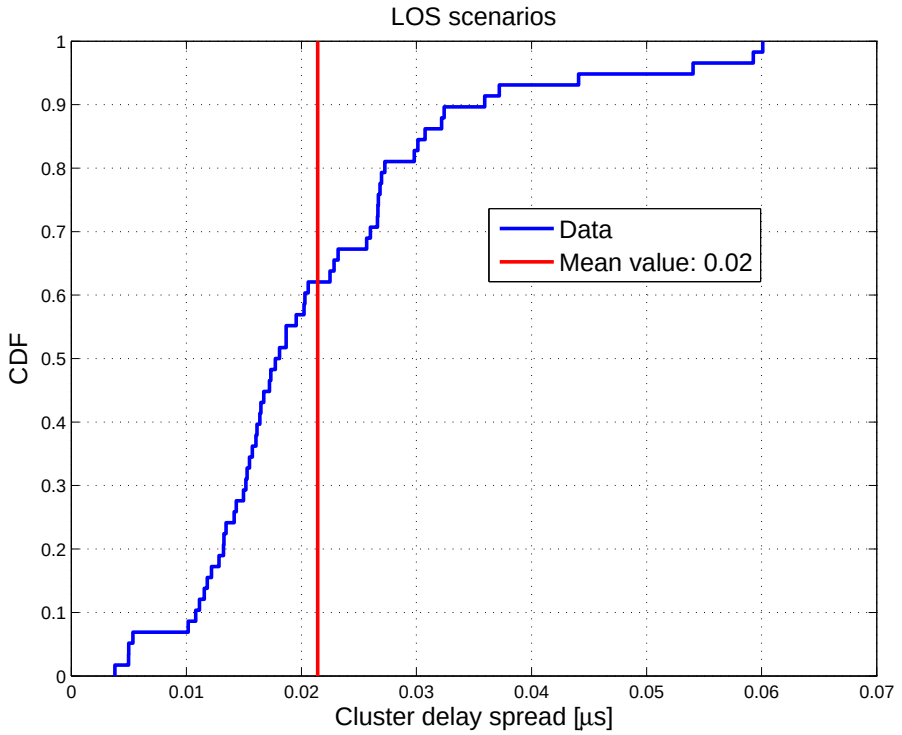

Figure 6.55: CDF of the cluster delay spreads, LOS scenarios.

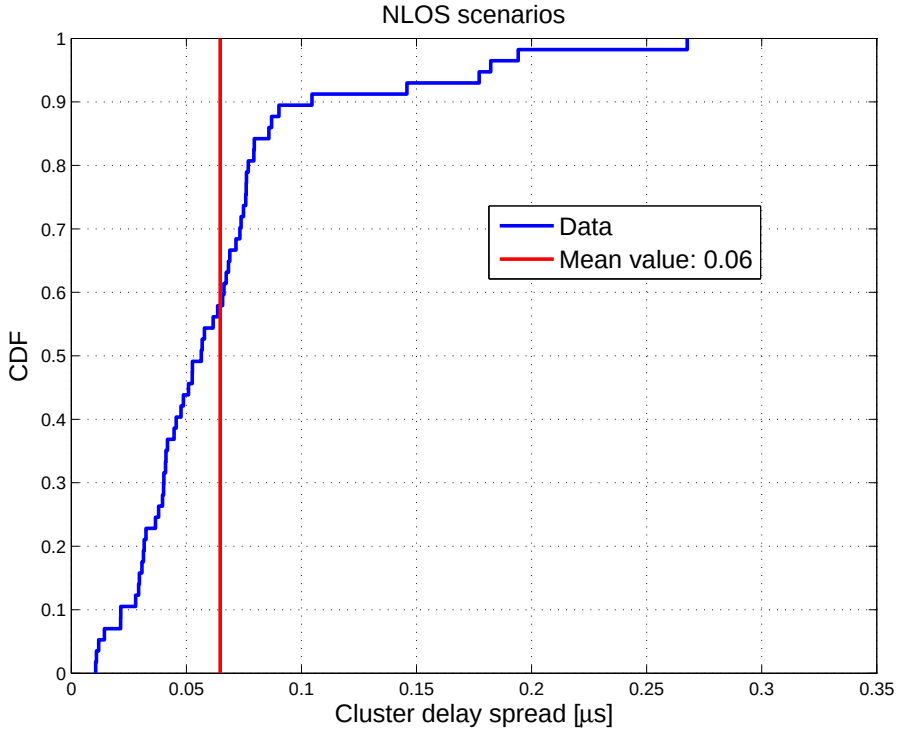

Figure 6.56: CDF of the cluster delay spreads, NLOS scenarios.

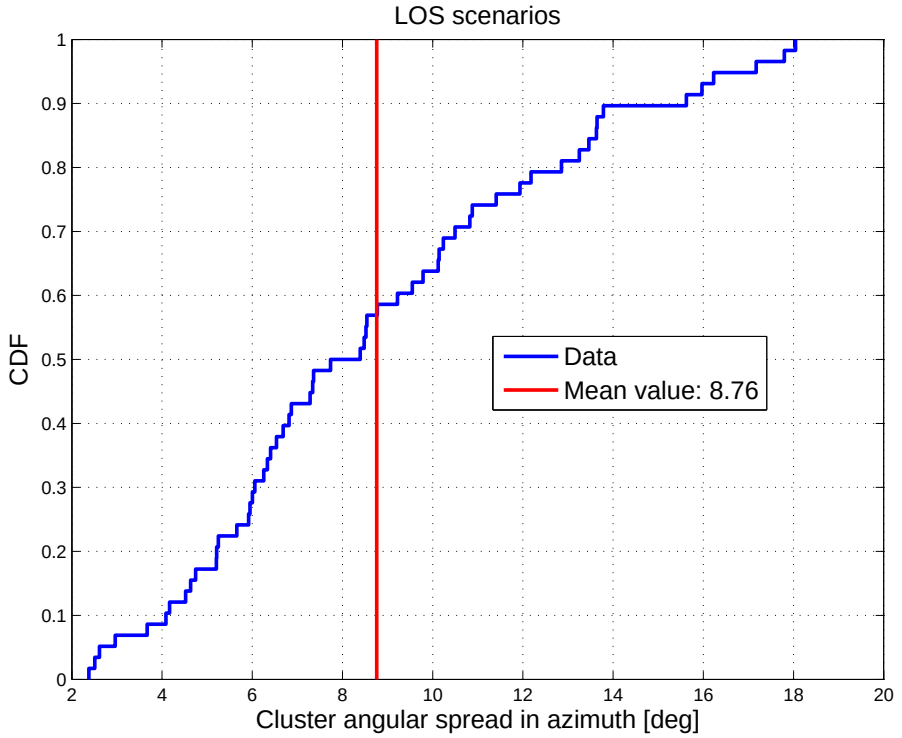

Figure 6.57: CDF of the cluster angular spreads in azimuth, LOS scenarios.

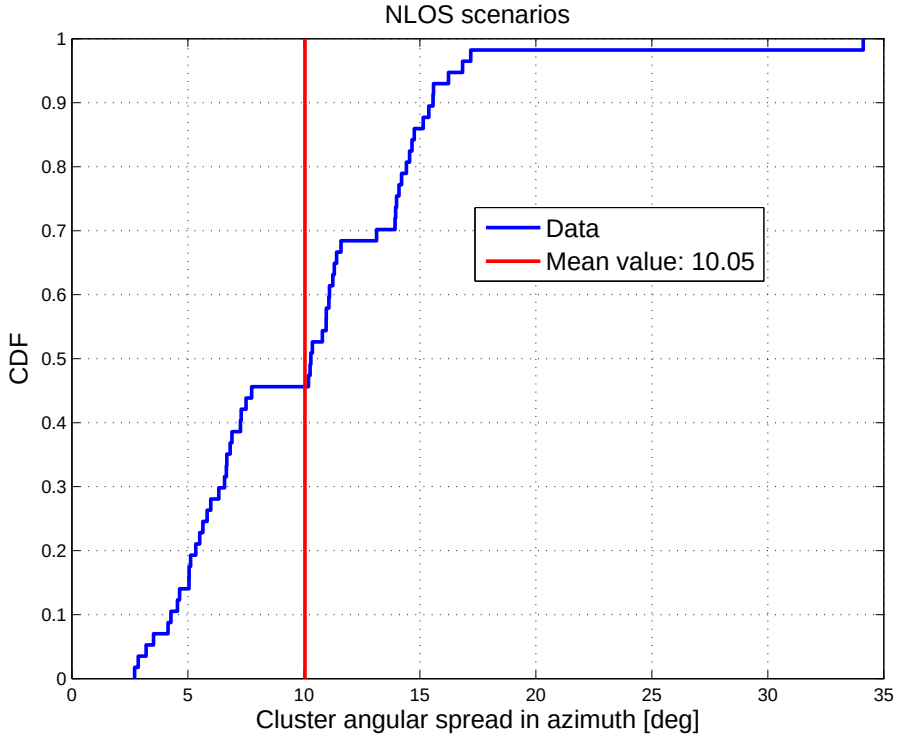

Figure 6.58: CDF of the cluster angular spreads in azimuth, NLOS scenarios.

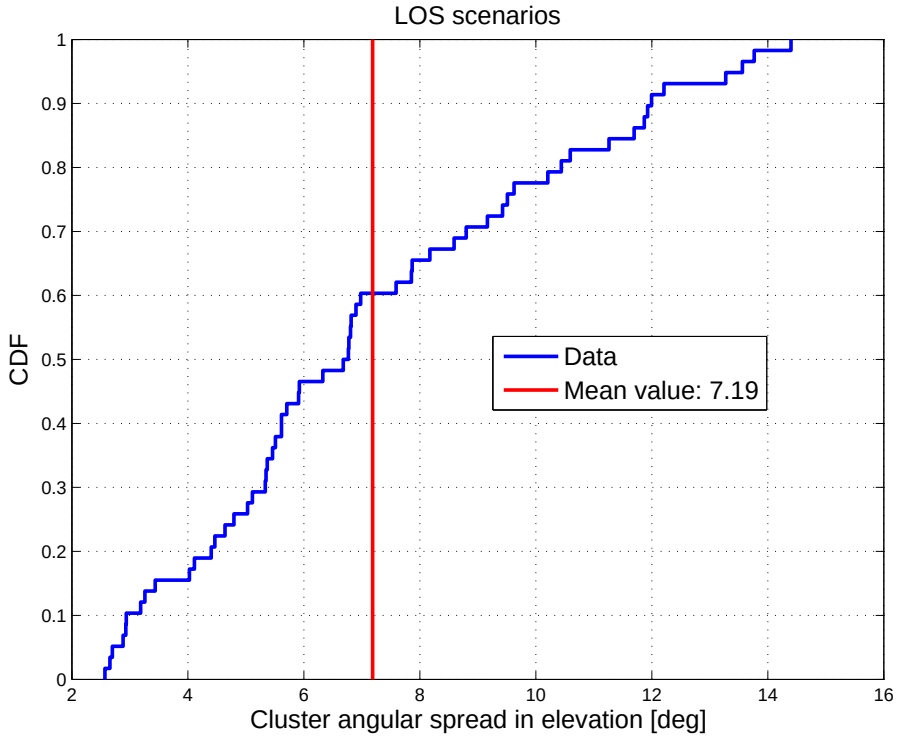

Figure 6.59: CDF of the cluster angular spreads in elevation, LOS scenarios.

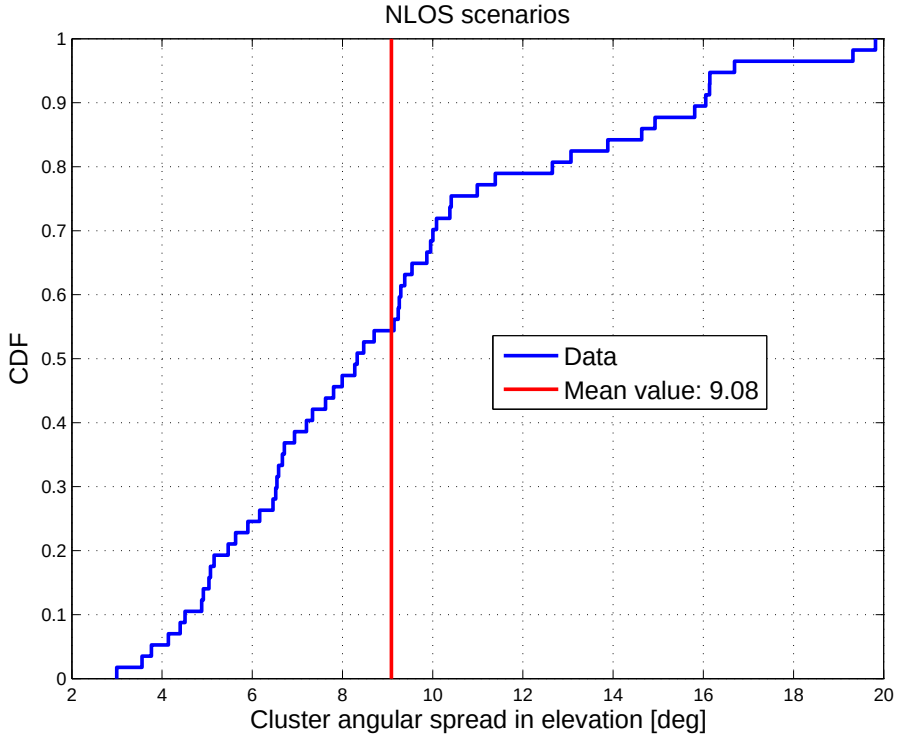

Figure 6.60: CDF of the cluster angular spreads in elevation, NLOS scenarios.

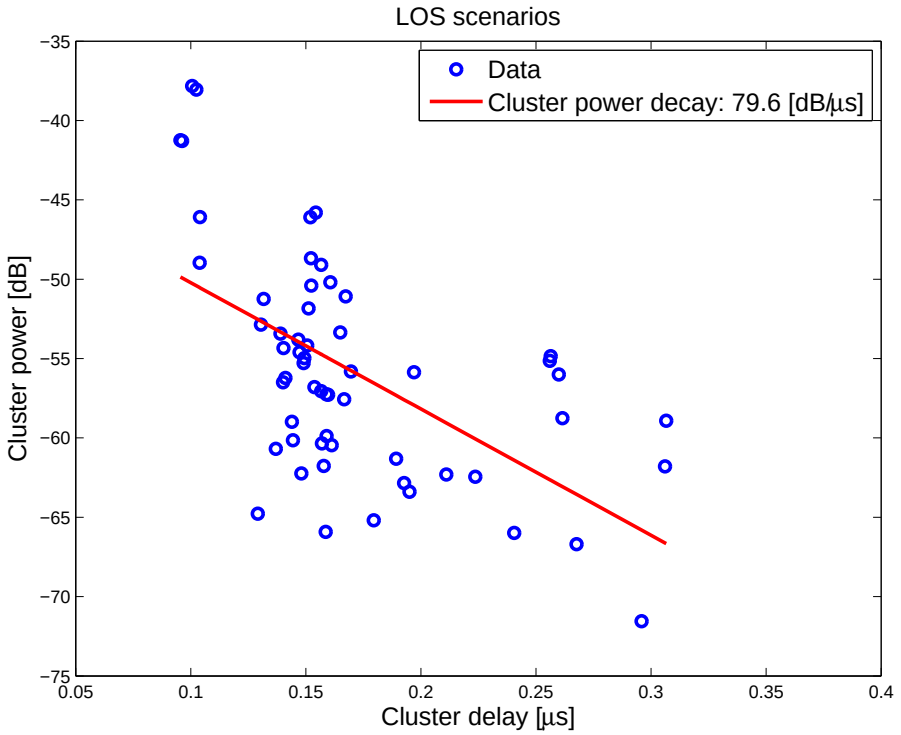

Figure 6.61: Cluster power decay, LOS scenarios.

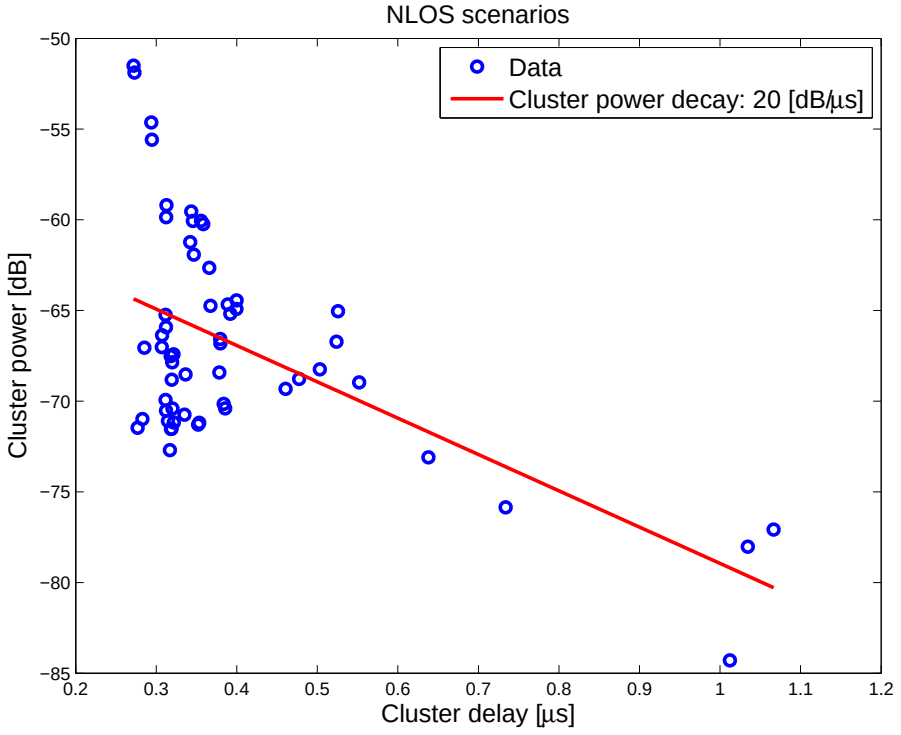

Figure 6.62: Cluster power decay, NLOS scenarios.

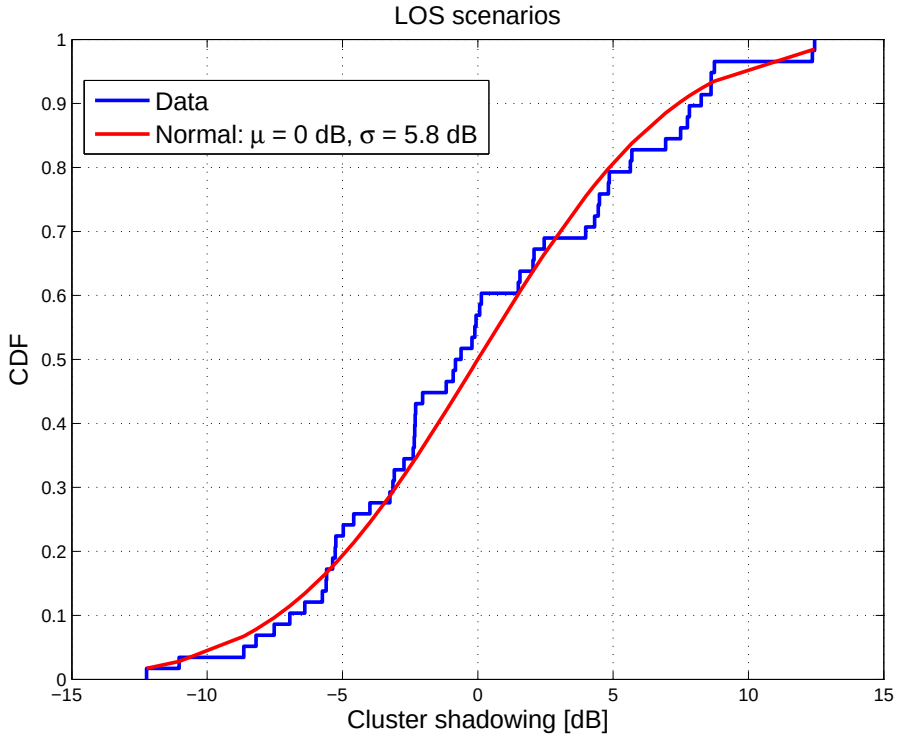

Figure 6.63: CDF of the cluster shadowing fading, LOS scenarios.

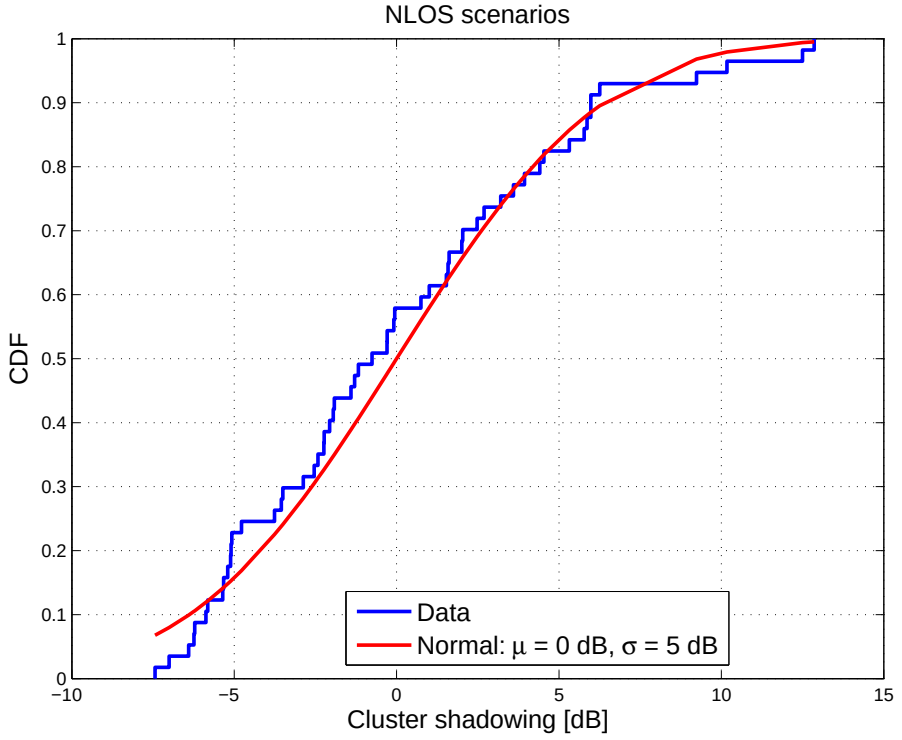

Figure 6.64: CDF of the cluster shadowing fading, NLOS scenarios.

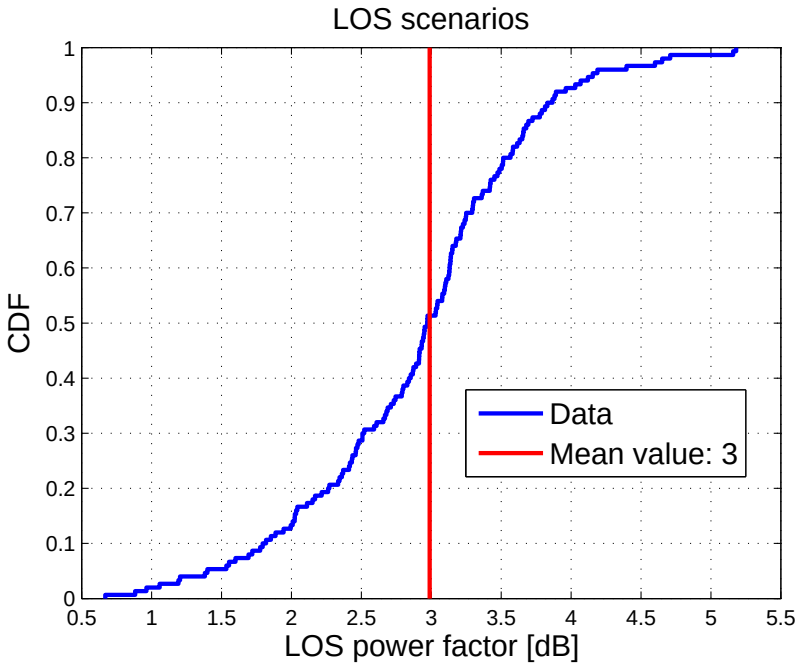

Figure 6.65: CDF of the LOS power factors (K-factors), LOS scenarios. Estimated from RSSI measurements with a single-antenna at the user side, no user effect.

Chapter 7

Massive MIMO channel model

7.1 Approach and scope

7.1.1 Model consistency

As explained earlier, the COST 2100 channel model is adopted in this work as a general framework that has the required flexibility to model the different aspects for massive MIMO channels. Besides the requirement of capturing the behavior of the wireless channels in the different spatio-temporal, angular, and delay domains, the developed channel model should also be consistent in both the spatial domain and the frequency domain. In the spatial domain, the channel model should be able to capture the propagation behavior over small distances in the range of a wavelength to very large distances (hundreds of meters), for both the terminal side and the base station side. The model should cover the cases where the user terminals are closely spaced to cases where user terminals are far separated and cases where the base station array is physically small to cases where it is physically large. The consistency in the spatial domain makes it possible to compare massive MIMO with conventional MIMO. In the frequency domain, the channel model should support lower frequencies (below 6 GHz) as well as high frequencies (above 6 GHz). The consistency in the frequency domain has become ever more important due to the trend of 5G communications toward using the higher frequency band, i.e., 6-100 GHz. The cluster-based stochastic channel model, the COST 2100 model, can meet the requirement of the consistency in both the spatial and frequency domains, as discussed above. We, however, limit the efforts here to the case below 6 GHz.

Another aspect of massive MIMO systems is the inherent higher resolution in the directional domain, which requires the channel model to provide detailed description of the channel in the sub-cluster or even multipath component levels. Therefore, despite the fact that the COST 2100 model describes a cluster as a collection of physical scattering points, more details are required to describe the behavior of individual scattering points when a user terminal is moving within their corresponding clusters visibility region. For example, the developed channel model, should consider the fact that the power contribution of a scattering point changes and it might disappear even when its corresponding cluster is active. This requires an extension of the COST 2100 channel model on the multipath component level, and should be consistent with conventional MIMO that has lower angular resolution.

7.1.2 The COST 2100 channel model extension

In this work, the COST 2100 model is extended based on the performed measurement campaigns, and modeling aspects for physically-large BS array and closely-spaced users are implemented. In the case of having limitations preventing us from extracting some parameters of interest based on our channel measurements, these parameters are implemented based on the 3GPP and WINNER channel models. For example, due to the limited polarization and directional information at the users' side in our measurements, the intra-cluster angular spread in elevation is implemented based on the 3GPP 3D model, and the cross polarization ratio (XPR) for individual MPCs is implemented based on the WINNER model. The implemented extensions for the COST 2100 model are detailed in the sequel.

3D extension

Supporting elevation angles for the MPCs is crucial in capturing the behavior of the channel especially when 2D or 3D antenna arrays are used at the BS and/or the UE sides. Besides that, the proximity of the BS and/or the UEs to the interacting objects in the environment make the effect of the elevation domain more pronounced. Therefore, in this work, the COST 2100 has been extended in 3D by including parameters such as intra-cluster angular spread in elevation for both the BS and the UE side. Due to the limitation in extracting these parameters based on our measurement campaign, The parameter values of cluster angular spread in elevation are adopted from the 3GPP 3D model [1].

Polarization extension

One of the main results discussed in the previous chapters is the significant effect of the polarization on the performance of massive MIMO systems in serving closely-spaced users. Both vertical and horizontal polarized antennas at the base station are useful for separating the users. This is of great importance since the polarization at the user side is usually dual but unknown especially when having the hand and head effect on the antenna pattern. Besides that, we also gain from the user diversity due to the difference in user polarizations and patterns. Therefore, the COST 2100 model is extended by including the polarization for the MPCs, i.e., in a single MPC, how much energy is from co-polarization (vertical to vertical and horizontal to horizontal), and how much is from cross-polarization (vertical to horizontal and horizontal to vertical). At the end, the polarization of MPCs is combined with the polarization of the BS/UE antenna pattern to generate channel transfer functions.

In our measurement campaigns, however, due to lack of the polarization information at the user side, we adopt the XPR parameters reported in the WINNER II channel models. There, XPR for each MPC follows log-normal distribution $\kappa = 10^{\frac{X}{10}}$, where $X \sim N(\mu, \sigma)$. For indoor office (A1) scenario, the mean $\mu = 11$ dB for LOS and $\mu = 10$ dB for NLOS, and the standard deviation $\sigma = 4$ dB. For large indoor hall hotspot (B3), $\mu = 9$ dB for LOS and $\mu = 6$ dB for NLOS, $\sigma = 4$ dB and $\sigma = 3$ dB for LOS and NLOS, respectively. For urban micro-cell (B1), $\mu = 9$ dB for LOS and $\mu = 8$ dB for NLOS, and $\sigma = 3$ dB.

Extension for physically-large arrays

Dedicated measurement campaigns have been performed in order to extend the COST 2100 model for the case of having physically-large arrays at the BS [7,8]. It was found that the power contribution of the individual clusters vary across the array, and clusters may not be "seen" over the whole array. It was concluded that the effect of large-scale fading can be experienced

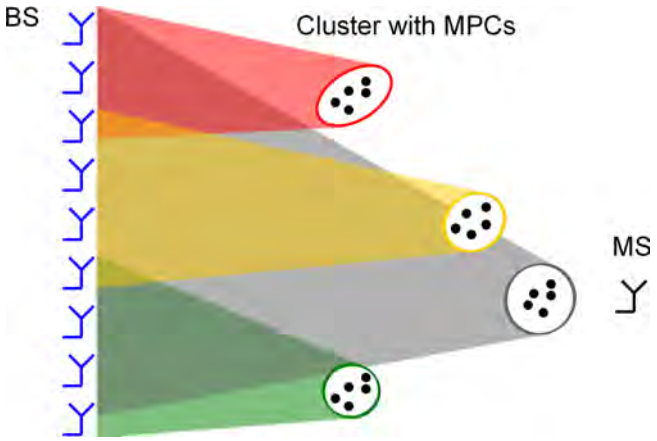

Figure 7.1: An illustration of the extension of cluster visibility regions to the base station side [9].

over physically-large arrays. Besides that, when an array spans many wavelengths in space, both users and scatterers are within its near field, hence, spherical-wave fronts are experienced at the array.

In order to capture the effect of having a physically-large array at the BS and be compatible with the convectional COST 2100 model, the simulation area at the base station side is extended to several meters, and the cluster visibility region at the BS side is introduced, see Fig. 7.1. A cluster thus has two visibility regions, one at the MS side (MS-VR) and one at the BS side (BS-VR), and the cluster contributes in the channel between a MS and a BS antenna only when the MS is within its MS-VR and the BS antenna is within its BS-VR. Based on the measurements, the size of BS-VRs and the power variation of a cluster within its BS-VR, i.e., the visibility gain, are both modeled and implemented. Besides, the number of clusters is naturally more than conventional MIMO, since a physically-large array experiences the channel more in the spatial domain. This extension naturally captures the effect of the spherical-wave front.

The extension for physically-large arrays is consistent with physically-compact arrays where a whole array is within the same BS-VR and does not experience cluster power variations. This allows direct comparison of physically-large and compact arrays in the simulation. However, the verification for this extension has not been fully done so far. Model parameters for NLOS scenarios can be found in [9].

Extension for closely-spaced users

Different measurement campaigns were performed to extract the models for the closely-located users case for both outdoor and indoor scenarios. In all cases, the users were confined within a small area, i.e., 5 m diameter circle (see previous chapters); therefore, we assume that all users stay within the same cluster visibility regions, and they all see the same far clusters. When a user is moving within this confined area, the effects of changing its position, orientation and tilt and the effect of the crowd around the user are captured as follows.

- The user antenna pattern will reflect the effect of changing the orientation and the tilt of the antenna through the complex antenna gain associated with the direction of arrival of each MPC.
- The effect of changing the position of the user within the cluster visibility region will result in varying the power contribution of each MPC, based on the relationship between the

users' position and the corresponding physical scattering point. This will make individual MPCs to have different patterns describing their contribution to the channel at each position. This effect is captured by introducing MPC gain functions that have a symmetric Gaussian shape. The gain is determined by the distance between the location (in 2D, or 3D when the 3D extension is used) of the peak of the gain function in the visibility region and the location of the antenna, i.e.

$$g_{\mathrm{MPC}}(d) = \exp\left(-\frac{d^2}{2\sigma_g^2}\right), \tag{7.1}$$

where $d = \sqrt{(x-x_i)^2 + (y-y_i)^2 + (z-z_i)^2}$ and (x_i, y_i, z_i) is the coordinate for the peak of the gain function for MPC i. The width of this function (determined by the standard deviation σ_g) controls the variability of the MPC gain and should be related to, e.g., the size of simulation area, the size of cluster visibility region and the distance between users and clusters.

Each MPC has its own gain function and it has a peak location within the corresponding cluster visibility region. For a specific user location the Euclidean distance d to the peak of the gain function is calculated, and the gain of the MPC is given as a function of this distance. The peak of the MPC gain function is randomly distributed in the corresponding cluster visibility region. From our preliminary observation, the lifetime of MPCs is about 2 m, therefore, we set $\sigma_g = 2.37$ which corresponds to 3 dB power decay when $d = 2$ m. When introducing the MPC gain functions, backward compatibility with the conventional model can be achieved by setting a large standard deviation for the gain functions, i.e., according to the size of the cluster visibility region. The number of MPCs per cluster $N_{\mathrm{MPC}}^{\mathrm{total}}$, average effective MPCs per cluster $N_{\mathrm{MPC}}^{\mathrm{effective}}$ and the radius of cluster visibility region $R_c$and radius of 3-dB power decay of MPC gain function r_g have the following relation

$$N_{\mathrm{MPC}}^{\mathrm{total}} = N_{\mathrm{MPC}}^{\mathrm{effective}} \frac{R_c^2}{r_g^2}. \tag{7.2}$$

According to the conventional models (COST 2100 and WINNER II), we choose the average number of effective MPCs per cluster to be 16. Hence, with $R_c = 10$ m and $r_g = 2$ m, the total number of MPCs per cluster is 400. The MPCs with weak power can be regarded as diffuse multipath components (DMC).

- The crowd effect which causes local scattering or absorption may be captured by utilizing the concept of the local cluster. Local clusters have already been implemented in the conventional COST 2100 model. By definition the local clusters are always visible and contain single-bounce MPCs uniformly distributed in azimuth. When a user moves, updates of the local MPCs are refilled in the local cluster at the new position. Each user has its own local cluster. When considering the effect of a crowd, it may cause scattering as well as shadowing. Therefore, we may need to modify the concept of the local clusters, e.g., by allowing local clusters have different parameters as the far clusters, or adding shadowing objects around the users. This issue needs further investigation.

By implementing directional antenna patterns at the user, the shadowing effect of the users can be captured. On the other hand, the shadowing effect due to the crowd around the user can be modeled as extra absorbing object dropped within the simulation area. At current stage, however, we do not include absorbing objects in the model.

7.1.3 Model limitations

The results reported in this document and consequently the implemented extensions of the COST 2100 model are based on two types of propagation campaigns: 1) outdoor campaigns with physically-large array at the BS and single-antenna virtual multi-user, and 2) indoor and outdoor campaigns with compact massive MIMO at the BS (cylindrical array with 128 elements) and closely-located multi-user. Based on these campaigns, the COST 2100 model is extended in order to capture different features of wireless channels; however, due to the measurement setup, the implemented "first version" model has the following limitations:

- No validation has been performed on the scenario with closely-spaced users and a physically large array at the BS. In other words, the model is capable of generating channel matrices of closely-located users given that the antenna at the BS side is compact. Therefore, the whole array at the BS is assumed to be within the same BS-VR and does not experience cluster power variations. However, from previous measurements, it was found that having physically large array at the BS increases the system's capability to separate closely-located users due to the different cluster power variations throughout the array associated with each user.

- For the outdoor scenario of having closely-located users and a compact massive MIMO at the BS, the users moved within a confined area (a circle of 5 m diameter). The MPC gain function is introduced to capture the position-dependent effects on the channel matrices of the users while moving within this confined area. We claim that the newly introduced MPC gain function combined with the already introduced cluster visibility gains are able to make the COST 2100 spatially consistent over small distances in the range of a wavelength to very large distances (hundreds of meters). However, since our measurement campaigns were confined to a small area, we have no measurement results to support the aforementioned claim.

- The measurement of the closely-located users was limited to a speed not exceeding 0.5 m/s. Doppler effect and temporal behavior due to higher speeds are not captured in the model so far.

- For the outdoor closely-located user propagation campaign, results have been reported based on the measurement sites that have LOS conditions. Due to the low SNR at the NLOS measurement sites, more processing is needed in order to reach solid conclusions.

- Due to the users (and crowd) effect on the antenna patterns of the users, in all reported results, it was not possible to decouple the antenna effect from the channel.

- Even though the users were holding the antenna in a position where it was tilted by 45 degrees, the exact antenna polarization was not known due to the random user movements. Hence, it was not possible to estimate the cross polarization of the channel based on our measurements.

7.2 Model parameters

Based on the outdoor propagation campaigns for closely-located users, the parameters used for this "first version" COST 2100 model extension are listed in Table 7.1. As marked in the table, some parameter values are adopted from a 300 MHz outdoor measurements for the COST

model, and some are adopted from the 3GPP 3D channel model and the WINNER II channel models.

7.3 Validation against measurements

We validate the model extension for closely-spaced users in LOS scenarios. In order to validate the concept and use of MPC gain functions, in the simulation we place the clusters at the same positions and with the same cluster spreads as in the measurements. Randomness are obtained through cluster shadowing, MPC distribution within clusters, and LOS K-factors, etc. We simulate the user movements in straight lines but with random rotations (between $-\pi$ to π) of user antenna patterns to simulate the rotation of users during the movements. The user antenna pattern we use in the simulation is a measured pattern in the hand of an upper body phantom. The BS antenna pattern is the measured cylindrical array antenna pattern. In the simulated channels, we also add artificial noise according to the measurement SNR, i.e., about 20 dB SNR at site 1 and 16 dB at site 2. Then we compare the simulated channels with the measured channels in terms of user separability, linear precoding sum-rates, and spatial correlation in distance.

As explained earlier, the closely-spaced users can be spatially separated because they "see" different MPCs, and this is related to the MPC gain function in the model extension. We validate this by evaluating singular value spreads in the simulated channels and sum-rates that can be achieved, and comparing with those in the measured channels. The singular value spreads and sum-rates are shown in Fig. 7.2, and Fig. 7.3.

The model should also be consistent in spatial domain and be able to capture the propagation behavior from small distances to large distances. Therefore, we validate the correlation in space from 0.01 m to 1 m through the auto-correlation functions when users are moving, as shown in Fig. 7.4. We discuss these validation in the following.

7.3.1 Singular value spreads

As can be seen in Fig. 7.2, the singular value spreads of the simulated channels match well with those of the measured channels. However, in the simulated channels, the singular value spreads have larger variations. That means, in the simulated channels, we obtain relatively low singular value spreads as well as relatively high singular value spreads. This could be due to lack of statistics in the simulations due to 1) number of simulations, 2) randomness in user movements, 3) diversities in user antenna patterns. We also see similar trends that the singular value spreads become smaller when increasing the number of BS antennas, and the difference is very small between the cases of 64 antennas and 128 antennas. In future work, the simulation could be improved by introducing more randomness in user movements, and crowd effect to the user antenna patterns.

7.3.2 MRC and ZF sum-rates

Comparing the CDFs of MRC and ZF sum-rates in the simulated and measured channels in Fig. 7.3, we clearly see larger variations in the simulated channels. This is more obvious in the ZF sum-rates than in the MRC sum-rates. It can be explained by the fact that ZF precoding is more sensitive to the spatial correlation between user channels than MRC. Again, it could be due to lack of randomness and statistics in the simulation.

Table 7.1: Parameters of the outdoor measurements for the COST 2100 channel model.

Parameter	LOS scenario	NLOS scenario
Number of far clusters		
N_{C}	15	14
Radius of cluster visibility region		
R_{C} [m]	10	10
Radius of cluster transition region		
T_{C} [m]	2	2
Number of MPCs per cluster		
N_{MPC}	400	400
Cluster power decay factor		
k_τ [dB/μs]	79.6	20
Cluster cut-off delay		
τ_{B} [μs]	1.7	1.7
Cluster shadowing		
σ_{S} [dB]	5.8	5
Cluster delay spread		
m_τ [μs]	0.02	0.06
S_τ [dB]	0.01	0.01
Cluster angular spread in azimuth (at BS)		
$m_{\psi_{\mathrm{BS}}}$ [deg]	8.5	9.8
$S_{\psi_{\mathrm{BS}}}$ [dB]	1.9	2.2
Cluster angular spread in elevation (at BS)		
$m_{\theta_{\mathrm{BS}}}$ [deg]	7.0	8.9
$S_{\theta_{\mathrm{BS}}}$ [dB]	1.9	1.9
Cluster angular spread in azimuth (at MS)[1]		
$m_{\psi_{\mathrm{MS}}}$ [deg]	14.8	19
$S_{\psi_{\mathrm{MS}}}$ [dB]	2.68	2.03
Cluster angular spread in elevation (at MS)[2]		
$m_{\theta_{\mathrm{MS}}}$ [deg]	4	7.6
$S_{\theta_{\mathrm{MS}}}$ [dB]	1.6	1.6
Cluster spread cross-correlation		
$\rho_{\tau\sigma_{\mathrm{S}}}$	-0.5	-0.4
$\rho_{\psi_{\mathrm{BS}}\sigma_{\mathrm{S}}}$	-0.8	-0.8
$\rho_{\theta_{\mathrm{BS}}\sigma_{\mathrm{S}}}$	-0.8	-0.7
$\rho_{\psi_{\mathrm{BS}}\tau}$	0.6	0.4
$\rho_{\theta_{\mathrm{BS}}\tau}$	0.4	0.2
$\rho_{\psi_{\mathrm{BS}}\theta_{\mathrm{BS}}}$	0.7	0.7
Radius of LOS visibility region[1]		
R_{L} [m]	343	-
Radius of LOS transition region[1]		
T_{L} [m]	93	-
LOS power factor		
$\mu_{K_{\mathrm{LOS}}}$ [dB]	2.8	-
$\sigma_{K_{\mathrm{LOS}}}$ [dB]	0.8	-
XPR[3]		
μ_{XPR} [dB]	9	8
σ_{XPR} [dB]	3	3
MPC gain function		
σ_g	2.37	2.37

[1]Parameter values adopted from the 300 MHz outdoor measurements for the COST 2100 model [22].
[2]Parameter values adopted from the 3GPP 3D channel model [1].
[3]Parameter values adopted from the WINNER II channel models [11].

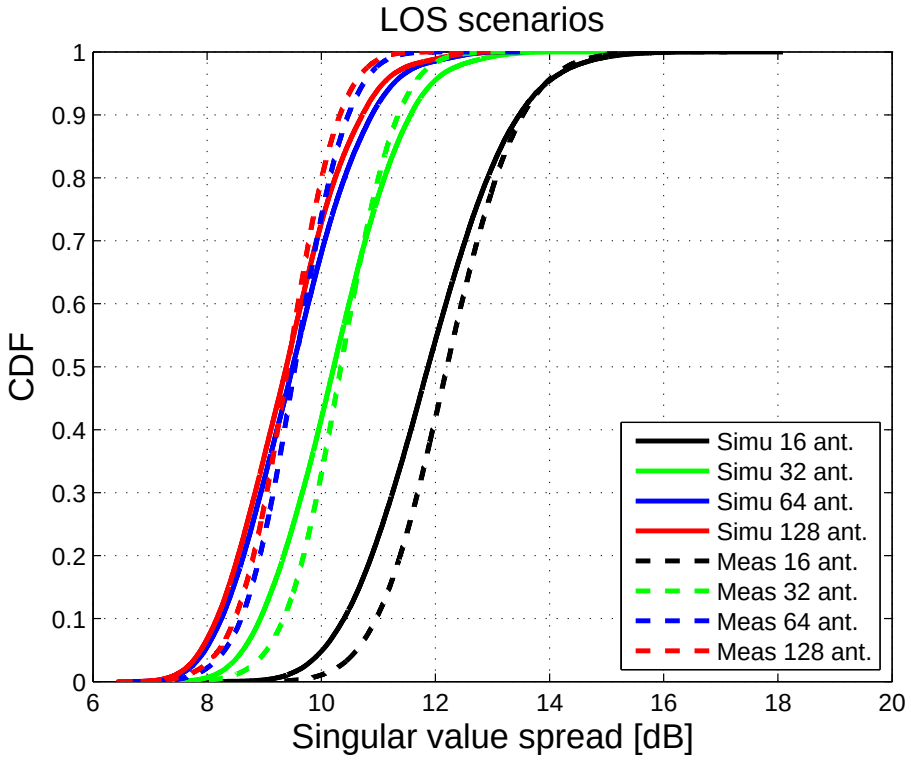

Figure 7.2: Singular value spreads of the simulated channels and measured channels.

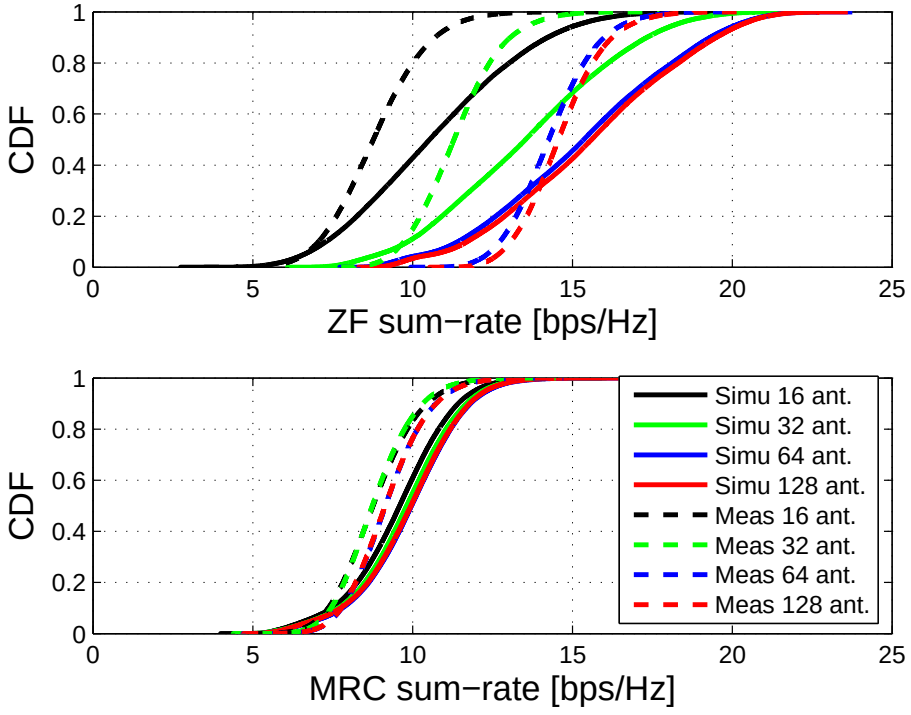

Figure 7.3: Downlink sum-rates by ZF and MRC in the simulated channels and measured channels, when the average interference-free SNR at the users is 10 dB.

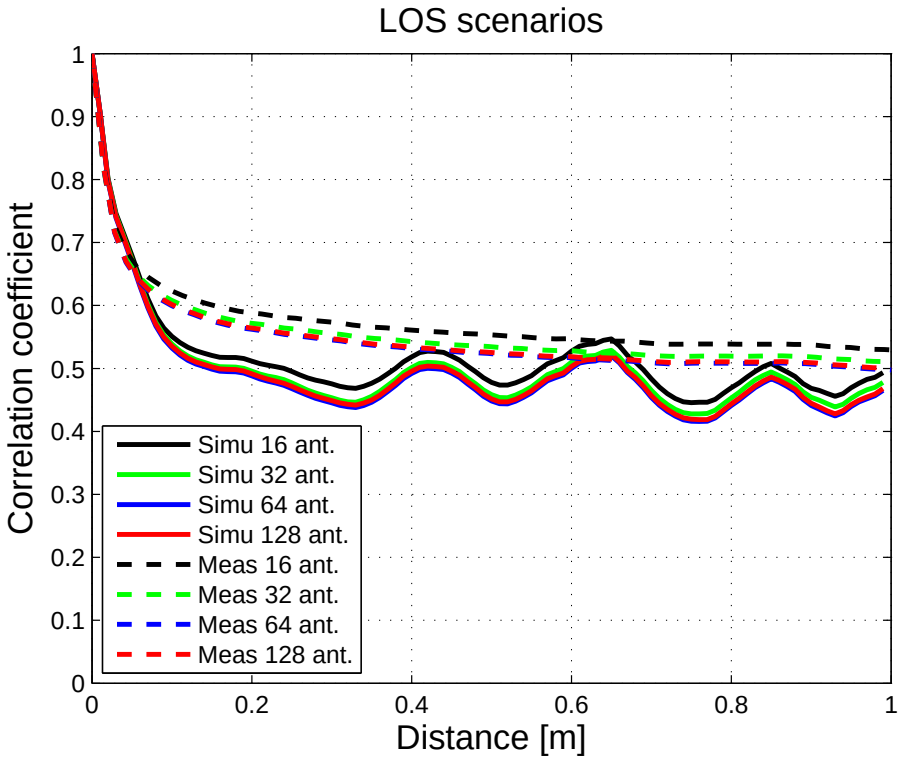

Figure 7.4: Auto-correlation in distance of the simulated channels and measured channels.

7.3.3 Temporal behavior

The temporal behavior of the simulated and measure channels in terms of auto-correlation in space of one user are shown in Fig. 7.4. The auto-correlation is averaged over different users, snapshots and frequencies. The correlation coefficient $c(\Delta_t)$ is calculated as below,

$$c(\Delta_t) = \frac{1}{L}\sum_{\ell=1}^{\ell=L}\frac{1}{K}\sum_{k=1}^{k=K}\frac{1}{T}\sum_{t=1}^{t=T}\left|\frac{\mathbf{h}_{t,k,\ell}\mathbf{h}_{t+\Delta_t,k,\ell}^{H}}{\|\mathbf{h}_{t,k,\ell}\|\,\|\mathbf{h}_{t+\Delta_t,k,\ell}\|}\right|, \tag{7.3}$$

where $\mathbf{h}_{t,k,\ell}$ is the $1\times M$ channel vector, M is the number of BS antennas, and t, k and ℓ represent snapshots, users and frequencies, respectively. Note that the averaging is performed on the amplitudes of the correlation coefficients in each realization. We see that from 0.01 m to 1 m the auto-correlation in the simulated channels matches with that in the measured channels, although the auto-correlation is slightly lower and the variation is larger in the simulated channels. This indicates that with the model extension we are able to capture the temporal behavior of the channels in a small distance.

Chapter 8

Summary

Understanding the channel behavior is crucial for robust and efficient system and algorithm design, as well as for realistic assessment of the possible performance of any wireless system. In this deliverable we have discussed requirements on massive MIMO channel models and identified important properties that have to be well reflected by the model for realistic assessment of system performance. We have reported on a thorough measurement campaign for massive MIMO, specifically targeting the "Open Exhibition" and "Crowded auditorium" scenarios, which are seen as key scenarios for future 5G deployments. The performed measurements are described, in terms of equipment, setup and measurement configuration.

We have analyzed the measurements by system level measures such as singular value spreads and sum-rate capacities, and we have performed a detailed directional analysis of the propagation characteristics. The directional data is also used for a clustering analysis.

Based on the results and analysis we have proposed and implemented a backwards compatible extension of the COST 2100 channel model for massive MIMO. The extension includes:

- Extension from two to three dimensions, as the large base station arrays envisioned most likely will have the ability resolve clusters of multipath components both in azimuth and elevation.
- Cluster centric visibility regtions both at the user side and at the base station side. The introduced base station visibility regions give the ability to capture large-scale fading effects along physically large arrays.
- Individual gain functions of individual multipath components as individual multipath components tend not to be visible in the entire cluster visibility region.

A parameterization of the model, based on the measurements, is performed. Model parameters from the COST 2100 and the WINNER II channel models are used as a complement to get a complete set of model parameters. The channel model has been implemented in MATLAB and validation is performed by comparing against measurements, using the same measures (singular-value spreads, sum-rate capacities, directional properties and time/frequency correlations). Similarities and discrepancies are discussed.

While this version of the deliverable provides analysis and a channel model, including its parameters, for massive MIMO we expect that more analysis and feedback on the model will become available as the MAMMOET project progresses. Especially when the model is used in WP3 and WP4 we expect additional valuable insights into its strengths and weaknesses. Updated versions will be released of both the model and its MATLAB implementation. To reflect this, we expect to release an updated version of this deliverable at the end of 2015.

The presented analysis, including the propagation characteristics and channel parameters, and the proposed channel model extension for massive MIMO of the well known COST 2100 model will be a valuable input to the standardization efforts of channel models for 5G. The results will also be crucial for the development of massive MIMO systems and signal processing algorithms for massive MIMO, as well as for realistic assessment of the possible performance gains of massive MIMO in real environments.

List of Abbreviations

ACLR	Adjacent Channel Leakage Ratio
ASI	Application-Specific Instruction
ASIC	Application-Specific Integrated Circuit
ASIP	Application-Specific Instruction-set Processor
BER	Bit Error Rate
BS	Base Station
CB	Conjugate Beamforming
CP	Cyclic Prefix
CE	Cyclic Extension
CSI	Channel Statie Information
DLP	Data-Level Parallelism
DSP	Digital Signal Processor (or Digital Signal Processing)
DTCE	Discrete-Time Constant-Envelope
EC	European Commission
FD	Frequency-Domain
FDD	Frequency-Division Duplex
FDE	Frequency-Domain Equalizer
FIR	Finite Impulse Response
FPGA	Field-Programmable Gate Array
ILP	Instruction-Level Parallelism
KSP	Known-Symbol Padding
LMMSE	Linear Minimum Mean-Squared Error
MIMO	Multiple-Input Multiple-Output
MMSE	Minimum Mean-Squared Error
MRC	Maximum-Ratio Combining
MRT	Maximum-Ratio Transmission
MS	Mobile Station
MSE	Mean-Squared Error
NMSE	Normalized Mean-Square-Error
NRE	Non-Recurring Engineering

OFDM	Orthogonal frequency-division multiplexing
PA	Power Amplifier
QAM	Quadrature Amplitude Modulation
PAPR	Peak-to-Average Power Ratio
PER	Packet Error Rate
RF	Radio Frequency
RZF	Regularized Zero-Forcing
SC	Single-Carrier
SDR	Software-Defined Radio
SIMD	Single-Instruction Multiple-Data
SISO	Single-Input Single-Output
SNR	Signal-to-Noise Ratio
TD	Time-Domain
TDD	Time-Domain Duplex
TDE	Time-Domain Equalizer
TLP	Task-Level Parallelism
VLIW	Very Long Instruction Word
ZF	Zero Forcing
ZP	Zero Padding

Bibliography

[1] Study on 3D channel model for LTE. Technical Report TR 36.873 V12.1.0, 3GPP, 2015.

[2] Oliveras A., De Carcalho E., and Nielsen J.Ø. Towards very large aperture massive MIMO: A measurement based study. In *Global Telecommunications Conference, 2014. GLOBECOM '14. IEEE*, pages 281 –286, dec 2014.

[3] M. Costa. Writing on dirty paper. *IEEE Trans. Intell. Transp. Syst.*, IT-29(3):439–441, May 1983.

[4] N Czink. *The random-cluster model*. PhD thesis, PhD thesis, Technische Universität Wien, 2007.

[5] N. Czink, P. Cera, J. Salo, E. Bonek, J.-P. Nuutinen, and J. Ylitalo. A framework for automatic clustering of parametric MIMO channel data including path powers. In *2006 IEEE 64th Vehicular Technology Conference, 2006. VTC-2006 Fall.*, pages 1–5, Sept 2006.

[6] B.H. Fleury, M. Tschudin, R. Heddergott, D. Dalhaus, and K. Ingeman-Pedersen. Channel parameter estimation in mobile radio environments using the sage algorithm. *IEEE J. Sel. Areas Commun.*, 17(3):434–450, 1999.

[7] X. Gao, O. Edfors, F. Rusek, and F. Tufvesson. Massive MIMO performance evaluation based on measured propagation data. *IEEE Transactions on Wireless Communications*, PP(99):1–1, 2015.

[8] Xiang Gao, F. Tufvesson, and O. Edfors. Massive MIMO channels - measurements and models. In *2013 47th Asilomar Conference on Signals, Systems and Computers (ASILOMAR)*, 2013.

[9] Xiang Gao, Meifang Zhu, Fredrik Tufvesson, Fredrik Rusek, and Ove Edfors. Extension of the COST 2100 channel model for massive MIMO. 2015.

[10] Nihar Jindal, Wonjong Rhee, Sriram Vishwanath, Ali Jafar, and Andrea Goldsmith. Sum power iterative water-filling for multi-antenna Gaussian broadcast channels. *IEEE Trans. Intell. Transp. Syst.*, 51(4):1570–1580, April 2005.

[11] Pekka Kyösti, Juha Meinilä, Lassi Hentilä, Xiongwen Zhao, Tommi Jämsä, Christian Schneider, Milan Narandzić, Marko Milojević, Aihua Hong, Juha Ylitalo, et al. Winner II channel models. 2008.

[12] Lingfeng Liu, C. Oestges, J. Poutanen, K. Haneda, P. Vainikainen, F. Quitin, F. Tufvesson, and P.D. Doncker. The cost 2100 mimo channel model. *Wireless Communications, IEEE*, 19(6):92–99, December 2012.

[13] T. L. Marzetta. Noncooperative cellular wireless with unlimited number of base station antennas. *IEEE Trans. Wireless Commun.*, 9(11):3590–3600, November 2010.

[14] Andreas F. Molisch. *Wireless Communications*. John Wiley & Sons, New York, 2011.

[15] Arogyaswami Paulraj, Rohit Nabar, and Dhananjay Gore. *Introduction to Space-Time Wireless Communications*. Cambridge University Press, The Edinburg Building, Cambridge CB2 8RU, UK, first edition, 2008.

[16] S. Payami and F. Tufvesson. Channel measurements and analysis for very large array systems at 2.6 ghz. In *Antennas and Propagation (EUCAP), 2012 6th European Conference on*, pages 433–437, March 2012.

[17] Fredrik Rusek, Daniel Persson, Buon Kiong Lau, Erik G. Larsson, Thomas L. Marzetta, Ove Edfors, and Fredrik Tufvesson. Scaling up MIMO: Opportunities and challenges with very large arrays. *IEEE Signal Process. Mag.*, 30(1):40–60, January 2013.

[18] M. Steinbauer, Andreas F. Molisch, and E. Bonek. The double-directional radio channel. 43(4):51–63, August 2001.

[19] İ. Emre Telatar. Capacity of multi-antenna Gaussian channels. *European Transactions on Telecommunications: ETT*, 10(6):585–595, 1999.

[20] Reiner S. Thomä, Dirk Hampicke, Andreas Richter, Gerd Sommerkorn, Axel Schneider, Uwe Trautwein, and Walter Wirnitzer. Identification of time-variant directional mobile radio channels. 49(2):357–364, April 2000.

[21] Shangbin Wu, Cheng-Xiang Wang, E.-H.M. Aggoune, M.M. Alwakeel, and Yejun He. A non-stationary 3-d wideband twin-cluster model for 5g massive mimo channels. *Selected Areas in Communications, IEEE Journal on*, 32(6):1207–1218, June 2014.

[22] Meifang Zhu, G. Eriksson, and F. Tufvesson. The COST 2100 channel model: Parameterization and validation based on outdoor MIMO measurements at 300 Mhz. *IEEE Transactions on Wireless Communications*, 12(2):888–897, February 2013.